FINAL SCIENTIFIC REPORT

Assessing the Geomechanical Response of CO_2 Disposal in Flood Basalt Reservoirs

Award Number:
DE-FE0023381

Submitted to:
National Energy Technology Laboratory

Principal Investigators:

Ryan M. Pollyea (Lead PI)
Assistant Professor
Virginia Tech
(540) 231-7929
rpollyea@vt.edu

Sally M. Benson (co-PI)
Professor
Stanford University
(650) 725-0358
smbenson@stanford.edu

Submission Date:
November 30, 2018

DUNS Number:
003137015

Submitting Organization:
Virginia Polytechnic Institute & State University

Project Period:
10/01/2014 – 8/30/2018

Reporting Period End Date:
8/31/2018

DISCLAIMER

ABSTRACT

In this work, we complete a multi-scale investigation of the physical processes governing geologic CO_2 sequestration in basalt reservoirs. This work integrates (i) laboratory measurements of relative permeability in a basalt fracture, (ii) theoretical modeling to understand how relative permeability uncertainty affects geomechanical performance attributes of basalt reservoirs, (iii) outcrop-scale simulation to identify the characteristics of vertical CO_2 flow in a basalt fracture network, and (iv) regional-scale assessment of permeability architecture in the Columbia River Basalt Group (CRBG). These individual studies are combined into a site-scale stochastic model of geologic CO_2 sequestration in the Columbia River Plateau, which shows how bulk and relative permeability variability affects geomechanical reservoir integrity and storage capacity of flood basalt reservoirs. This project resulted in a novel laboratory technique that combines X-ray CT and micro-PET scanning to calculate the relative permeability curves for a horizontal fracture in basalt. We also discovered that permeability on the Columbia River Plateau exhibits directionally-dependent spatial correlation, which our analysis suggests is a result of loading-induced subsidence. This analysis further discovered that permeability in the CRBG may increase at depth due to bending moment stresses. In the context of CO_2 sequestration, this result implies that storage capacity and injectivity may actually increase at depths beyond ~1 km. Our outcrop-scale investigation found that buoyant, free-phase CO_2 tends to accumulate at fracture intersections, which inhibits vertical flow over 10+ year timescales and may facilitate both physical and chemical trapping as fluid mobility decreases. At the site-scale, we find that in flood basalt reservoirs the spatial configuration of reservoir permeability exhibits substantial control on CO_2 injectivity. We utilized known borehole geology from the Wallula Basalt Sequestration Pilot Project to develop 50 equally probable permeability configurations and found that a single injection well operating at 95% of the borehole breakout pressure can deliver 0.12 to 2.0 million metric tons of CO_2 per year (MMT_{CO2} yr^{-1}). This maximum injection rate can support a 1,000 MW gas-fired power plant with a single injection well.

TABLE OF CONTENTS

EXECUTIVE SUMMARY

Basalt formations have been proposed for carbon capture and sequestration (CCS) reservoirs on the basis of rapid mineral trapping and significant storage capacity in both onshore and offshore formations. Small-scale field tests (<1,000 tons CO_2) in Iceland and Washington, USA, show compelling evidence for rapid CO_2 mineralization in basalt formations, and storage estimates are on the order of 10^2 Gt CO_2 for individual continental flood basalt provinces and accessible offshore basalt formations. As a result, CO_2 storage in basalt reservoirs has the potential to significantly expand the geographic potential for CCS technology. Although basalt sequestration exhibits many favorable attributes, there remains significant uncertainty in industrial-scale deployment owing in large part to the pervasively fractured nature of basalt reservoirs. These fracture networks are characterized by fanning columnar joints with highly variable geometric orientations, which result in high levels of reservoir uncertainty for risk assessment and optimization studies because fracture networks govern the CO_2 flow characteristics and mineral trapping potential in basalt formations. This research is a multi-scale investigation of the physical processes governing geologic CO_2 sequestration in basalt reservoirs with a specific emphasis on the role of bulk and relative permeability in CO_2 storage potential and geomechanical reservoir integrity. This project comprises four individual studies that increase our knowledge of reservoir performance characteristics during CO_2 flow in basalt fracture networks. Each study occurs at varying scales of observation, including core-, outcrop-, and regional-scales. This knowledge is then integrated into a site-scale modeling study to quantify the effects of permeability uncertainty at the Wallula Basalt Sequestration Pilot Project in Washington State, USA. Below is a summary of results for each study, as well as recommendations for future research in the area of basalt sequestration:

Relative Permeability Measurements in Fractured Basalt

This study developed a new method to calculate relative permeability in a basalt fracture by combining core-flood experiments with X-ray CT and micro-PET scanning. Results from this experiment listed below.

- The relative permeability of basalt fractures is highly interfering and not well represented by widely used relative permeability models such as X-curves.
- Gas flow does not displace water from the smaller fracture apertures or regions with larger apertures that are not connected to the inlet and outlet of the core.
- Multiphase flow shifts quickly from a liquid to a gas dominated system in fractures. The abrupt transition between the two flow regimes suggest that fractures are likely to be either gas or water conducting, depending on achieving a high enough gas saturation in the fracture.
- Water flows mainly through a connected set of the largest apertures. Other portions of the fracture are difficult to access for water and gas flow. This suggests that chemical reactions in the small apertures (which are likely to be prevalent in the fracture) will require diffusion of the solutes into the smaller apertures. This will slow or limit chemical reactivity in fractured rocks.

Dynamics of Outcrop-Scale CO_2 Flow in a Basalt Fracture Network

In this study, terrestrial LiDAR is used to a develop high resolution, 2-D representation of a basalt fracture network exposed in outcrop. This fracture network is then utilized to simulate buoyant CO2 flow in 50 equaly probable fracture permeability distribution to identify characteristic flow dynamics in the fracture network. The summary of results from this study are listed below.

- Fracture network geometry controls flow paths and fluid pressure in early time (~1 year), while CO_2 saturation is governed by interactions between fracture permeability and network geometry.
- As CO_2 invades the fracture network, it tends to accumulates at fracture intersections.
- Phase change from super- to sub-critical CO_2 occurs over a narrow depth interval (~1.6 m), which suggests that flood basalt entablature zones may exhibit favorable physical trapping characteristics for isolating CO_2 over time scales required for mineral trapping.
- CO_2 flow tends to converge on a single flow path.
- The combination of CO_2 accumulation at fracture intersections and convergence towards a single flow path (over 5 m spatial scales) suggests fracture network connectivity may be substantially reduced due to mineral precipitation.

Regional-Scale Permeability Architecture of the Columbia River Basalt Group

While developing the site-scale model of CO_2 injections at the Wallula Basalt Sequestration Pilot Project, we compiled a database of all publicly available permeability data within the Columbia River Basalt Group (CRBG). Geostatistical analysis of this database resulted in an important discovery with significant implications for CCS in large igneous provinces. The summary of results is below.

- Between 950 and 1,450 m depth, mean CRBG permeability increases by 1.5 orders of magnitude, which is highly unexpected and deviates from well-known permeability vs. depth scaling relationships.
- The spatial correlation of CRBG permeability is direction-dependent and the axis of maximum correlation is parallel to the long axis of the underlying bedrock basin (N40°E).
- Our results suggest that CRBG emplacement induced lithospheric subsidence that caused a bending moment in the basalt pile.
- This bending moment preferentially dilates fractures in the direction of maximum spatial correlation and causes a reversal in the expected permeability-depth trend.
- Higher than expected permeability at depth will increase the injectivity of basalt reservoirs at depths where CO_2 will remain in the supercritical field.

Quantifying CO_2 Injectivity at 95% of Borehole Breakdown Pressure at Wallula Site

This study combines relative permeability measurements, knowledge of outcrop-scale CO2 flow dynamics, and geostatistical analysis of regional-scale CRBG permeability to model CO2 injections at the Wallula site. In doing so, we generate 50 equally probable reservoir models that each reproduce borehole geology from the Wallula well and simulate intermediate- and far-field permeability distributions on the basis of semivariogram correlation structure. This model scenario implements a constant pressure CO2 injection in a single injection well for a period of 20 years. The injection pressure is 12.1 MPa above reservoir pressure and accounts for 95% of the borehole breakdown pressure. As a result, these results constrain the plausible outcomes for a stable geomechanical regime.

- The mean CO_2 plume comprising all the 50 simulations results is circular (in plan view) about the injection well. This represents the volume that CO_2 will occupy with a high degree of confidence and regardless of permeability structure.
- Model uncertainty is manifest as an ellipse around the mean CO_2 plume that extends up to 1,800m away from the injection well. The ellipse trends parallel to the direction of maximum permeability correlation and suggests that the location of spatially correlated and interconnected flow paths are key pieces of information to fully constrain CO_2 migration in basalt reservoirs.
- After 20 years, CO_2 migrates vertically from the injection zone into the entablature layer bounding the injection zone, but it does not migrate any further suggesting that this region has the potential for CO_2-water-basalt interactions to effectively isolate large-scale CO_2 injection volumes.
- The total mass of CO_2 injected at 95% of the borehole breakout pressure for 20 years ranges from 2.4 MMT (0.12 MMT yr^{-1}) to 40.0 MMT (2.0 MMT yr^{-1}). The maximum volume injected could support at 1,000 MW gas-fired power plant with a single injection.
- This study also finds that the heat of dissolution associated with a large-scale CO_2 injection may be an effective MMV strategy for monitoring CO_2 breakthrough.

Overall Conclusions

Geologic carbon sequestration in basalt reservoirs is predicated on the geochemical transformation of CO_2 into immobile mineral precipitates. Recent field experiments in Washington State and Iceland show that this process occurs rapidly over annual timescales. In this context, the current project revealed several promising attributes for CCS in basalt reservoirs. Specifically, both outcrop- and site-scale simulation studies find that (i) basalt fracture networks are capable of trapping free-phase CO_2 over timescales required for widespread mineralization to occur and (ii) basalt injectivity is theoretically capable of supporting up to 2 MMT per year within a single injection well operating below the fracture pressure. Moreover, this study also finds that CO_2 tends to accumulate at fracture intersections, which slows vertical CO_2 mobility and increases fluid residence time, suggesting that mineralization may focus at fracture intersections. As a consequence, there exists a theoretical possibility that basalt fracture networks may be self-sealing systems in the presence of an equilibrium supply of CO_2; however, additional research is needed to more fully understand the dissolution-precipitation processes in natural fractures.

1. INTRODUCTION

A growing body of evidence suggests that deep basalt reservoirs (>800 m) may be attractive targets for CCS on the basis of favorable CO_2-water-rock reaction kinetics, which result in permanent CO_2 isolation through mineral trapping (McGrail et al., 2006; Matter and Kelemen, 2009). These reactions have been investigated theoretically on the basis of kinetic rate laws (Alexander et al., 2007), and in the laboratory using both grain-scale (McGrail et al., 2006) and core-scale experiments (Schaef et al., 2011). The work by Schaef et al. (2011) shows that CO_2, dissolved in either the aqueous phase or a water-rich supercritical phase, produces carbonate precipitates when exposed to basalt samples under temperature and pressure conditions representative of reservoir depth for a period of 180 days. This work also shows increasing mineralization rates with increasing temperature and pressure, suggesting that deep basalt reservoirs may be ideal targets for CCS implementation. In addition, natural analogs for this process were identified by Kelley et al. (2001) in a Mid-Atlantic Ridge hydrothermal vent field composed of ultramafic peridotite. More recently, geochemical experiments suggest that H_2S impurities within the CO_2 waste stream can be permanently co-sequestered as pyrite (Schaef et al., 2013), and numerical simulations of this process suggest H_2S concentrations up to 1 mol% do not adversely impact long term CO_2 mineralization (Bacon et al., 2014). These theoretical results are further supported by two promising field experiments, which showed rapid mineralization after both aqueous- (Matter et al., 2016) and supercritical-phase (McGrail et al., 2017) CO_2 injections. To complement these results, CCS in deep basalt reservoirs is motivated to a large extent by the relatively high storage potential within both onshore and offshore basalt formations. In particular, CO_2 storage estimates for the Columbia River Basalt Group in the northwestern United States are estimated to be on the order of 100 Gt CO_2 (McGrail et al., 2006), and offshore basalt formations within the Juan de Fuca plate and Central Atlantic Magmatic Province hold potential for CO_2 disposal on comparable scales (Goldberg et al., 2008, 2010).

1.1 Columbia River Basalt Group

The Columbia River Basalt Group (CRBG)—located in the northwestern United States—is among the most intensively studied large igneous provinces in the world owing in large part to hydrogeological characterization at the Hanford Nuclear Reservation and natural gas storage assessments in southeast Washington State. The CRBG is a layered assemblage of ~300 Miocene- age continental flood basalts with an areal extent of 200,000 km^2 (Figure 1), thickness between 1 and 5 km, and estimated aggregate volume greater than 224,000 km^3 (Reidel et al., 2002). Individual CRBG basalt flows exhibit km-scale lateral dimensions and vertical dimensions ranging from cm-scale to greater than 70 m (Mangan et al., 1986). Individual basalt flow morphology is characterized by (1) densely fractured, vesicular flow-tops, which result from rapid thermal contraction during cooling, (2) a central entablature comprising narrow, fanning columnar joints with hexagonal cross-sectional geometry, which result from thermal interactions between the upper and lower cooling fronts during solidification, Wallula Site and (3) lower colonnades with vertical, column bounding joints and, to a lesser extent, horizontal column-normal joints (Mangan et al., 1986). Within CRBG formations, the entablature is generally considered a barrier to fluid flow on the basis of in situ pumping tests that reveal hydraulic conductivity within the entablature is approximately seven orders of magnitude lower than in the densely fracture flow-tops (McGrail et al., 2009). This hydraulic conductivity contrast, combined with the km-scale areal extent of individual CRBG basalt flows, suggests that entablature zones may act as physical traps over a sufficient time frame to accommodate permanent CO_2 isolation through mineralization (McGrail et al., 2006).

On the basis of relatively high CO_2 storage estimates, potential for permanent CO_2 isolation, and generally favorable reservoir characteristics, the U.S. Department of Energy, through the Big Sky Carbon Sequestration Partnership (BSCSP), has identified the CRBG as the primary target formation for CCS development in the Pacific Northwest (Litynski et al., 2006, USDOE, 2010, Rodosta et al., 2011). As a result, the U.S. Department of Energy and BSCSP began initial site characterization efforts in 2007 for a pilot-scale CCS demonstration project at the Boise Mill Site, located along the Columbia River approximately 15 km southeast of Kennewick, WA (Spane et al., 2007). Initial site characterization efforts identified favorable reservoir properties for supercritical CO2 injections within a 59 m thickness of the Grande Ronde Formation, and delineated an injection zone between 828 and 887 m below ground surface (McGrail et al., 2009, 2011). Data from this site characterization effort have been used to constrain multi-phase/multi-component numerical models of supercritical CO_2 injections within the Grande Ronde Formation, and results demonstrate that physical trapping is generally favorable for a 1,000 metric ton pilot-scale CO_2 injection. As a result, in July 2013, the BSCSP began the validation phase of the Boise Mill Site (formally called the Wallula Basalt Sequestration Pilot Project) by initiating a 1,000 metric

ton CO_2 injection. The Wallula site was the monitored for two years post injection, and isotopic analysis of sidewall cores from the test well indicate that (i) carbonate mineral precipitation was widespread in the injection zone and (ii) the isotopic signature of carbon in carbonate alteration products is the same as in the injected CO_2 (McGrail et al., 2017).

1.2 Challenges to CCS in CRBG Reservoirs

Among the principal challenges for industrial-scale CCS in any geologic environment is to ensure >99% CO_2 isolation per thousand years (USDOE, 2013), which, if not met, will likely postpone rather than mitigate global warming trends (Shaffer, 2010). In order to achieve >99% CO_2 isolation, the integrity of physical traps (i.e., cap-rock seals) under long-term injection pressure is a paramount concern because excessive reservoir pressure may result in a number of adverse consequences, including fracture propagation/reactivation (Lucier et al., 2006, Goodarzi et al., 2011), shear or joint dilation (Min et al., 2004), induced seismicity (Cappa and Rutqvist, 2011), and cm-scale displacements on small, difficult to characterize faults and fractures (Zoback and Gorelick, 2012). Within CRBG reservoirs, pressure build up is a particular concern because both reservoir and seal rock are ubiquitously fractured. In particular, the central entablature is characterized by fanning columnar joints with narrow apertures and low permeability. As a result, the central entablature is generally considered to be a physical trap for CO_2 isolation prior to widespread mineral trapping; however, the fanning geometry of entablature joints also suggests that a subset of these fractures may be optimally aligned for shear dilation and propagation. Moreover, increasing fluid pressure during injection may also result in fracture dilation, which would dramatically increase the effective permeability of the central entablature because discharge within both open and closed fractures is known to increase with the cube of the fracture aperture (Witherspoon et al., 1980). As a result, the sealing efficacy of the central entablature may be highly sensitive to modest increases in fluid pressure within the reservoir.

Although the site characterization and simulation results from the Wallula Basalt Sequestration Pilot Project are generally favorable, there remain significant technical challenges to industrial-scale CCS deployment within the CRBG. In particular, there are several fundamental knowledge gaps with respect to multi-phase CO_2-brine flow in basalt reservoirs. For example, the relative permeability characteristics of basalt fractures are poorly constrained, as are the dynamics of CO_2 flow in discrete basalt fracture networks and the site-scale storage potential of highly heterogeneous flood basalt storage reservoirs. This project fills this gap in knowledge by (i) developing new laboratory methods for relative permeability measurements in basalt cores, (ii) developing the first-ever numerical study of three-phase CO_2 flow in a basalt fracture network, and (iii) quantifying the regional-scale permeability architecture of the Columbia River Basalt Group. These studies are integrated into a probabilistic assessment of industrial-scale CCS at the Wallula Basalt Sequestration Pilot Project. In pursuing this research, we consider (1) reservoir permeability is a first-order control on injection pressure accumulation and/or reservoir injectivity during CO_2 injections, and (2) the spatial distribution of *in situ* CRBG fracture distributions is a priori unknowable at scales of interest for industrial CCS operations, except within recovered drill cores. To address understand unsaturated flow characteristics in basalt fracture, we completed a set core-flood experiments to measure relative permeability and water saturation curves in basalt samples under variably saturated (CO_2 and brine) conditions. These laboratory results were utilized as input parameters for a Monte Carlo numerical modeling study of CO_2 injections under an industrial-scale CCS scenario for which CO_2 is injected at 95% of the regional fracture gradient. The Monte Carlo model comprised of 50 equally probable synthetic reservoirs in which fracture-controlled reservoir heterogeneity is the random variable, and borehole data from the Wallula Site (McGrail et al., 2009) are explicitly reproduced. By calculating the ensemble statistics from each Monte Carlo run (mean and variance of grid cell fluid pressure and CO_2 saturation), this project resulted in a site-scale risk assessment of for CCS at the Wallula Site. Results from this project are congruent with the Carbon Storage Program Goal “to improve reservoir storage efficiency while ensuring containment effectiveness” by addressing three of the six Geological Storage Technologies and Simulation and Risk Assessment (GSRA) Key Technologies: (1) fluid-flow, pressure, and water management; (2) geomechanical impacts; and (3) risk assessment (USDOE, 2013, Table 3-1). Moreover, the Monte Carlo modeling study based on equally probable reservoir permeability distributions is a generalizable and transferable risk assessment strategy for CCS deployment in any geologic environment.

2. MEASUREMENT OF RELATIVE PERMEABILITY OF A HORIZONTAL FRACTURE IN BASALTS

2.1 Objective

The object of this work is to study the multiphase flow behavior inside a fracture in a basalt rock and to measure the relative permeability curves. With this goal, we set up core flooding experiments to measure permeability and relative permeability. We also take X-ray CT images during the experiments to be able to calculate fracture aperture and water saturations in the fracture. The methods used to measure relative permeability and fracture aperture were previously developed in our research group (Huo and Benson 2015, Huo et al. 2016 and Huo and Benson 2016). We also took, as a starting point, the work done by Da Huo (Huo and Benson 2016). He used X-ray CT images to measure aperture and water saturations in a fractured sandstone core at two different effective stress levels, 300 and 800 psi. Figure 2.1 shows the resulting relative permeability curves at these two effective pressures.

In Figure 2.1 we can see that the system shifts quickly from one mode to another over a very small range in water saturation. At high water saturations, the relative permeability to water remains high, while the relative permeability to gas is very low. After a critical threshold, the relative permeability to gas increases quickly, while the relative permeability to water drops to near zero. After reaching the critical saturation, the water saturation remains nearly constant, but the gas phase relative permeability increases dramatically. This behavior suggests that the two phase are highly interfering.

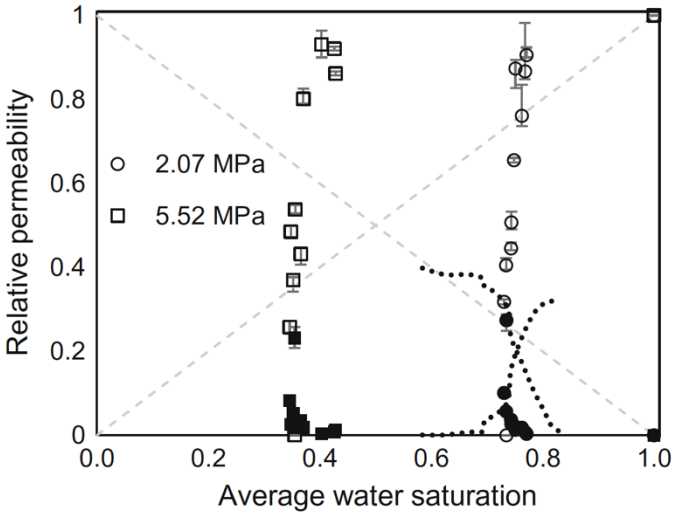

Figure 2.1: *Previous work from Huo and Benson (2016). Relative permeability curves obtained at 300 and 800 psi effective stress. Empty circles and squares show the wetting phase, and solid ones show the non-wetting phase. The error bars represent pressure drop fluctuations during the experiment. Dotted lines are Bertels et al. (2001) experiments.*

Although these results were quite surprising, it was not the first time that these type of relative permeability curves were measured (see Bertels et al. 2011). In our work, we want to repeat this procedure using a fracture in a basalt core , to see if we obtain similar results and to better describe the changes in saturation inside the fracture. To do so, we use the X-ray CT images and we also set up core flooding experiments using micro Positron Emission Tomography (PET), which will allow us to record dynamic images of the changes in the fluxes inside the fracture during the experiments.

2.2 Core flooding experiments combined with X-ray CT scan images

The samples used for the experiments are basalt cores from Columbia River Basalt Group. All the cores were collected from wells drilled at the Hanford Site as part of the characterization efforts that supported the Basalt Waste Isolation Project (BWIP) back in the late 70s to early 80s. Cores include intact and naturally fractured basalts. For these experiments, an intact core has been saw-cut in two to obtain a fracture (Fig. 2.2).

A total of eleven series of experiments have been carried out to study the multiphase properties of gas-liquid injection in a fractured rock under reservoir pressure and temperature conditions. Six of them are core-flood experiments combined with X-ray CT scanning images. The sample used is a basalt core 9'4cm long and 4'7cm diameter. The experiments have been conducted at 50ºC temperature and 300 psi effective pressure. Six pumps (Teledyne Isco) have been used in these experiments. Two double pumps to inject simultaneously liquid and gas, the pressure on the system is imposed by a back pressure pump (constant at 300psi) and a confining pressure pump (constant at 600psi) allows us to fix the effective pressure (at 300psi) and to confine the fluids inside the core. We use a two phase separator (TEMCO AMS-900) to separate the gas and liquid coming out from the core during the multiphase injection. Both phases are then redirected to the corresponding gas or water pumps to be available for reinjection. That way we keep the system closed and maintain the pressure during the experiment. Various heaters are used to keep the temperature at 50ºC inside the core and to inject gas and water at that same

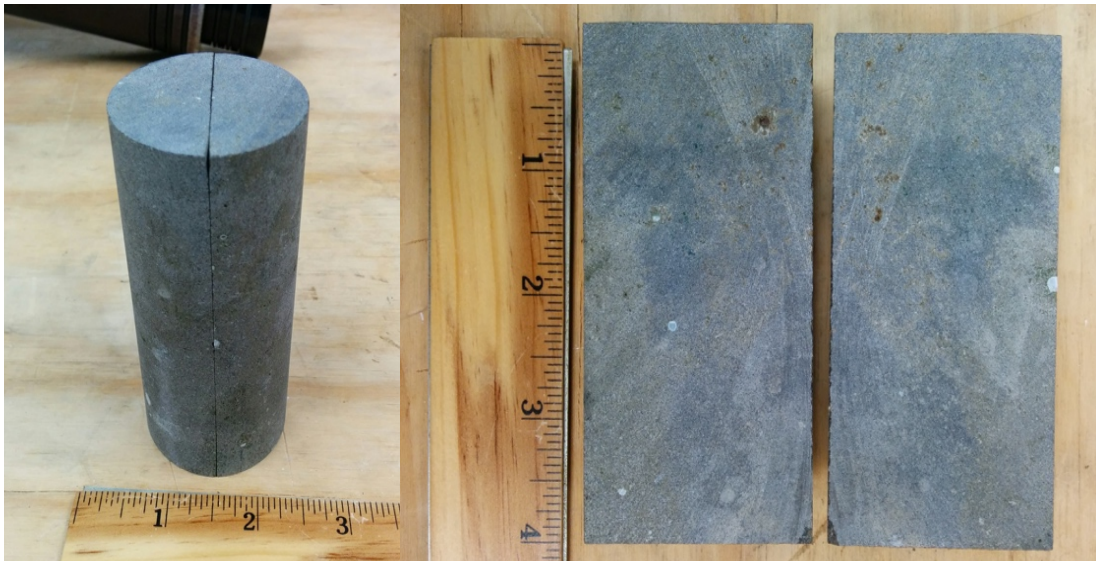

Figure 2.2: *Basalt core with a saw-cut fracture. The two surfaces can be seen on the right image.*

temperature. Pressure is measured at the inlet and at the outlet faces of the core by two high accuracy pressure transducers (Oil filled Digiquartz Intelligent Transmitter model 9000-3K-101). A simplified scheme of this core flooding set up is shown in Figure 2.3:

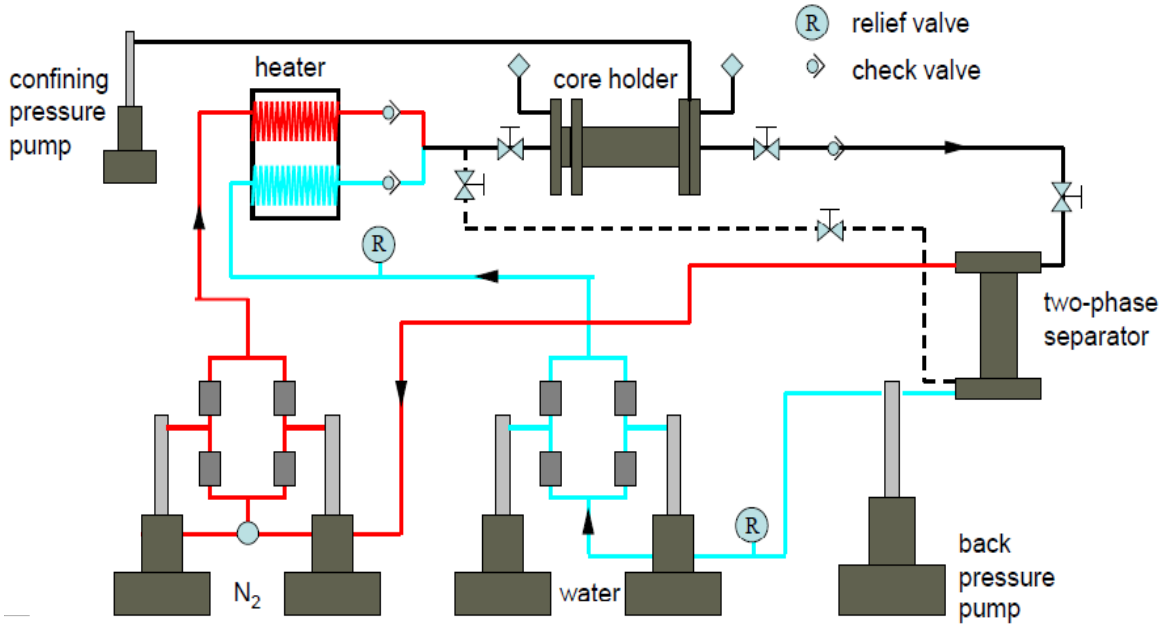

Figure 2.3: *Simplified scheme of the core flooding experiment (modified from Huo & Benson, 2016).*

Water is injected at different flow rates to obtain the fracture's water permeability. N_2 and water are co-injected at different ratios to calculate their relative permeabilities. The core-holder is placed in a medical X-ray CT scanner (General Electric Hi-Speed CT/I X-ray computed tomography) (Fig. 2.4) that is used to obtain the fracture aperture and water saturation during the core flooding experiments. The CT scanner radiates X-rays during discrete time intervals and relies on the electron density contrast between fluids to produce different levels of attenuation that generate a 3D image of the material. The following imaging parameters were applied: voxel dimensions of 0.18 x 0.18 x 0.625 mm, a tube current of 200mA and an energy level of 120KeV. With that, 113 slices along the core were recorded in every scan.

Figure 2.4: *On the left image, and from left to right, double water pump, back pressure pump and two phase separator. On the right one, the core-holder inside the medical X-ray CT scanner and the gas-liquid flux heater box.*

During the CT scans a slight displacement of the core was observed. To deal with this, we aligned every image set of the core and to be able to compare the results of different fluid injections all image sets from the different scans were registered. We also dealt with an heterogeneous matrix that contains some bubbles and mineral inclusions that generates errors when determining the position of the fracture from the CT scan images. To overcome that, we reduced the work area of the sample selecting only a rectangle that includes the fracture and we applied several image treatment techniques. In figure 2.5 it can be seen, on the left, the core used in the experiments, on the center, an image of the whole core obtained from the CT scan, and on the right, a slice of the core where the selected area is highlighted in red.

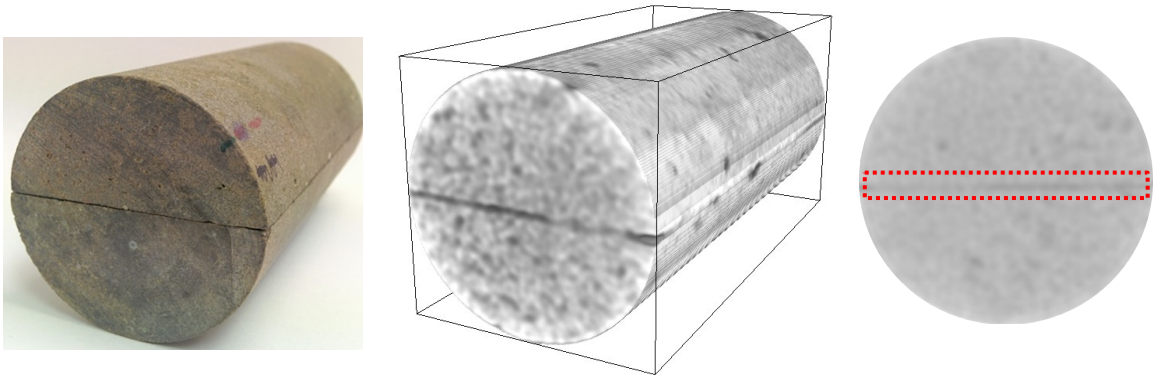

Figure 2.5: *On the left, the core used in the experiments, in the center, the image of the complete core obtained from the X-Ray CT scan and, on the right, the area used in the postprocessing calculations highlighted in red.*

Figure 2.6 shows the aperture map of the fracture along the core while it was still dry, at the beginning of the experiment. This is calculated from the data registered by the X-Ray CT scanner. The red areas reflect the largest apertures and the blue ones the smallest. The mean value of the fracture aperture is 26 μm and the median is 21 μm.

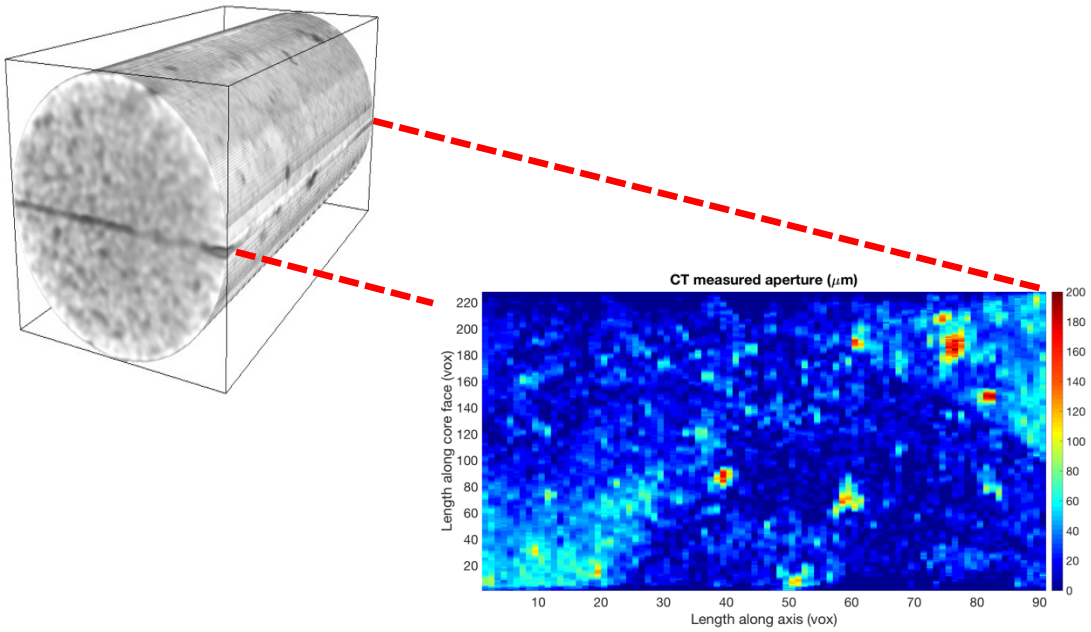

Figure 2.6: *Fracture aperture map obtained from the X-Ray CT images. Red areas represent the biggest apertures and blue areas the smallest ones.*

From this aperture map two areas with bigger apertures can be easily differentiated: the upper right corner and the lower left one, connected by a central zone that presents smaller aperture values.

Water permeability is obtained injecting water through the core at different flow rates and measuring the corresponding pressure drops between the inlet and the outlet of the core for each of these flow rates, and is calculated by means of Darcy's Law:

$$K = -\frac{Q\mu L}{A\Delta P}$$

Where Q is the water flow rate ($m^3\ s^{-1}$), μ is the water viscosity (0.000548 Pa s), L is the length of the core (m), A is the fracture aperture area (m^2) and ΔP is the pressure drop (Pa). The permeability obtained is $5 \cdot 10^{-11}$ m^2. Figure 2.7 shows the pressure drop versus the injection rate, where permeability is a function of the slope of the regression line ($Q/\Delta P = 8.6 \cdot 10^{11}$ m^3/Pa s).

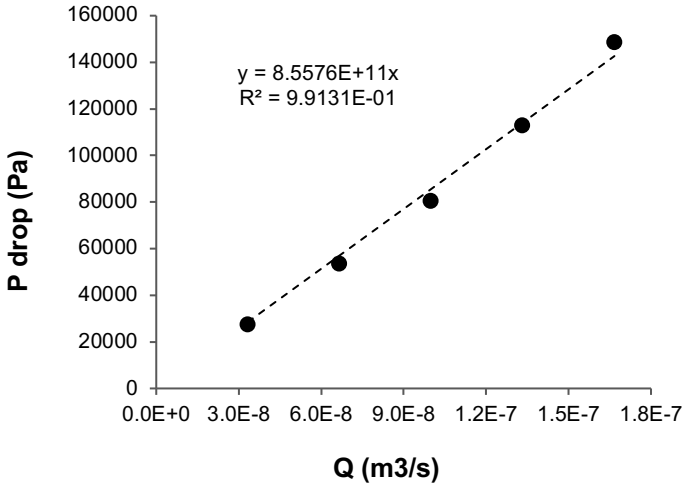

Q (m^3/s)	Δ*P* (Pa)	*K* (m^2)
1.67E-07	1.49E+05	4.63E-11
1.33E-07	1.13E+05	4.88E-11
1.00E-07	8.03E+04	5.13E-11
6.67E-08	5.34E+04	5.15E-11
3.33E-08	2.72E+04	5.05E-11

Figure 2.7: *Pressure drops measured between the inlet and the outlet of the core versus the corresponding water injection rates.*

This procedure was repeated for every experiment, obtaining very similar water permeability values, all in the range of 4 to 6E-11 m^2.

For the multiphase flow experiments we co-injected water and nitrogen at the total flow rate of 6mL/min. We start at 1% N_2 and 99% water and then we increase step-wise the fractional flow of nitrogen until it reaches 100%. Table 2.1 displays the different injection rates, the measured pressure drops and the calculated relative permeabilities and saturations.

Table 2.1: *Data from water-N2 co-injection at the total flow rate of 6mL/min.*

N_2 ratio (%)	Q_{N2} (mL/m)	Q_w (mL/m)	ΔP (psi)	Water k_{rel}	N_2 k_{rel}	Water Sat.
1	0.06	5.94	16	0.77	0.00027	0.967
5	0.3	5.7	17.7	0.67	0.0012	1
10	0.6	5.4	18	0.62	0.0024	1
45	2.7	3.3	13.4	0.51	0.0144	1
90	5.4	0.6	4.9	0.25	0.0789	1
99	5.94	0.06	2.1	0.06	0.2	1
100	6	0	1.1	0	0.39	1

Using the multiphase injection data, we can calculate the variation of both gas and water relative permeabilities with respect to the fraction of gas (Fig. 2.8).

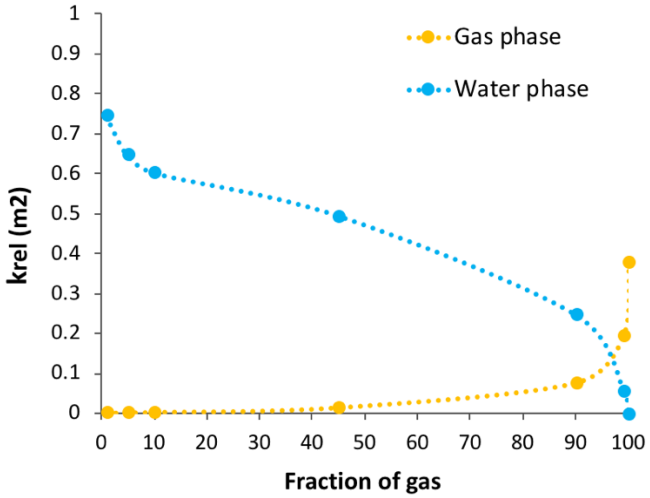

Figure 2.8: *Water and N_2 relative permeabilities versus fraction of gas.*

These data show how multiphase flow shifts quickly from being dominated by one phase, liquid, to another phase, gas, after a critical value of the gas phase saturation, implying that both phases are very interfering. Gas relative permeability is close to zero until fractional flow of gas is close to the 90%. From this point, water relative permeability decreases precipitously while the gas relative permeability raises sharply. When plotting the variation of both gas and water relative permeabilities with respect to the degree of water saturation (Fig. 2.9), we see that the relative permeability curves move over a small range in water saturation and close to the maximum value.

This suggests that gas is not displacing water from the fracture, but we know that this is not entirely true because we had some water coming out from the core. We plot the saturation maps along the fracture (Figure 2.10) for the 1% N_2 and 99% N_2 fractional flows to see the changes in saturation during the multiphase injection. Yellow indicates the maximum water saturation. If we compare them we can see that they are almost identical, so we are not capturing the entry of the gas and the consequent water displacement out of the fracture.

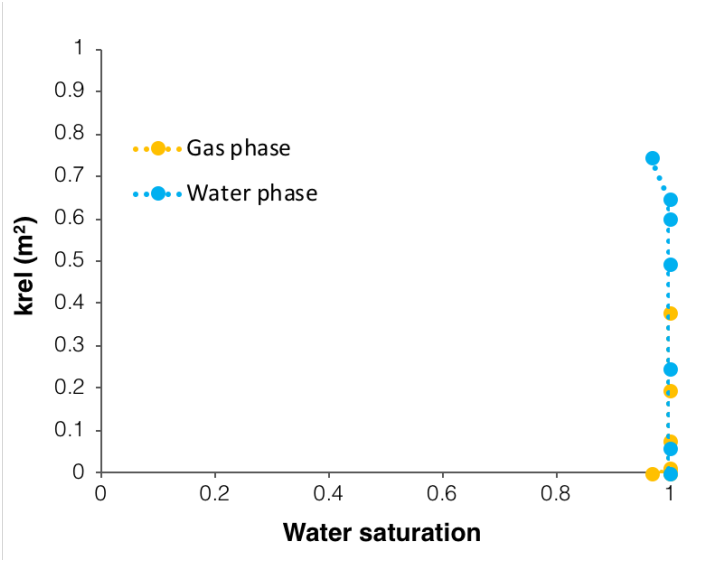

Figure 2.9: *Water and N_2 relative permeabilities versus degree of saturation.*

Analyzing these experimental results, we concluded that the contrast between the gas and the liquid during the multiphase injection is too small to differentiate them so we cannot obtain accurate saturation measurements from the X-Ray CT images. As a result, we modified our experiments by using a solution of NaI salt instead of water, to increase the contrast between the liquid and the gas phase during the multiphase injection. A 100,000 ppm, 10% in weight, NaI solution was used. The results showed that the change in contrast due to the tracer was insufficient and did not change the saturation values obtained.

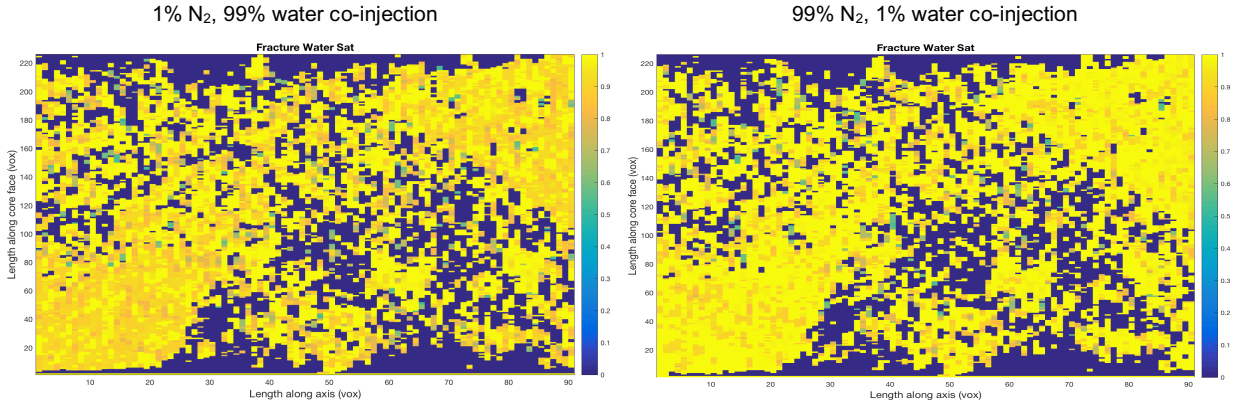

Figure 2.10: *Fracture water saturation maps for two different steps during the multiphase injection. On the left, 1% N2 and 99% water and on the right, 99% N2 and 1% water.*

We also tried applying different image processing techniques to better locate the pixels of the fracture where the fluids flow during the multiphase injection, but none of these improved the water saturation measurements.

With the aim to differentiate the two phases (gas and liquid) during the co-injection, we used micro Positron Emission Tomography (PET) for imaging the fracture flow. The use of radiotracers mixed with the liquid phase should allow to clearly separate the two phases. This technique will also provide dynamic information about flow behavior in the fracture.

2.3 Core flooding experiments combined with micro-PET scan images

The micro-PET scanner (Fig. 2.11) relies on detection of photon emissions produced during radioactive decay of radiotracers injected into a material. The coincident photon events are collected continuously by a cylindrical array of photon detectors that surround the core. These events can be binned temporally to create time lapse frames of the scan that can be as short as 10–20 seconds. From the resulting data, it is possible to produce quantitative four-dimensional images of the radiotracer transport in the core during single and multiphase flow experiments.

A total of five experiments (Test 1 to 5) have been conducted using 18F (Fluorine radioisotope) as a radiotracer mixed with the water. The same fractured basalt core from the CT scanner experiments was used.

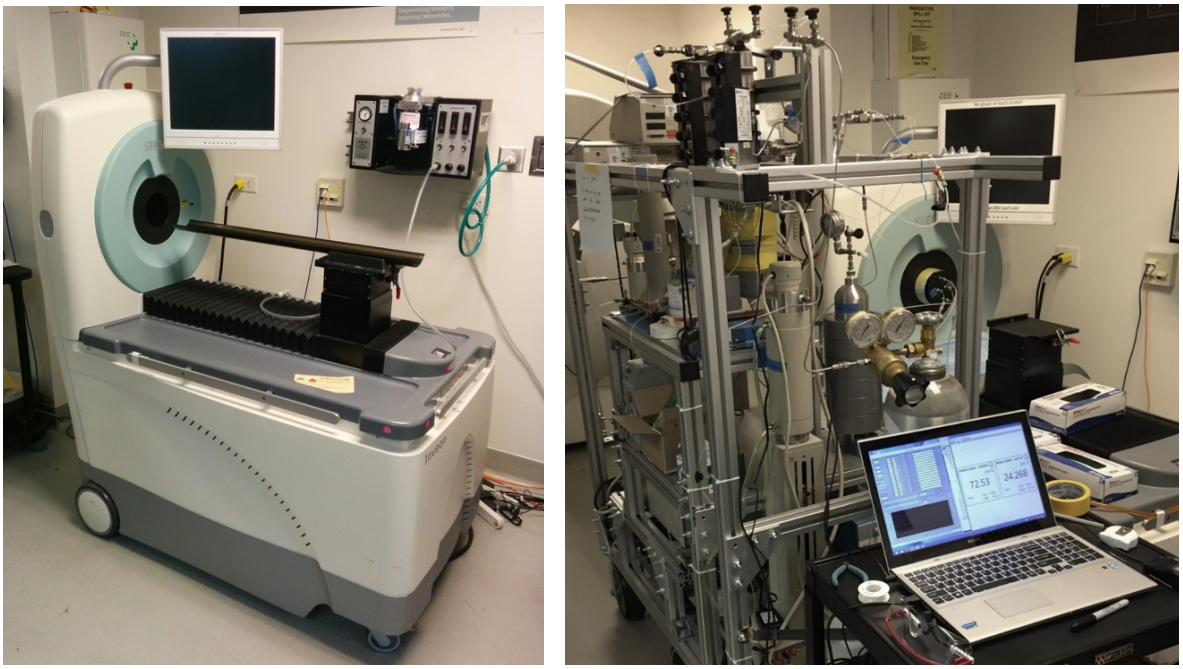

Figure 2.11: *On the left, micro-PET imaging scanner, on the right, our set up during the experiments.*

The same core flooding experiment set up from the CT experiments was used in the PET ones. Just a few modifications were necessary to protect us from the activity coming from the tracer.

Test experiments (Tests 1 and 2)

The purpose of these first two experiments was to establish the concentration of radiotracer needed to be able to see the water flux through the fracture and the different fractional flows to use in the multiphase experiments. Since we are now constricted by the life time of the radiotracer, we have limited time, thus we need to reduce the number of steps of the multiphase injection. Test 1 was a single phase (radio tracer mixed with water) and two different injections were carried out: a long injection at a low flow rate (45 min at 0.6 mL/min) and a short pulse at a higher flow rate (20 min at 3 mL/min). Figure 2.12 shows the recorded tracer curves at the inlet (blue line) and at the outlet (red line) of the core during the injections. From these curves we can see that the concentration of radio tracer in the water wasn't identical (the top of the curves should be horizontal). Thus, for Test 3 and 4 we decided to mix the radio tracer and the water for a longer time to get a uniform solution of the tracer in the injected water.

Test 2 consisted of a multiphase injection, water and N_2, but no radiotracer was used. Total flow rate injection of 5 mL/m and 350 psi effective pressure. The experiment started with the core fully saturated with water and then the nitrogen concentration was increased step-wise until 100% of nitrogen fractional flow was achieved: 50, 80 90, 95, 99% N_2 steps. The resulting water and gas relative permeabilities versus fraction of gas are shown in figure 2.13. As expected, the results are very similar to the ones obtained from the CT scan experiments (Fig. 2.8) were we saw that the two phases are very interfering.

These first 2 tests were also useful to check that all the water was flowing through the fracture and to see how much tracer was needed to be able to measure differences between the various gas/water ratios used during the multiphase flow experiments.

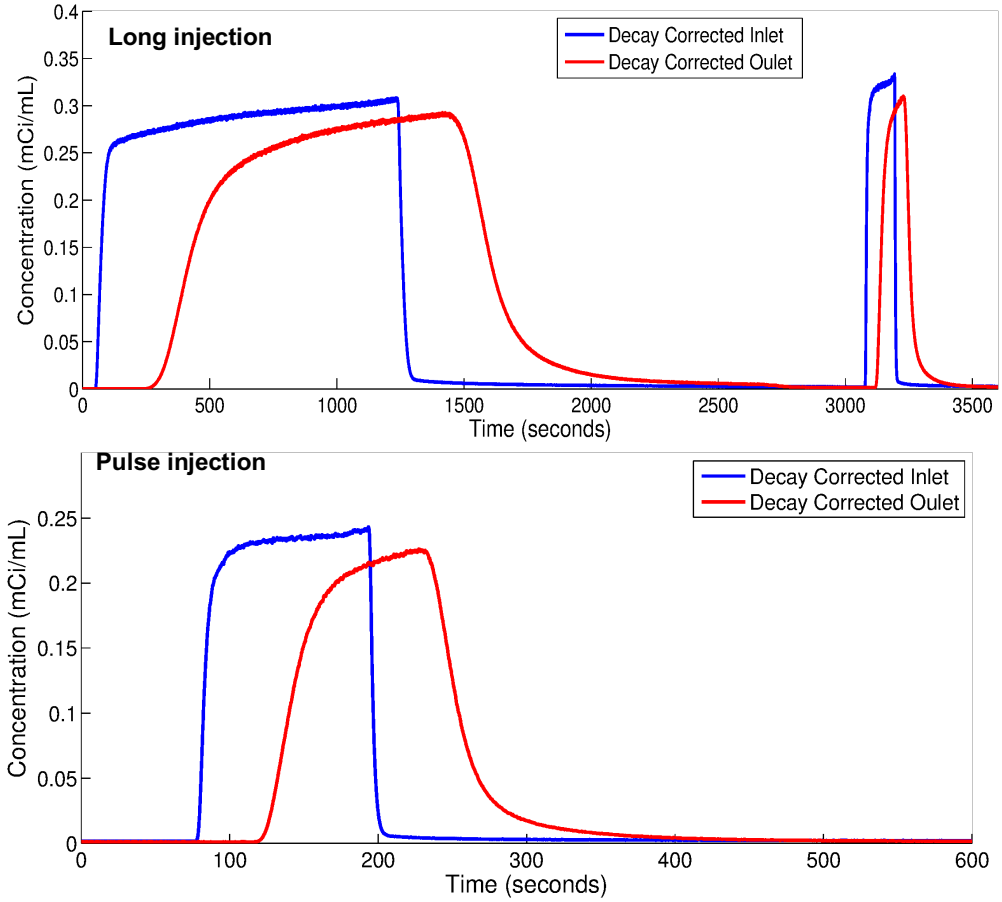

Figure 2.12: *Tracer curves measured at the inlet (blue line) and outlet (red line) for 2 injections during Test 1.*

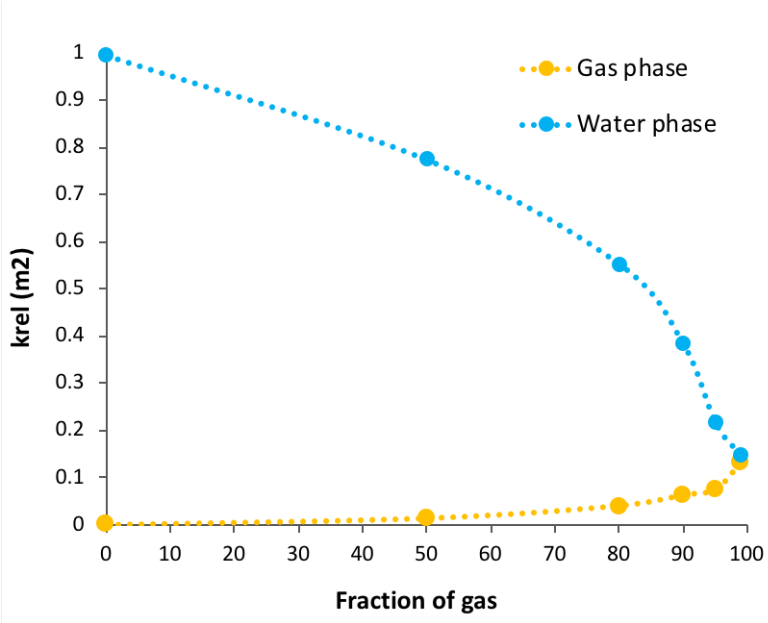

Figure 2.13: *Water and N2 relative permeabilities versus fraction of gas.*

Figure 2.14, left image, shows an example of the images resulting from the PET scans. The flows were injected form the right side to the left. The brighter areas point the location of the higher tracer concentrations, thus the areas with higher water content. There are two main areas where most of the water is concentrated, the upper right corner (at the entry) and the lower left corner (close to the exit of the fracture). The flow in these two areas seem to be connected through a central path where the tracer concentration is lower (less bright) but still visible and they conform what looks like a main path for flow. Notice how this path matches the regions where the fracture is wider (red to green pixels) in the fracture aperture maps from the CT scanner (Fig. 2.14, right image).

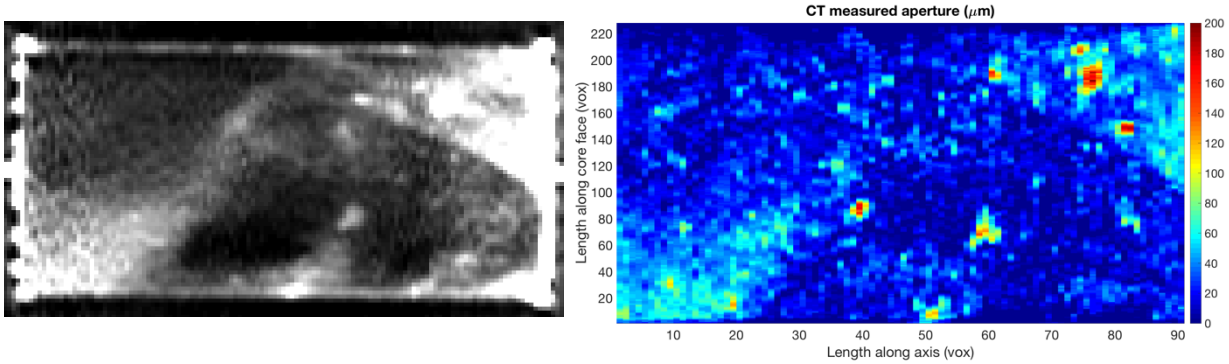

Figure 2.14: *On the left, image from the PET scan with the tracer flowing through the fracture (bright areas point higher tracer concentrations and thus higher water content). On the right, fracture aperture map obtained from the CT scan.*

Multiphase experiments (Tests 3 and 4)

Test 3 and 4 are both multiphase experiments co-injecting different ratios of N_2 /water with tracer. Total flow rate injection of 5 mL/m and 350 psi effective pressure. Both tests started with a fully saturated core. The first step is to inject CO_2 in the core until fully saturated, then water is injected to dissolve the CO_2 and to carry it out of the fracture. On that way, we are sure that there is no gas phase in the fracture so it is fully saturated with water. Afterwards, the multiphase injection starts, the nitrogen concentration is increased by steps until 100% nitrogen is reached. The steps to increase the N_2 during Test 3 (Fig. 2.15) were: 50, 80 90, 95, 99 and 100% N_2.

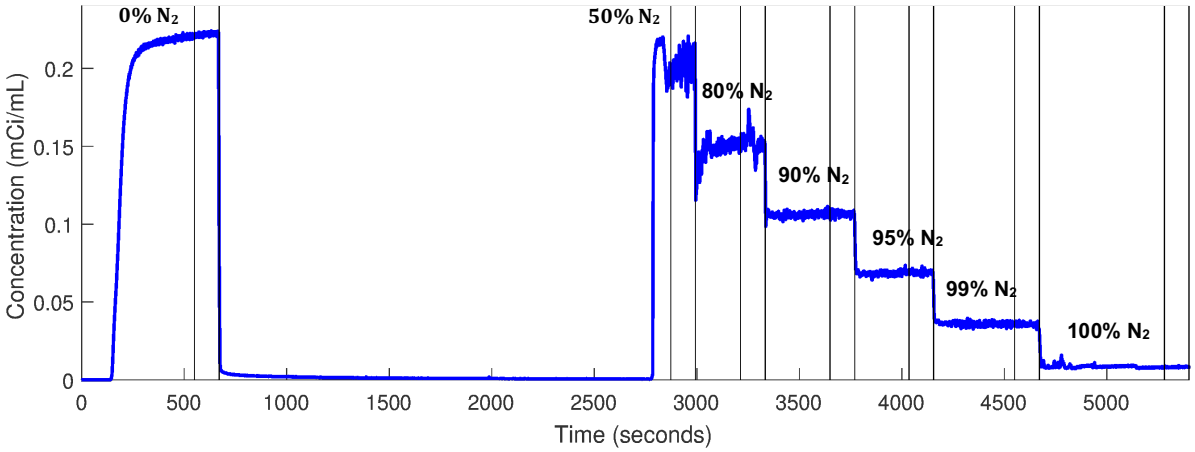

Figure 2.15: *Tracer concentration at the inlet for the different steps (increasing gas/water ratio) during Test 3.*

From the PET scan data we obtain tracer activity maps for the different gas/water fractional flows (Fig. 2.16). The fluids are injected from the right side of the images and the outlet is on the left side. In yellow the higher radiotracer activities and in blue the lower ones. It can be seen how for all the different ratios the water always flows through the main flow path (yellow pixels).

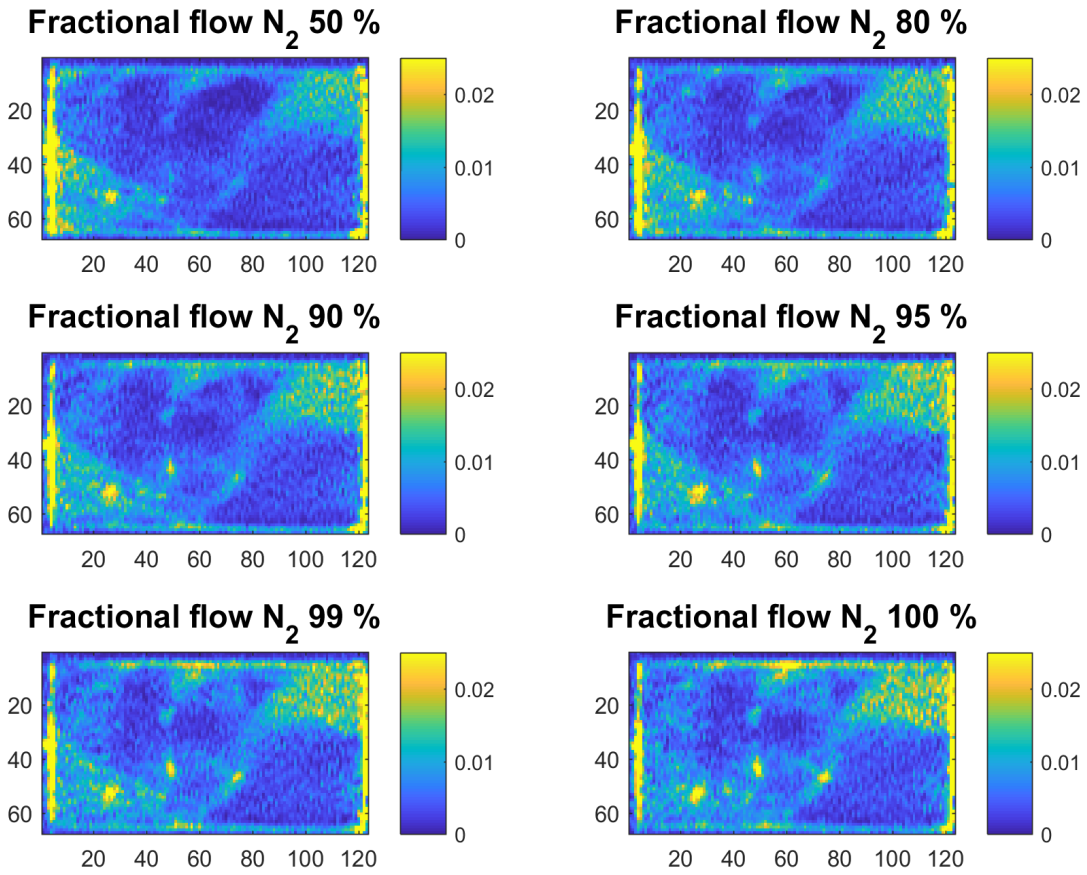

Figure 2.16: *Activity maps for the different gas/water ratios obtained from the PET scan data. In yellow the higher activities (higher water saturation) and in blue the lower activities (higher gas saturation).*

After this experiment, we concluded that to help differentiate changes in the activity, higher tracer concentrations were needed. As the tracer radioactivity decreases with time, we also shortened the experiment by decreasing the number of steps. As we have seen before, Figures 2.8 and 2.13, the gas relative permeability doesn't increase until the gas/water ratio is close to 90% N_2, so we decided to do the experiment at the highest gas ratios to be able to capture the variations when the system is changing from liquid to gas dominated. For Test 4, the ratios used were: 90, 98 and 99.5% N_2 (Fig. 2.17).

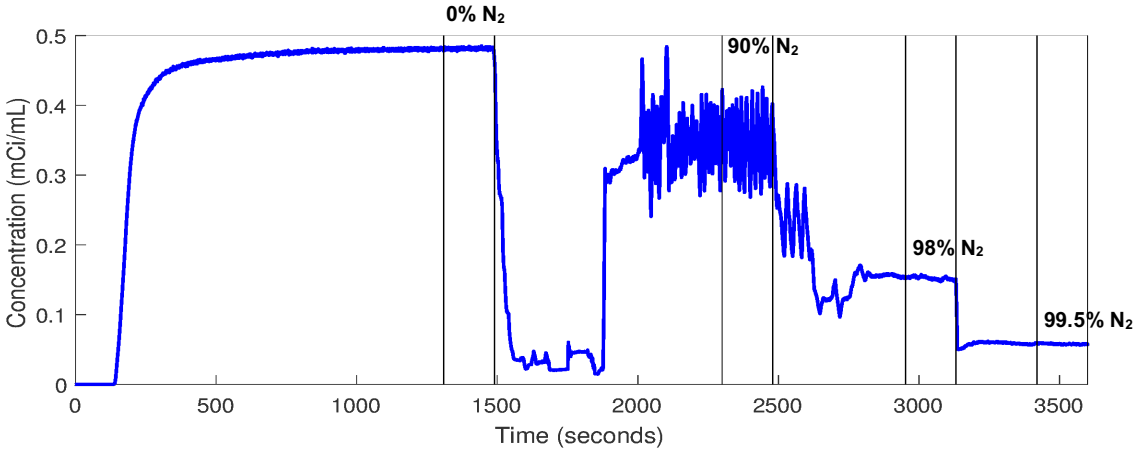

Figure 2.17: *Measured tracer concentration at the inlet for the different gas/water ratios during Test 4.*

Figure 2.18 displays the resulting tracer activity maps for the different gas/water ratios calculated during Test 4. The inlet is on the right side of the images and the outlet is on the left side. In yellow the highest activities and in blue the lowest. The yellow pixels are pointing the areas where water is flowing and the change from yellow to blue indicates where the nitrogen is displacing the water.

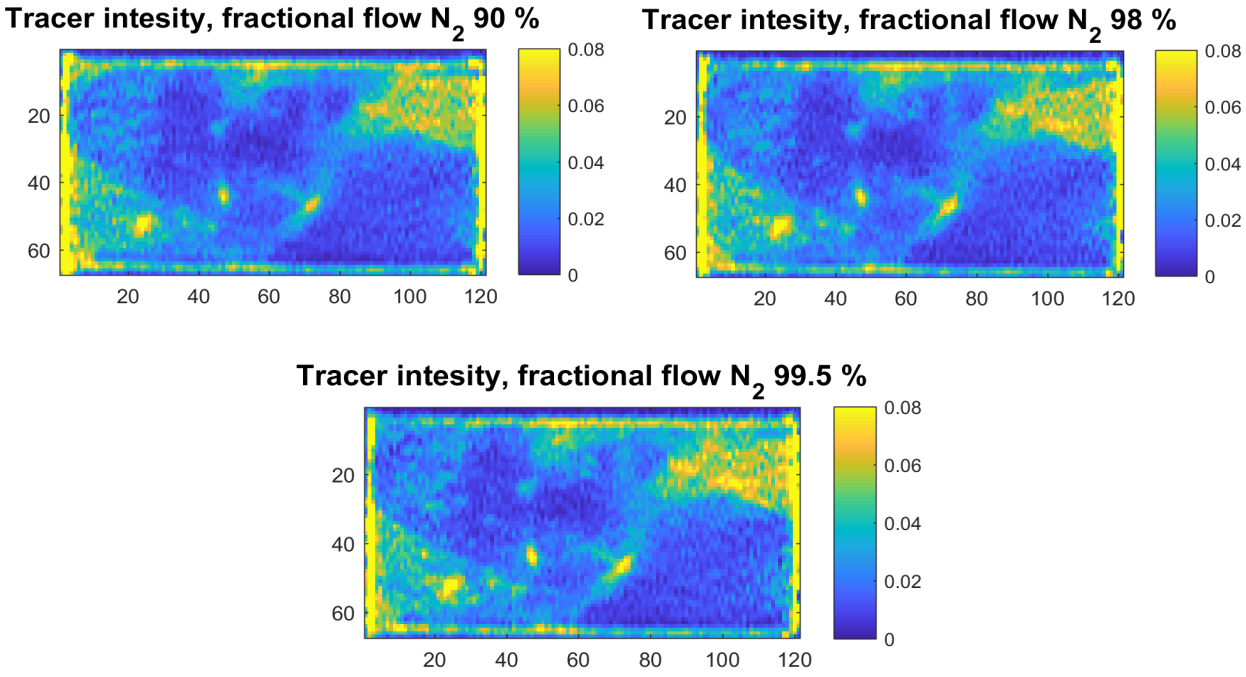

Figure 2.18: *Activity maps for the different gas/water ratio obtained from the PET scan data during Test 4.*

The data from these activity maps is then used to calculate the water saturations in the fracture. To do that, we work with the evolution of the activity in the fracture (Fig. 2.19).

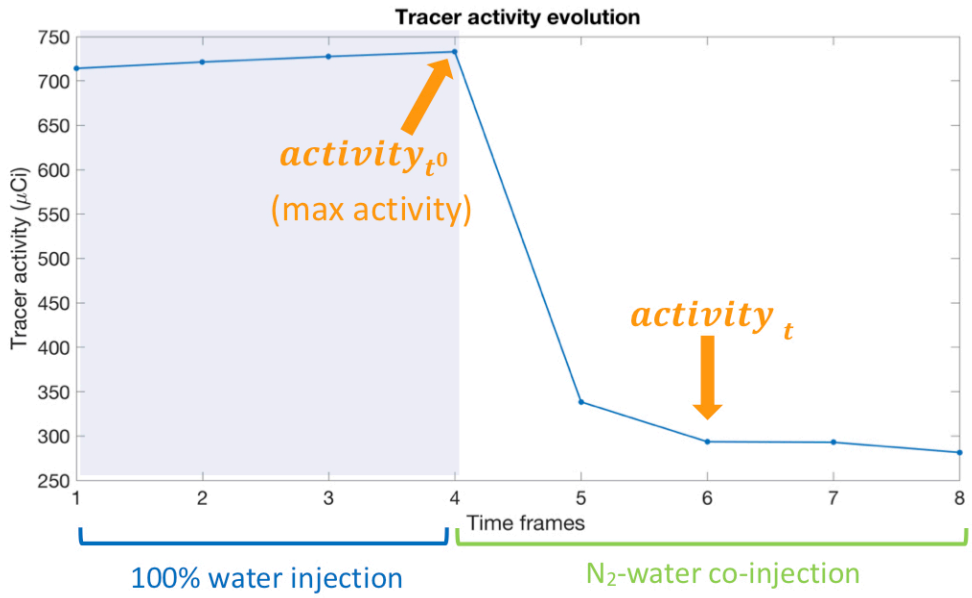

Figure 2.19: *Radiotracer activity evolution in the fracture during the multiphase experiment.*

We consider the activity value registered before starting the gas injection as the one representing full saturation (100% water) and the maximum possible activity in that pixel. Once co-injection starts, tracer activity diminishes (as water content does). By comparing the activities measured in each of these steps (90, 98 and 99.5% nitrogen) with the one with 100% fractional flow of water, we can calculate the corresponding degree of saturation as:

$$S = activity_t / activity_{t^0}$$

The pixel-by-pixel calculations of the saturation changes over time showed that the saturation of water appeared to be increasing over time in some regions of the fracture. We identified two possible explanations: first, the existence of diffusion into the matrix, and second, the tracer was not distributed uniformly throughout the fracture at the beginning of the multiphase injection. Both scenarios could lead to an increase in activity in the fracture over time (and the consequent larger than 1 saturation values), but the first would take place in the matrix close to the fracture and the second would be spread through the fracture itself.

With the aim of checking whether there was tracer diffusion into the matrix, we plot cross sections of the activity perpendicular to the fracture with increasing time. Figure 2.20 shows the tracer activity along the cross section for five different times.

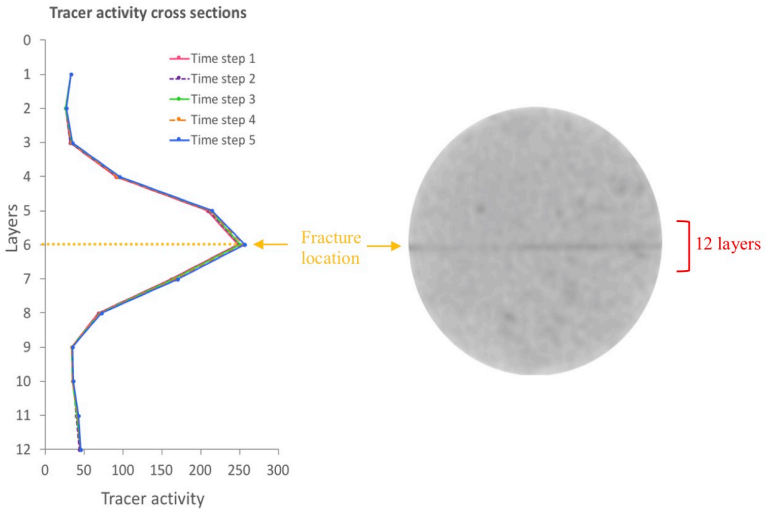

Figure 2.20: *Tracer activity cross sections perpendicular to the fracture at five different times.*

This graph displays the sum of the tracer activity for every layer (from the 12 core central layers that contain the fracture). Each layer is 1 pixel wide. These layers are horizontal planes along the core and parallel to the fracture, so the tracer activity is the sum of the activity of all the pixels conforming each layer. Layer six is where the fracture is located, but due to the nature of the PET scan data, the tracer signal is spread through more than one layer (from 4 to 8 approx.). The layers that go from 1 to 3 are matrix pixels above the fracture and layers 9 to 12 are the matrix below. From that graph can be seen that the activity does not increase over time out of the fracture (layers 1-3 & 9-12), so the existence of matrix diffusion can be eliminated.

Looking at figure 2.20, it can also be seen that the concentration of tracer in the fracture (layers 4 to 8) decreases less than expected with time. When gas is displacing water, the activity should clearly decrease at each step. That suggests that there is an increase in concentration of tracer in the aqueous phase that counteracts the decreases in activity due to the gas entry. This is consistent with the hypothesis that the tracer was not uniformly distributed through the fracture before starting the gas injection.

To study this phenomenon, we evaluated the activity evolution slice by slice and found that there are pixels showing an increase in concentration during the multiphase injection, even while the gas ratio is increasing (Fig. 2.21).

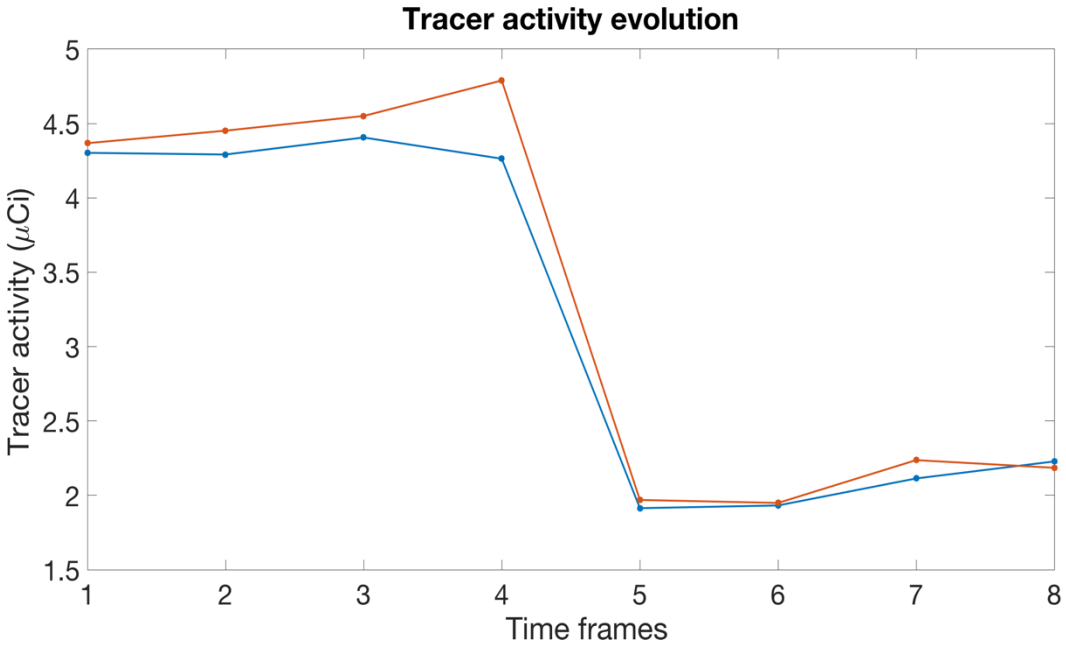

Figure 2.21: *Example of areas that show an increase of tracer activity while increasing the gas/water ratio during the multiphase co-injection.*

The increase in tracer activity appears to be caused by the presence of very low permeability regions in the fracture that that do not get fully swept by the tracer solution prior to starting the gas injection. These pixels have been identified and removed from the calculations leaving only the ones who had reached full tracer saturation at the beginning of the multiphase experiment. If we plot again the activity in the cross sections, now only for the central layers that contain the fracture, we can see that the activity decreases in all the layers at every step of the multiphase injection (Fig. 2.22). For each of these time frames, the tracer activity decreases all along the cross section.

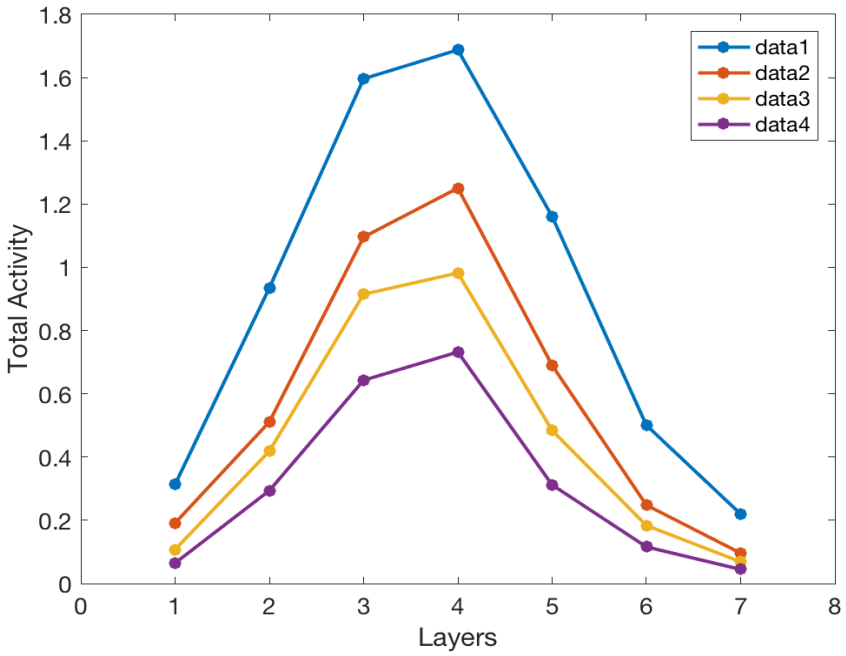

Figure 2.22: *Cross sections of the tracer activity perpendicular to the fracture for four different gas/water ratios after discarding some pixels (data1=100% water, data 2, 3 and 4 correspond to 90, 98 and 99.5% N2 respectively).*

From this analysis, it is clear that the majority of the fracture is not participating in either single or multiphase flow due to with the small apertures and/or the lack of a connected pathway with the inlet of the fracture. To identify systematically those portions of the fracture that are not part of the main flow path within the fracture, we apply the following procedure. First, we superpose the images from the X-ray CT and PET scans. As a result, we can plot the fracture aperture versus the tracer activity for every pixel in the fracture (Fig. 2.23). If the aperture were completely filled with tracer we would expect a liner relationship between the size of the fracture aperture and the amount of activity. As shown in Figure 2.23, there are many areas where the activity is far lower than expected based on the aperture. This is indicative of regions where there is not a connected pathway between the inlet and these portions of the fracture with larger apertures. To eliminate these regions from the analysis, we apply three different filters: 1) 2.5 times the standard deviation around the regression line between the aperture and activity, 2) a minimum activity value (0.02 μCi), and 3) a minimum aperture value (3 μm). We consider the activity values lower than this threshold to be noise and the apertures smaller than 3 μm to not be accessible for flow. The pixels out of these filters are discarded and then we plot the aperture versus the activity for the remaining ones. After that, the fracture aperture map is plotted again only with the remaining pixels to check the reliability of our selection (Fig. 2.24).

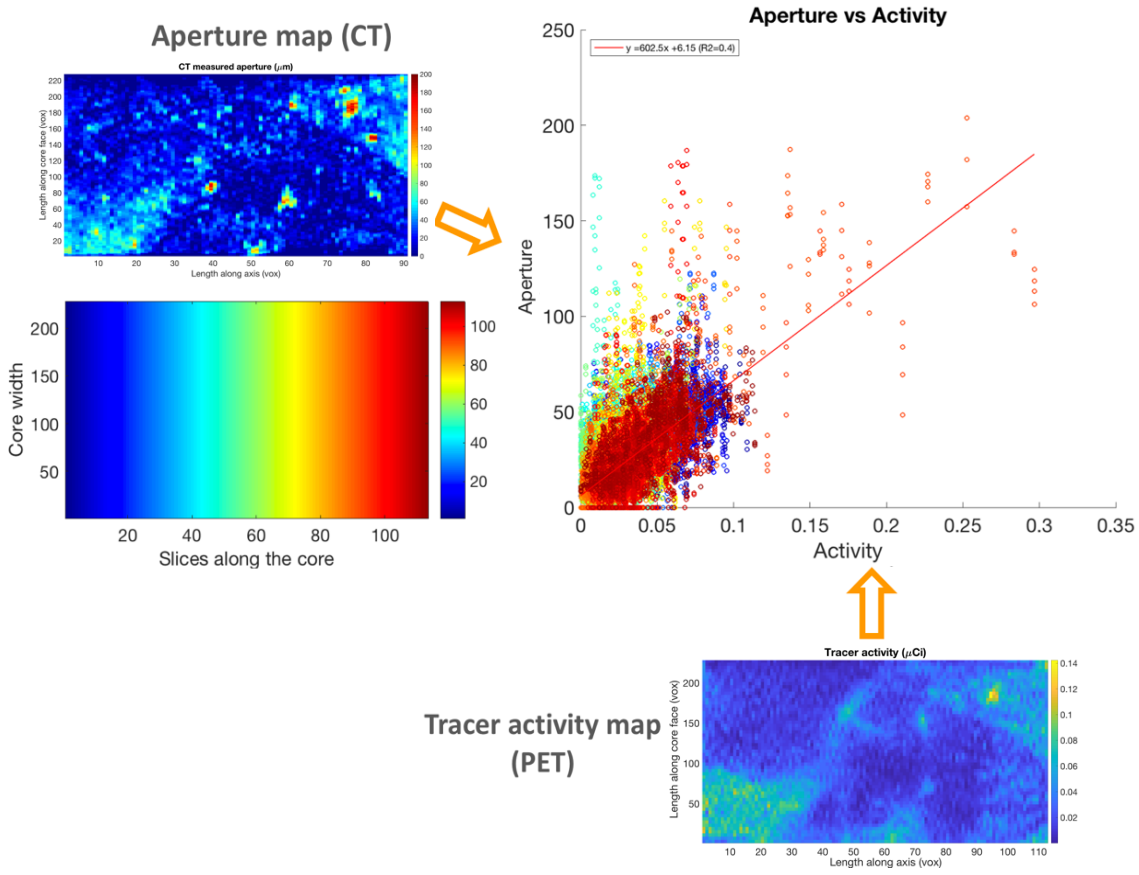

Figure 2.23: *Fracture aperture (from the CT scans) plotted versus tracer activity (from the PET scans) per pixel. The color map on the left low corner displays the colors assigned to each slice along the core.*

The fracture map on the right (Fig. 2.24) shows that the pixels that remain after applying the filters, where water is flowing thus the tracer is well distributed, match the areas that we previously identified as a main flow path. That gives us confidence on the results obtained using these filters. Now, we calculate again water saturation along the fracture using these remaining pixels. Figure 2.25 presents the final calculated saturations by pixel. The average saturation for each of these steps is: 0.75 for the 90% N_2, 0.74 for the 98% N_2 and 0.74 for the 99% N_2. Because these changes in water saturation aren't large, is difficult to visually see the differences in the saturation maps (Fig. 2.25) but they are taking place mainly in the area close to the inlet (right side of the maps) and, in a smaller amount, all along the main flow path.

Taking this into account, now we plot the relative permeability curves (Fig. 2.26). Note that the points show the data that has been measured during the experiment and the discontinuous lines are estimations of what we would measure if we had worked in a wider range of fractional flows.

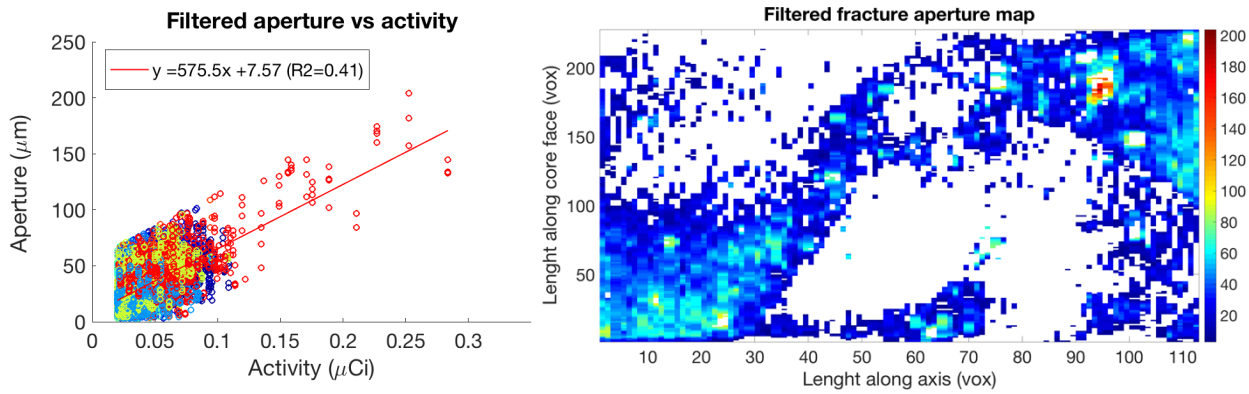

Figure 2.24: *On the left, fracture aperture plotted versus tracer activity using the remaining pixels after applying the filters. The fracture aperture map on the right displays the distribution of the remaining pixels along the fracture.*

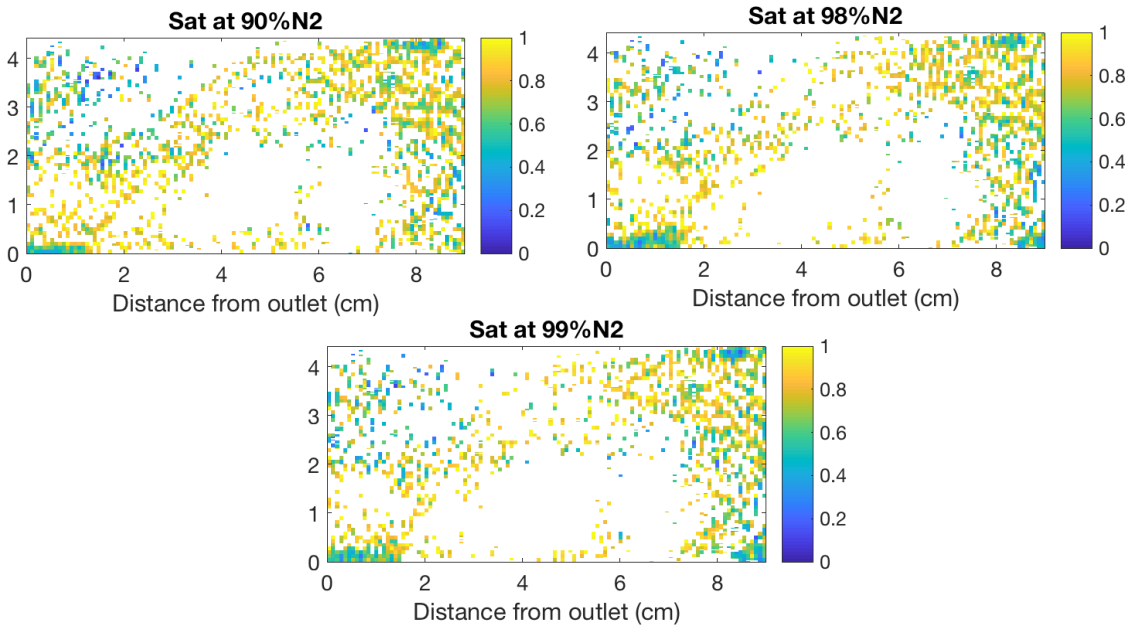

Figure 2.25: *Water saturation maps for the different gas/water ratio (90, 98 and 99.5% N2) during Test 4.*

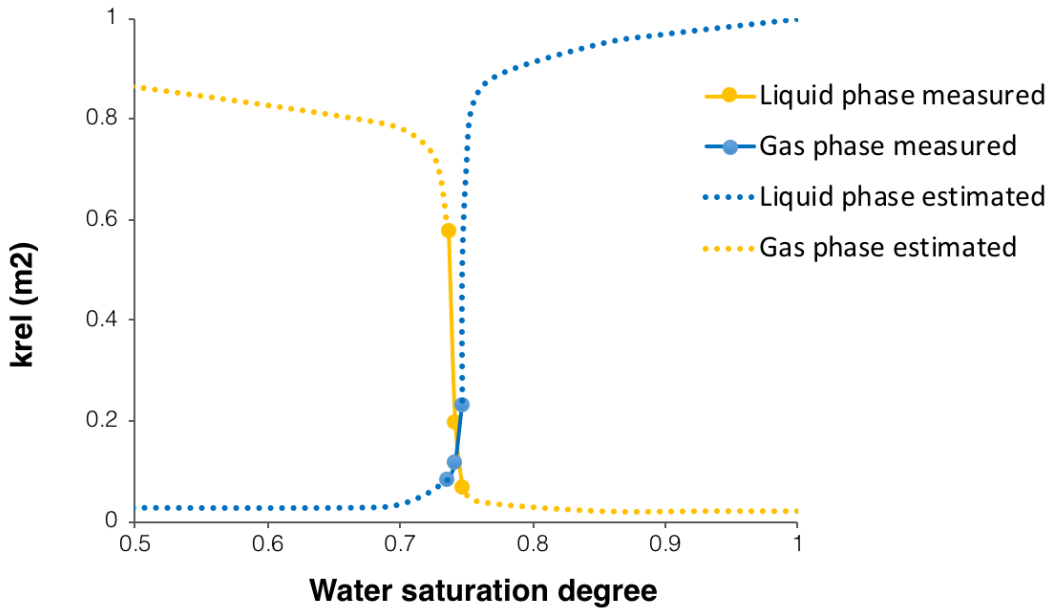

Figure 2.26: *Gas and liquid phase relative permeability curves for the multiphase injection of Test 4. The points are the data measured during the experiment and the discontinuous lines are estimations of what we would measure if working in a wider range of water saturation degrees.*

Next table (Table 2.2) summarizes the gas-water ratios and the water and gas flow rates used during the multiphase injection together with the calculated saturations and relative permeabilities.

Table 2.2: *Data from the water-N2 co-injection for Test 4*

N_2 ratio (%)	Q_{N2} (mL/m)	Q_w (mL/m)	Water k_{rel}	N_2 k_{rel}	Water Sat
90	4.5	0.5	0.234	7.26E-02	0.747
98	4.9	0.1	0.119	2.01E-02	0.741
99.5	20	0.1	0.084	5.82E-01	0.736

These relative permeability curves (Fig. 2.26) change abruptly in a small range of water saturation showing that the two phases are highly interfering and that the system changes quickly from being water dominated to being gas dominated. It also points out that the residual water saturation in the fracture is high, thus gas has a hard time displacing water from the fracture. We infer that gas displaces the water located in the wider apertures of the main flow path, leaving behind films of water trapped on the walls and small cavities of the fracture.

Based on this methodology for calculating water saturation in fracture, we decided to repeat the experiment with a more uniform distribution of the tracer in the fracture, so we can calculate the relative permeability curves using a bigger number of the pixels located in the main flow path.

Multiphase experiments (Tests 3 and 4)

To get a more uniform tracer distribution along the fracture, we applied some changes in the single-phase injection part of the experiment. In test 5, we injected the water mixed with radiotracer at a lower flow rate and for a longer period of time (0.1ml/min during approx. 60 minutes instead of 1ml/min during 10 minutes). After that, we started the multiphase injection increasing the N_2 ratio while keeping constant the capillary number at 2.09E-6. The steps, injection rates, we followed were: 84, 94, 98 and 99.8% N_2. Table 2.3 summarizes the gas-water ratios and the water and gas flow rates used during the multiphase injection together with the calculated relative permeabilities.

Table 2.3: *Data from the water-N2 co-injection for Test 5.*

N_2 ratio (%)	Q_{N2} (mL/m)	Q_w (mL/m)	Water k_{rel}	N_2 k_{rel}
84	2	0.38	0.77153711	1.40E-01
94	5	0.33	0.47399696	2.48E-01
98	10	0.238	0.43973212	6.37E-01
99.8	20	0.05	0.20956457	2.89E+00

We follow the same post-processing procedure. The images from the CT scans (aperture map) and from the PET scans (tracer activity maps) are superposed so aperture and activity can be plotted one against the other (Figure 2.27).

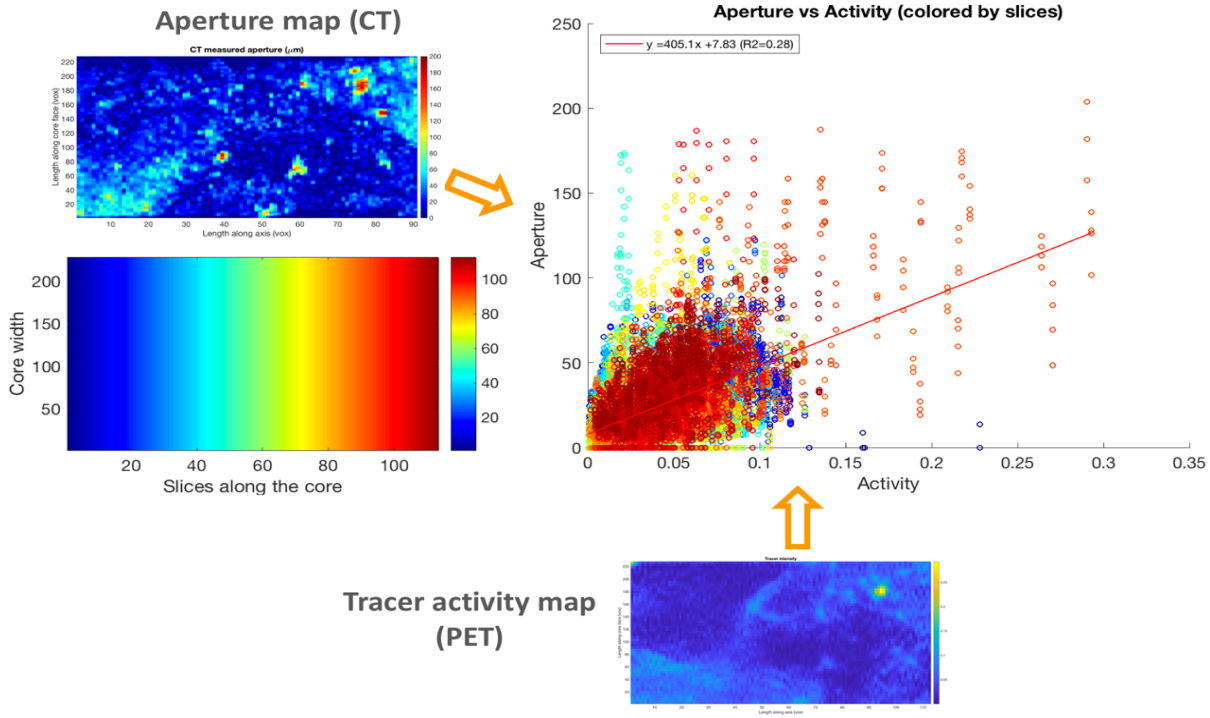

Figure 2.27: *Fracture aperture (from the CT scans) plotted versus tracer activity (from the PET scans) per pixel. The color map on the left low corner displays the colors assigned to each slice along the core.*

As seen in Test 4, the relationship between the fracture aperture and the tracer activity is not linear, so again there are pixels where the activity is not increasing as the aperture does. We apply again the three filters: one standard deviation, a minimum activity value (0.025 μCi) and a minimum aperture value (3μm). The pixels out of these filters are discarded, then we plot the aperture versus the activity for the remaining ones and we also plot the fracture aperture map only with the remaining pixels to check the reliability of the selection (Fig. 2.28).

The fracture map on the right (Fig. 2.28) shows that the pixels that remain after applying the filters, where water is flowing thus the tracer is well distributed, match again the areas that we previously identified as a main flow path.

Now, as we did for Test 4, we calculate the water saturations along the fracture using these remaining pixels (Fig. 2.29). Looking at these maps, Figure 2.29, we can see that we lose pixels as we increase the nitrogen ratio at each multiphase step. These discarded pixels are due an increase in activity from one step to the next one, so the tracer was not well distributed along the fracture this time either.

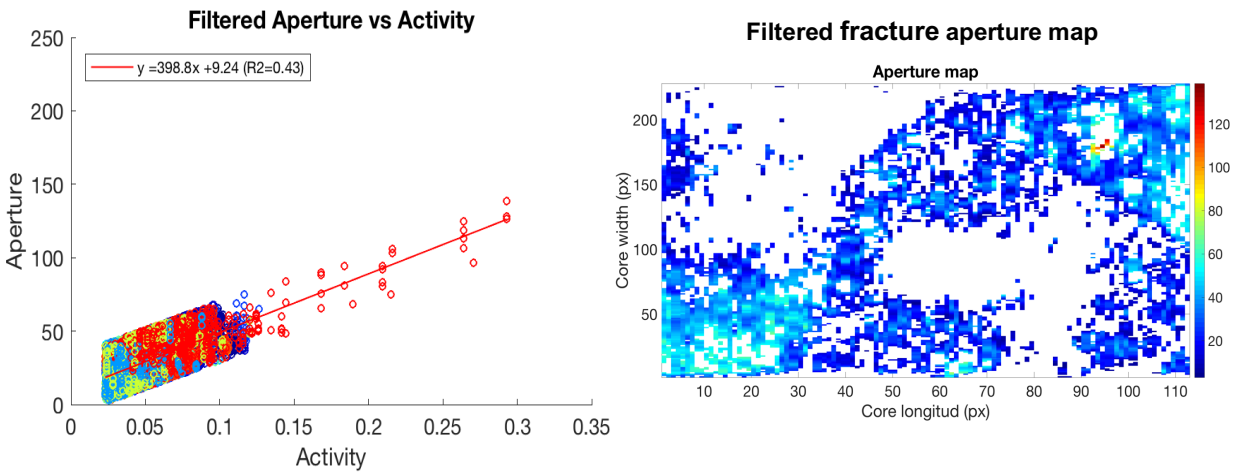

Figure 2.28: *On the left, fracture aperture plotted versus tracer activity using the remaining pixels after applying the filters. The fracture aperture map on the right displays the distribution of the remaining pixels along the fracture.*

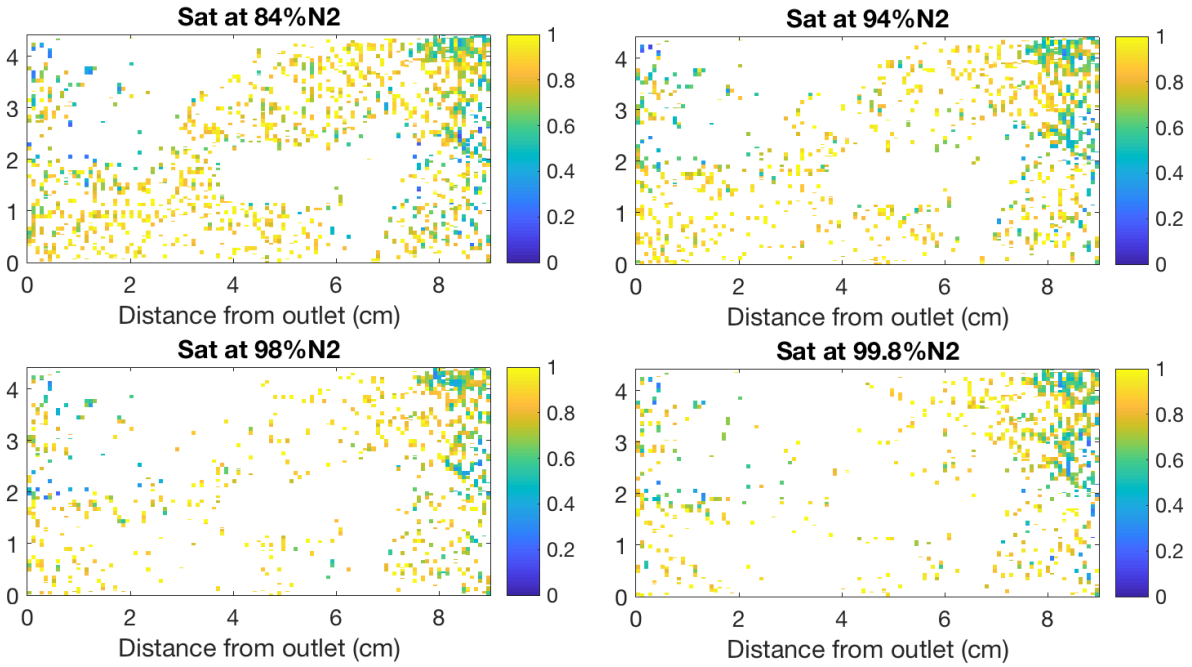

Figure 2.29: *Water saturation maps calculated for the different gas/water ratio (84, 94, 98 and 99.8% N_2) in Test 5.*

2.4 Summary

Based on this work we can draw several conclusions:

- Combining core flooding experiments with X-ray CT and micro-PET scans we can calculate the relative permeability curves for a horizontal fracture in basalt.
- The relative permeability curves obtained in these experiments are similar to those obtained from Huo and Benson (2015) and Bertels at all (2001) for flow in fractured sedimentary rocks. This suggests that for fractures in real rocks, as compared to synthetic replicas of fractures, flows are highly interfering and not well represented by widely used relative permeability models such as X-curves (Huo et al., 2015).
- Gas flow does not displace water from the smaller fracture apertures or regions with larger apertures that are not connected to the inlet and outlet of the core.

- Multiphase flow shifts quickly from a liquid to a gas dominated system in fractures. The abrupt transition between the two flow regimes suggest that fractures are likely to be either gas or water conducting, depending on achieving a high enough gas saturation in the fracture.
- Water flows mainly through a connected set of the largest apertures. Other portions of the fracture are difficult to access for water and gas flow. This suggests that chemical reactions in the small apertures (which are likely to be prevalent in the fracture) will require diffusion of the solutes into the smaller apertures. This will slow or limit chemical reactivity in fractured rocks.

3. DYNAMICS OF OUTCROP-SCALE CO_2 FLOW IN A BASALT FRACTURE NETWORK

3.1 Objective

The project proposal originally called for geostatistical correlation structure of permeable intra-basalt flow features using fracture network models developed with terrestrial light detection and ranging. After our initial field season in fall 2015, we found that intra-flow features exist over much longer length scales than was anticipated. As a result, we focused permeability correlation efforts on regional scale data sets that are publicly available in the literature. Despite this pivot, we still had very high-resolution fracture network models developed with terrestrial LiDAR, and we embarked on an exploratory research effort to understand the multi-phase CO_2-brine flow dynamics (including CO_2 phase change) in basalt fractures. This study was made possible by recent advances in the TOUGH3 code, which parallelized the ECO2M module for simulating the non-isothermal CO_2-water-brine system, including phase change between sub- and super-critical phase CO_2. Results from this study reveal that CO_2 tends to accumulate at fracture intersections due to relative permeability effects. The implication of this result is that secondary alteration products may focus downgradient of the fracture intersection, thus sealing conductive flow paths.

3.2 Methods

This study utilizes multi-phase, multi-component numerical modeling to investigate the influence of fracture permeability on CO_2 infiltration and phase change(s) within a basalt entablature fracture network. The model scenario is designed to represent supercritical CO_2 entering a basalt entablature from below when the pressure-temperature conditions are near the phase change boundary for CO_2. As a result, this study provides first-order estimates of buoyancy-driven leakage potential as CO_2 density decreases during phase changes from supercritical fluid to subcritical liquid or gas. For this study, free CO_2 can be in any of three phases, which are (1) supercritical fluid, (2) subcritical liquid, and (3) subcritical gas; however, the supercritical phase fluid and subcritical gas are the predominant fluid phases in the modeling results. The model domain comprises a 5 m × 5 m fracture network developed using outcrop-scale data acquired by ground-based light-detection and ranging (LiDAR) (Sections 3.1 and 3.2). To account for the uncertainty associated with fracture permeability at depths of interest (> 750 m) for CO_2 sequestration, a synthetic fracture permeability distribution is produced on the basis of core-scale fracture aperture measurements from the literature (Section 3.3). This fracture permeability distribution is implemented for a Monte Carlo numerical model comprising fifty (50) equally probable, 2-D realizations of the same fracture network. In order to isolate the effects of permeability uncertainty, the fracture network geometry is identical for each realization; however, the spatial distribution of fracture permeability is randomly drawn from the synthetic permeability distribution. Three-phase relative permeability and capillary pressure effects are accounted for using generic characteristic curves (Section 3.4). Vertical CO_2 flow is simulated in each fracture network model (Section 3.5), and e-type estimates are computed for fluid pressure and CO_2 saturation over the complete ensemble of 50 equally probable fracture permeability distributions (Section 3.6). The bulk fluid and rock properties are listed in Table 3.1.

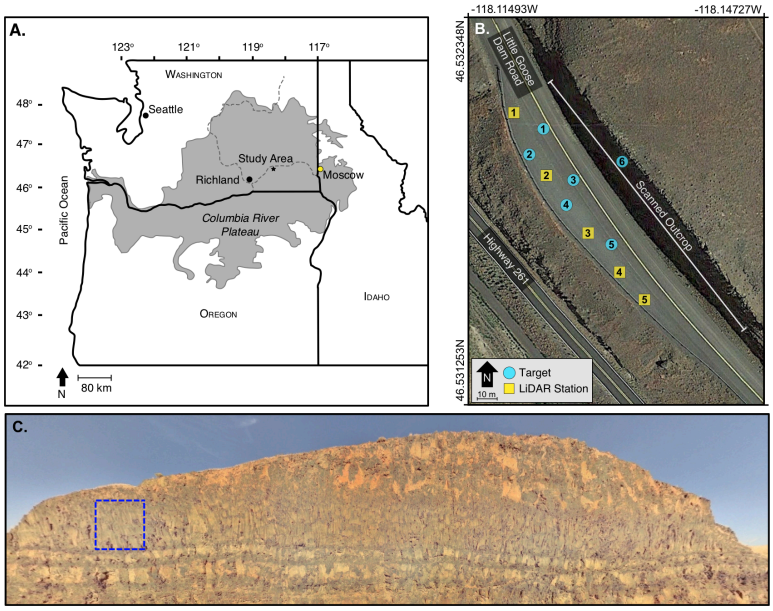

Figure 3.1: *(a) Areal extent of the Columbia River Basalt Group. (b) Study area map and LiDAR station locations at field site. Image from Google Earth™. (c) Image of study area outcrop with dashed blue box corresponding to the fracture network modeled for this study. The blue dashed box is 5 m × 5 m, and the image is not orthorectified.*

3.2.1 LiDAR Acquisition

Ground-based LiDAR scans were acquired from a basalt outcrop near Starbuck, Washington, in November 2015 (Figure 3.1B). The selected outcrop was approximately 100 m wide by 10 - 15 m tall (Figure 3.1C). Terrestrial LiDAR scans were acquired with a Z+F Imager 5010x, which is a phase-based laser scanner with a range of 187 m and range noise of ~0.4 mm at 25 m. LiDAR data were acquired at five scanning stations selected along the outcrop, and each scan was specified to overlap the previous scan by ~25% (Figure 3.1B). In order to facilitate accurate point cloud registration, six Z+F Profi targets were deployed in a staggered geometric configuration along the outcrop and each scan acquired a minimum of four targets. The LiDAR stations and target locations were geospatially referenced with a Trimble Geo7x hand held GPS configured for sub-centimeter resolution. The outcrop LiDAR scans were merged using Z+F Laser Control software with mean registration error of 1.7 mm, standard deviation of 1 mm, and maximum deviation of 5.6 mm. Following registration, errant data points (e.g., reflections from dust, insects, and occasional traffic) were filtered from the combined data set manually, and the post-processed outcrop point cloud data was exported in ASCII format.

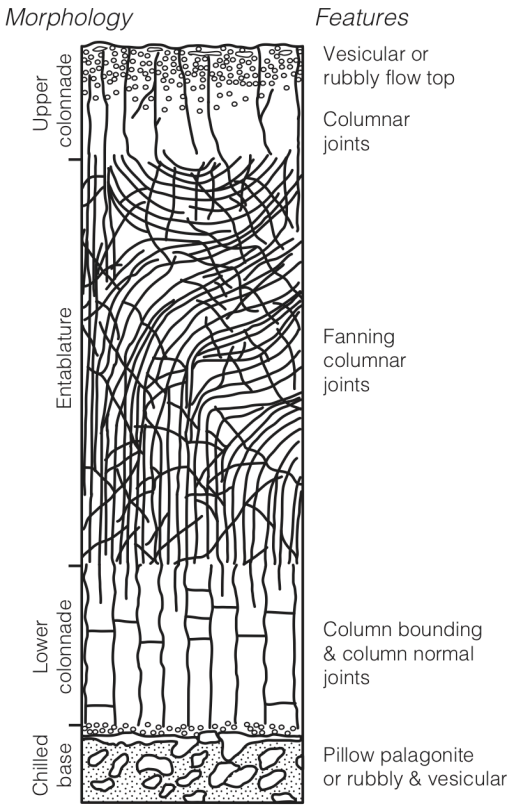

Figure 3.2: *Generalized schematic of CRBG flow morphology, modified after Mangan et al. (1986).*

3.2.2 Fracture Network Model

The fracture network developed for this study comprises a 5 m × 5 m sub-section of the post-processed point cloud (Figure 3.1C). This sub-section of the outcrop is located entirely within the entablature portion of the basalt flow. The entablature is of particular interest here because it has been proposed as the confining unit for CO_2 trapping on the basis of effective permeability values of $\sim 10^{-18}$ m^2 [*McGrail et al.*, 2009]. In order to extract the entablature fracture distribution from the subsampled region, the raw point cloud is processed using the surface roughness algorithm developed by *Pollyea and Fairley* [2011, 2012b]. In this method, the point cloud is discretized into a regular Cartesian grid and an orthogonal regression plane is fit to the points within each grid cell. The surface roughness of each grid cell is then calculated as the standard deviation of point-to-plane distances. This method returns surface roughness values on a ratio scale for each grid cell, and [*Pollyea and Fairley*, 2011] showed that 2-D fracture network models can be extracted by implementing a binary transform to normalized surface roughness data. The premise underlying this binary transform is that surface roughness is larger for grid cells intersecting fracture edges and/or prominences in the outcrop, and, as a result, this information is exploited to assign each grid cell to either “fracture” or “matrix” subdomains. Conse- quently, unique hydrogeological properties can be assigned within each subdomain for numerical flow modeling.

For this study, surface roughness is calculated within the 5 m × 5 m entablature subsection over a regular Cartesian grid discretized with 0.025 m (2.5 cm) resolution. This results in a 2-D model domain comprising 200 grid cells along each axis (40,000 total grid cells). After normalizing surface roughness to range between 0 and 1, the binary threshold delineating fracture and matrix grid cells is determined by trial-and-error to be the lowest value for which the resulting fracture network is visually realistic and at least two fractures are continuously connected through the domain (Figure 3.3).

3.2.3 Fracture and Matrix Permeability

Basalt matrix permeability is uniformly specified as 10^{-20} m^2 on the basis literature values ranging between 10^{-17} m^2 and 10^{-24} m^2 for basalt matrix permeability [*Bertels et al.*, 2001; *Nara et al.*, 2011; *Walker et al.*, 2013a,b]. In contrast, the fracture permeability for 0.025 m grid resolution is unknowable at depths of interest (> 750 m) for CO_2 sequestration; however, *Lamur et al.* [2017] report a core-scale

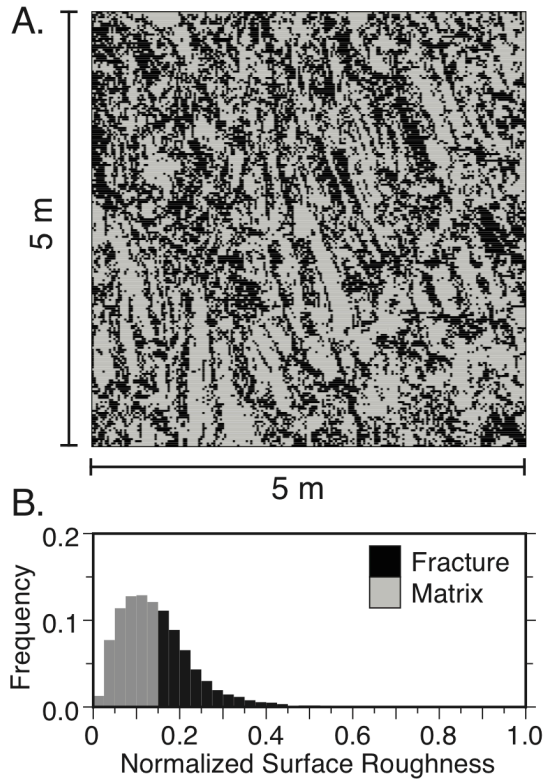

Figure 3.3: *(a) LiDAR-based 2-D fracture network map developed for this study. The fracture network is modeled with 0.025 m grid resolution from a 5 m × 5 m section of a Columbia River Basalt flow entablature (Figure 1c, blue dashed box). The fracture model comprises 40,000 grid cells. Matrix and fracture cells are denoted by gray and black shading, respectively. (b) Probability distribution of normalized surface roughness for the fracture network in Figure 2a. Shading denotes the proportion of the probability distribution assigned to matrix cells (gray) and fracture cells (black).*

basalt fracture permeability of ~ 10^{-15} m^2 at effective stresses up to 30 MPa. As a result, this study implements as a Monte Carlo numerical model comprising 50 individual simulations within the same fracture network. In this approach, the spatial distribution of fracture permeability in each model domain is randomly selected from a synthetic log-normal fracture permeability distribution.

The synthetic fracture permeability distribution is based on *Lindberg* [1989], which reports spatially uncorrelated and log-normally distributed fracture aperture (b) measurements from 3,194 CRBG joints. This aperture distribution is described by mean aperture of 2.66 × 10−4 m and standard deviation of 4.89 × 10^{-4} m. For this study, the fracture aperture distribution is converted to a fracture permeability (k_f) distribution on the basis of the parallel-plate cubic law ($k_f = b^2/12$) [*Witherspoon et al.*, 1980; *Ge*, 1997], which is assumed valid on the basis of the 0.025 m grid discretization. Application of the cubic law to the *Lindberg* [1989] aperture distribution results in a mean fracture permeability of 5.9 × 10^{-9} m^2 with corresponding standard deviation of 1.99 × 10^{-8} m^2. *Lindberg* [1989] also shows that CRBG fracture apertures are spatially uncorrelated, and, as a result, the fracture permeability distribution developed here is reproduced in 50 equally probable realizations of the same fracture map, while the spatial distribution within each realization is spatially uncorrelated.

Because the Lindberg (1989) distribution was measured from ex situ core samples, each simulated fracture permeability distribution is scaled to account for the effects of loading at depths of interest of CO_2 sequestration. In doing so, the simulated permeability value assigned to each grid cell is scaled by subtracting a mean fracture permeability that is assumed to be representative of in situ conditions. For this study, the in situ mean fracture permeability is estimated using the weighted geometric mean for the case when (1) effective (bulk) permeability is constrained by field-scale pumping tests and (2) matrix permeability is reasonably approximated by core-scale experimental data. In the context of effective medium theory, the general form of weighted geometric mean permeability is given by:

$$k_{eff} = exp\left(\frac{\sum \omega_i \ln k_i}{\sum \omega_i}\right)$$

where, k_{eff} is effective permeability, k_i is the permeability of subdomain i, and ω_i is a weighting function (Fairley, 2016; Rubin, 2003). For the bimodal fracture network model, equation (1) is expanded and rearranged to solve for mean fracture permeability:

$$k_f = exp\left(\frac{\ln k_{eff} - \omega_m \ln k_m}{\omega_f}\right)$$

where, subscripts f and m refer to the fracture and matrix subdomains, respectively. For this study, k_{eff} is specified as 10^{-18} m^2, which is a typical value for pumping tests in CRBG entablatures (McGrail et al., 2009; Wood & Fernandez, 1988); k_m is equal to the 10^{-20} m^2 (discussed above); and the weighting function is based on the probability distribution of each subdomain, so that ω_m and ω_f are 0.58 and 0.42, respectively, (Figure 3.3b). Equation (2) results in a mean in situ fracture permeability of 5.78 × 10^{-16} m^2, which is comparable to permeability tests in artificially induced basalt cores at effective stresses comparable to depths of interest for CO_2 storage (Lamur et al., 2017). The difference between this in situ mean k_f and the Lindberg (1989) mean permeability is subtracted from each simulated fracture

permeability in the ensemble of 50 equally probable realizations, which effectively translates the Lindberg (1989) distribution to depths of interest for CO_2 sequestration while maintaining the same degree of variability about the mean. The resulting fracture permeability distribution for one equally probable realization is illustrated in Figure 3.4a with the corresponding permeability histogram shown in in Figure 3.4b.

3.2.4 Three-Phase Constitutive Relations

For this modeling study, characteristic curves are used to simulate the effects of relative permeability and capillary pressure as functions of aqueous phase saturation. Relative permeability and capillary pressure for multiphase CO_2 and water systems have not yet been finalized (Gran et al., 2017). Consequently, the three-phase relative permeability model developed by Stone (1970) is implemented with constraints based on multiphase experiments between N_2 and water in a basalt fracture (Bertels et al., 2001). For this study, fitting relative permeability curves with data from multiphase N_2-water experiments is justified on the basis of Pini and Benson (2013), which shows very small differences in relative permeability characteristics between gN_2-water, gCO_2-water, and $scCO_2$-water fluid pairs at pressure and temperature conditions relevant for CCS (Pini & Benson, 2013). After fitting relative permeability curves, the resulting parameters are then used for the three-phase capillary pressure model developed by Parker et al. (1987). The relative permeability and capillary pressure models used for this study are shown graphically in Figure 3.5 with parameters in Table 3.1, and a detailed discussion of each model follows.

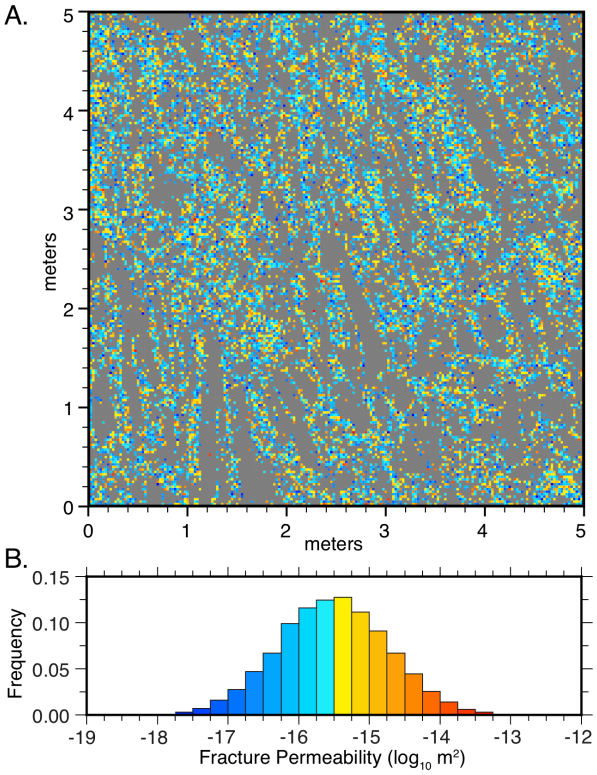

Figure 3.4: *(a) One equally probable fracture permeability distribution developed by scaling the Lindberg (1989) aperture distribution to depths of interest for CO_2 sequestration. Gray shading denotes matrix permeability (log_{10} k_m = -20) and color range denotes fracture permeability (log_{10} k_f). (b) Histogram of log_{10} k_f for the simulated permeability distribution in Figure4a. Color bars correspond with scale for log_{10} k_f in Figure 6a.*

Relative Permeability: To account for the effects of multiple fluid phases in each grid cell, the relative permeability model originally proposed by Stone (1970) is implemented for each fluid phase as:

$$k_{rg} = \left(\frac{S_g - S_{gr}}{1 - S_{ar}}\right)^n$$

$$k_{ra} = \left(\frac{S_a - S_{ar}}{1 - S_{ar}}\right)^n$$

$$k_{rl} = \left(\frac{1 - S_g - S_a - S_{lr}}{1 - S_g - S_{ar} - S_{lr}}\right)\left(\frac{1 - S_{ar} - S_{lr}}{1 - S_a - S_{lr}}\right)\left(\frac{(1 - S_g - S_{ar} - S_{lr})(1 - S_a)}{1 - S_{ar}}\right)^n$$

where, k_{rg}, k_{ra}, and k_{rl}, represent relative permeability for the nonwetting gaseous or supercritical (non-wetting) CO_2 phase, aqueous (wetting) phase, and nonwetting liquid CO_2 phase, respectively; S_{gr} and S_a are gaseous (or supercritical) and aqueous phase saturation, respectively; S_{gr}, S_{ar}, and S_{lr} are irreducible saturation parameters for the gaseous (or supercritical) CO_2 phase, aqueous phase, and nonwetting liquid CO_2 phase, respectively; and n is a phase interference parameter. The Stone (1970) relative permeability model is based on channel theory, which states that in any given channel, only one fluid is active. Furthermore, this relative permeability model assumes that the wetting phase tends to remain in small pore spaces, while the nonwetting phases preferentially occupy larger pores. Because of this phase separation, interactions of the liquid nonwetting phase with water and gas are considered separate events (Stone, 1970). To implement this model within the basalt fracture network, equations (3) and (4) are fit to data from two-phase (k_{rg} and k_{ra}, respectively) relative permeability experiments reported by Bertels et al. (2001) for water and nitrogen in a basalt fracture (Figure 3.5a and Table 3.1). At the time of this writing, relative permeability for the nonwetting liquid CO_2 phase (k_{rl}) has not been measured experimentally.

Capillary Pressure: Capillary pressure effects are modeled using the three-phase model reported by Parker et al. (1987). In this formulation, the capillary pressure across each fluid interface is calculated with the following set of equations:

$$P_{c,gl} = -\frac{\rho_a g}{\alpha_{gl}}\left(\bar{S}_l^{\frac{-1}{m}} - 1\right)^{\frac{1}{n}}$$

$$P_{c,ga} = -\frac{\rho_a g}{\alpha_{la}}\left(\bar{S}_a^{\frac{-1}{m}} - 1\right)^{\frac{1}{n}} - \frac{\rho_a g}{\alpha_{gl}}\left(\bar{S}_l^{\frac{-1}{m}} - 1\right)^{\frac{1}{n}}$$

$$P_{c,la} = P_{c,ga} - P_{c,gl}$$

where, $P_{c,gl}$ is capillary pressure across the interface between gaseous (or supercritical) and liquid phases, $P_{c,ga}$ is capillary pressure across the interface between gaseous (or supercritical) and aqueous phases, and $P_{c,la}$ is capillary pressure across the interface separating the nonwetting phase liquid and aqueous phases. In addition, g is acceleration due to gravity, ρ_a is aqueous phase density, m is the Van Genuchten (1980) phase interference parameter (m = 1 – 1/n), and α_{la} and α_{gl} are strength parameters for the liquid-aqueous and gaseous-liquid interfaces, respectively. In this formulation, capillary pressure calculated as a function of effective saturation ($\bar{S}$), where $\bar{S}_a$ is effective aqueous phase saturation ($\bar{S}_a = (S_a - S_{ar})/(1 - S_{ar})$) and ($\bar{S}_l$) is effective nonwetting phase liquid saturation ($\bar{S}_l = (S_g + S_l - S_{ar})/(1 - S_{ar})$). Equations (6–8) are parameterized using the α parameters presented by Parker et al. (1987) and irreducible wetting and nonwetting phase saturation values found by fitting the relative permeability model to Bertels et al. (2001) experimental data (Figure 3.5b and Table 3.1).

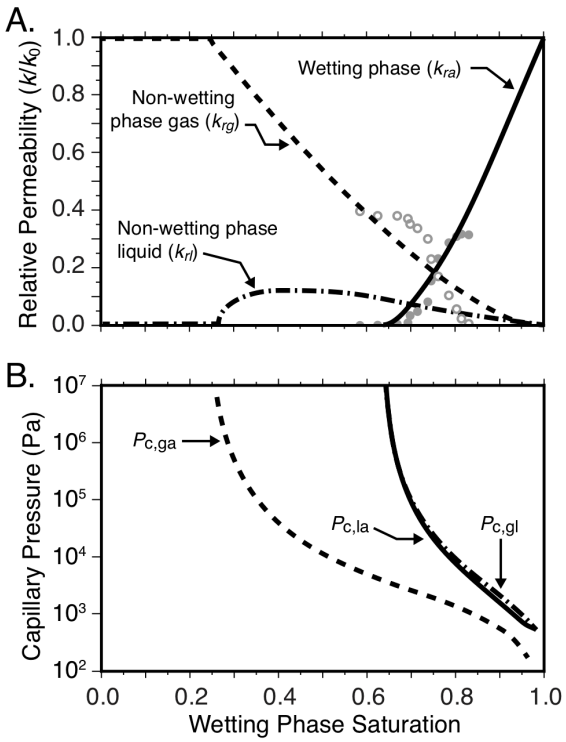

Figure 3.5: *(a) Labeled curves represent the three-phase relative permeability model of Stone (1970). Curves are fit to Bertels et al. (2001) experimental data for water-nitrogen relative permeability in a basalt fracture: solid and open circles are wetting and nonwetting phase relative permeability, respectively. (b) Three-phase capillary pressure model by Parker et al. (1987). See Notation section for a description of the symbols.*

3.2.5 Numerical CO_2 Flow Simulation

The numerical model simulates a scenario in which free-phase, supercritical CO_2 has accumulated below a basalt flow entablature at depths approaching CO_2 phase change boundary. The code selection for this study is TOUGH3 (Jung et al., 2016), which solves energy and mass conservation equations for nonisothermal, multiphase flows in porous geologic media. Here TOUGH3 is compiled with fluid property module ECO2M, which simulates mixtures of water, CO_2, and NaCl, as well as CO_2 phase change between liquid, gaseous, and supercritical state (Pruess, 2011). In this formulation, CO_2 phase partitioning in each grid cell is modeled on the basis of equilibrium thermodynamics for the temperature range 12° ≤ T ≤ 110°C and fluid pressure up to 60 MPa (Pruess, 2011).

Initial conditions are specified with a hydrostatic pressure gradient ranging from 7.35 to 7.39 MPa, which corresponds with a saturated depth of ~750 – 755 m. The initial temperature field is specified as 32°C, and thermal effects are accounted for in the simulations. These initial conditions are consistent with field conditions encountered at the Wallula Basalt Sequestration Pilot Project in southeast Washington State, USA (McGrail et al., 2009). Furthermore, this initial condition is designed such that free-phase supercritical CO_2 will encounter the critical point within the model domain, and thus undergo phase change to subcritical liquid or gas. Adiabatic pressure and temperature conditions are specified on the lateral model boundaries. Fluid is allowed to leave the model domain by specifying a Dirichlet condition at the upper boundary, and temperature is held constant at 32°C at the upper and lower boundaries. The

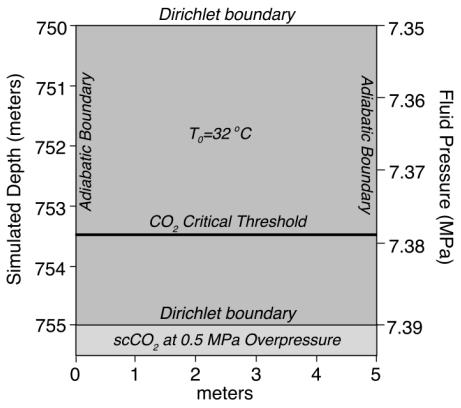

Figure 3.6: *Schematic illustration of the initial and boundary conditions implemented for each CO_2 model in this study.*

basal boundary simulates an accumulation of supercritical CO_2 below the basalt flow entablature by specifying a Dirichlet condition as fully saturated with CO_2 at 0.5 MPa overpressure and 32°C (Figure 3.6). Hydraulic and thermal properties are listed in Table 3.1.

In order to quantify the effects of fracture permeability uncertainty within the model domain, 50 individual CO2 flow models are performed within the synthetic fracture network. The decision to simulate 50 equally probable reservoirs represents a balance between computational efficiency and simulating sufficient data to capture a wide range of possible outcomes. For each numerical model, the fracture network geometry and initial and boundary conditions are identical; however, the permeability for each fracture cell is randomly drawn from the synthetic permeability distribution developed in section 3.3 (Figure 3.4b).

In closing this description of model development and specification, a brief mention about model limitations is warranted. Specifically, this modeling study does not account for geochemical processes responsible for basalt dissolution and carbonate precipitation, which are likely to affect fracture permeability. For example, Luhmann et al. (2017a, 2017b) show that CO_2-spiked water flowing in a basalt fracture results in minor permeability reduction due to mineral precipitation at low flow rates, while higher flow rates result in order-of-magnitude permeability enhancement due to rapid dissolution and transport. Similarly, Adeoye et al. (2017) indicate that the temporal evolution of fracture geometry under net dissolution is strongly influenced by mineral grain size. Although these processes will likely impose dynamically changing permeability in a natural fracture network, such scaling laws remain beyond the current state-of-the-art. Consequently, the numerical model developed here is relevant primarily in early time prior to widespread mineralization (<~ 10 years).

Table 3.1: *Model parameters*

Parameter	Symbol	Value	Units
Initial temperature	T_o	32	°C
Total dissolved solids	TDS	270	mg L^{-1}
Specific heat	c_p	840	J kg^{-1} $°C^{-1}$
Thermal conductivity	κ_T	2.11	W m^{-1} $°C^{-1}$
Basalt density	ρ_r	2,950	kg m^{-3}
Fracture porosity	ϕ_f	0.1	–
Matrix porosity	ϕ_m	0.01	–
Residual aqueous phase saturation	S_{ar}	0.63	–
Residual liquid phase saturation	S_{lr}	0.01	–
Residual gas phase saturation	S_{gr}	0.001	–
Van Genucten parameter (n = 1 – 1/m)	n	1.4	–
Capillary strength: gas-liquid interface	α_{gl}	10.8	–
Capillary strength: liquid-aqueous interface	α_{la}	6.0	–

3.2.6 Data Analysis (E-type Estimates)

The ensemble of 50 simulations is analyzed using e-type estimates, which yield the mean and variance of a simulated variable within each grid cell of the domain (Deutsch & Journel, 1998). For example, the mean value of simulated fluid pressure ($\bar{P}_{f(x,z)}$) in each grid cell of the Monte Carlo model is computed for the ensemble of 50 simulations as,

$$\bar{P}_{f(x,z)} = \frac{1}{50}\sum P_{f,i(x,z)}$$

where, $P_{f,i(x,z)}$ is the simulated fluid pressure at location (x,z) for simulation i. The corresponding measure of uncertainty around the mean at each grid cell is computed as the standard deviation ($\sigma_{Pf(x,z)}$),

$$\sigma_{Pf(x,z)} = \sqrt{\frac{1}{50}\sum\left(P_{f,i(x,z)} - \bar{P}_{f,(x,z)}\right)^2}$$

In addition to e-type estimates for fluid pressure, these equations are implemented for wetting and non-wetting phase saturations to assess variability in phase partitioning as a function of permeability uncertainty.

3.3 Results and Discussion

Each numerical model accounts for 10 years of simulation time with data output at 1, 5, and 10 years. The results of two individual simulations are illustrated in Figure 3.7, which shows total free-phase CO_2 saturation at 1, 5, and 10 years of simulation time. These individual simulations are labeled 39 and 46, and represent the minimum and maximum extent of CO_2 infiltration for the complete ensemble, i.e., these simulations are end-members of the model behavior after 10 years. The e-type estimates resulting from the complete ensemble at 1, 5, and 10 years are shown for total free-phase CO_2 saturation in Figure 3.8, and the corresponding e-type estimates for fluid pressure are shown in Figure 3.9. Phase partitioning between supercritical- and gas-phase CO_2 after 10 years of simulation is illustrated in Figure 3.10.

3.3.1 One Year

After 1 year of simulation, all free CO_2 remains in the supercritical phase for the end-member simulations, 39 and 46 (Figure 3.7). In both simulations, CO_2 rises ~1 m into the fracture network, and follows the same pathways with comparable saturation levels. The fluid pressure distribution in simulations 39 and 46 (not shown) propagates upward through the domain according to fracture network geometry. Consequently, fluid pressure decreases nonlinearly with elevated pressure occurring below blockages in the fracture pathways, and lower pressures along clear conduits.

E-type results for total CO_2 saturation and fluid pressure after 1 year are presented in Figures 3.8 and 9, respectively. The ensemble mean supercritical CO_2 saturation is comparable to the results for simulations 39 and 46, with mean CO_2 saturation ranging between 0.10 and 0.36 in the conductive fractures. The variability of this ensemble behavior is relatively low, as indicated by the corresponding standard deviation of □0.06 to 0.10, which is governed by variability in the permeability distribution. Nevertheless, the largest degree of CO_2 saturation variability occurs in conductive fractures, particularly where a single flow path diverges into two or more flow paths. The ensemble mean fluid pressure after 1 year of simulation indicates the pressure perturbation induced by infiltrating CO_2 is maximized in conductive fractures as pore space is drained (Figure 3.9a). Interestingly, fluid pressure variability is also maximized in the conductive fractures, where the maximum deviation is ~72 kPa (Figure 3.9c). This effect is most pronounced at the leading edge of the advancing CO_2, where aqueous phase relative permeability in basalt fractures decreases substantially at low CO_2 saturation levels (Bertels et al., 2001). This result agrees with Pollyea (2016), which shows that fluid pressure accumulation in basalt reservoirs is governed primarily by drainage of the aqueous phase. Similarly, the gradient in fluid pressure variability is highest below constrictions or blockages in the main fracture pathways, which can occur when a conductive fracture terminates or as a result of comparatively low fracture permeability. In contrast, fluid pressure variability within conductive fracture is smallest at locations where CO_2 initially enters the fracture network. The ensemble model results after 1 year indicate that CO_2 flow paths and fluid pressure distribution are controlled primarily by fracture network geometry, while variability in CO_2 saturation is governed by interactions between fracture permeability and network geometry.

3.3.2 Five Years

After 5 years, the end-member simulations 39 and 46 show little discernible difference in both CO_2 saturation (Figures 3.7b and 3.7e) and fluid pressure distribution (not shown). As with the 1-year end-member simulations, all free CO_2 remains in the supercritical phase as the fluid pressure diffusion from the lower boundary pushes the critical point of CO_2 to more shallow depths. E-type results for total CO_2 saturation and fluid pressure are shown in Figures 3.8b, 3.8e, 3.9b, and 3.9e, respectively. These results indicate the presence of three conductive fractures, within which supercritical CO_2 has migrated ~2 m from the basal boundary. Mean CO_2 saturation is ~0.2 in the conductive fractures, although substantially higher CO_2 saturation levels occur in disconnected fractures as CO_2 accumulates. In addition, elevated CO_2 saturation occurs at fracture junctions, where a single conductive fracture splits into two or more flow paths. This suggests that intersecting fractures may focus the effects of mineralization, as elevated free CO_2 maintains an equilibrium supply of hydrogen and bicarbonate ion to drive both basalt dissolution and carbonate precipitation (Pollyea & Rimstidt, 2017). Interestingly, the standard deviation of CO_2 saturation is generally highest along continuous sections of the fracture network, suggesting that fracture permeabil-

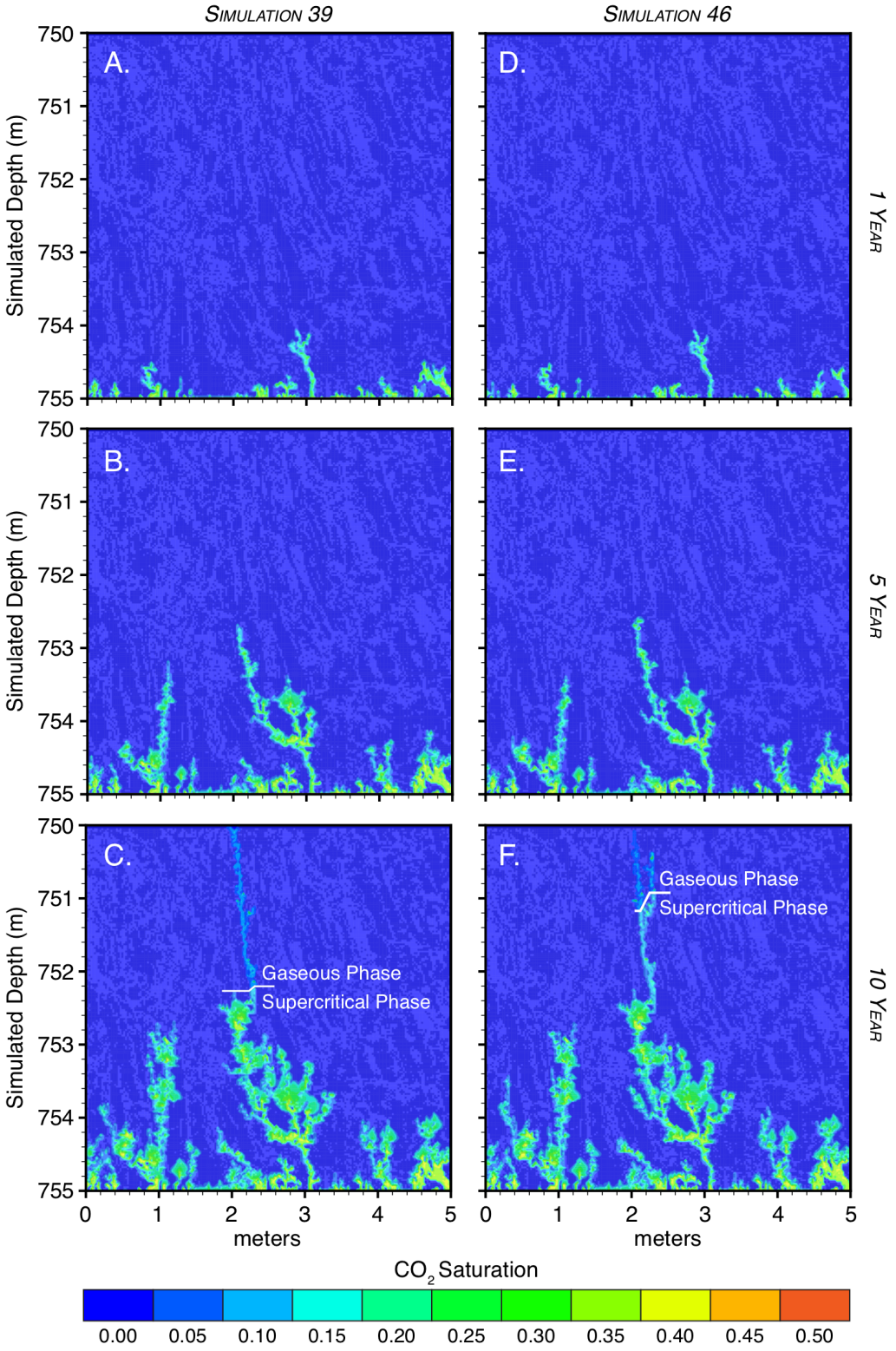

Figure 3.7: *Temporal evolution of total CO2 saturation for end-member simulations: simulation 39 at (a) 1, (b) 5, and (c) 10 years; simulation 46 at (d) 1, (e) 5, and (f) 10 years.*

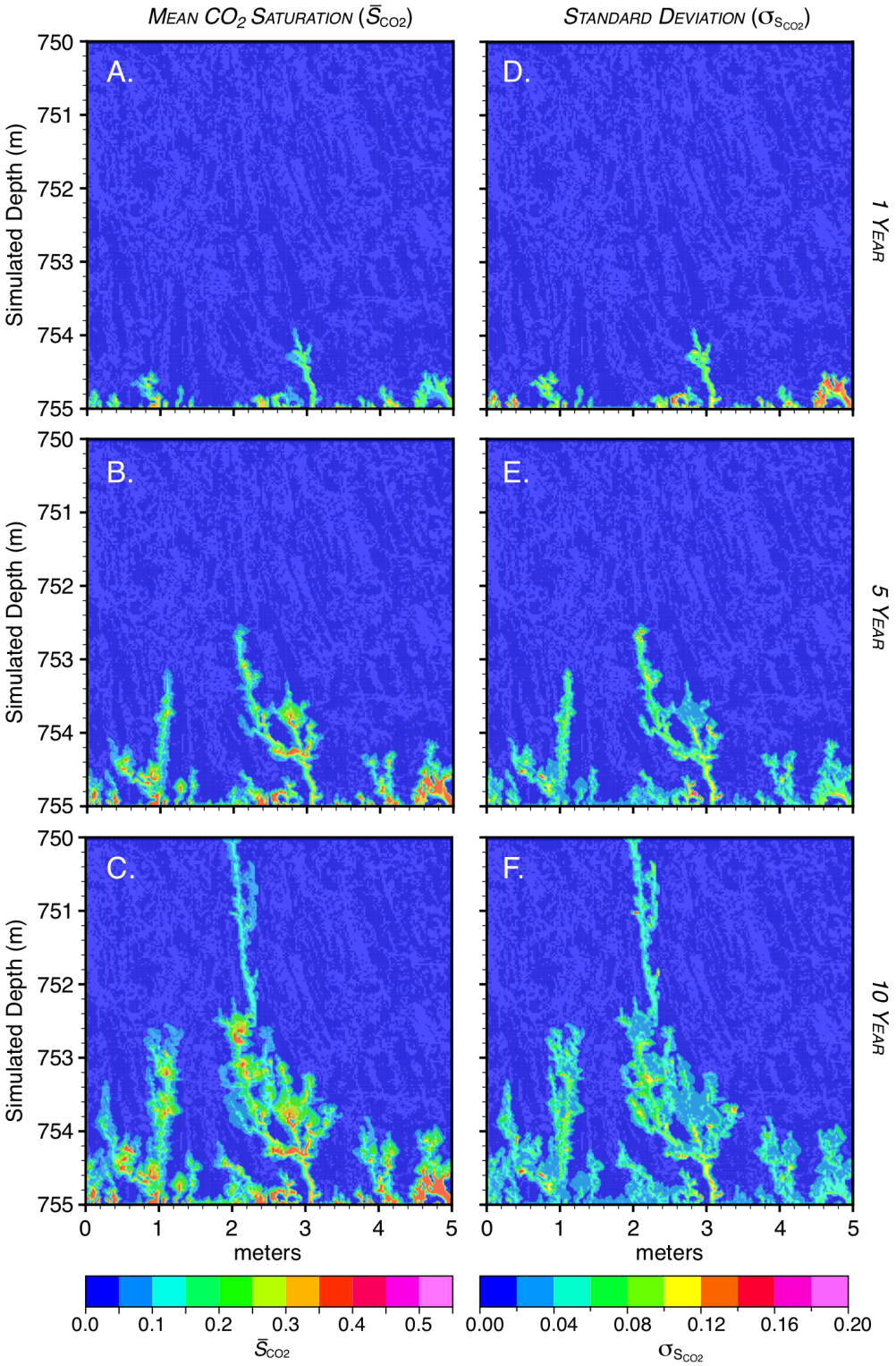

Figure 3.8: *Ensemble results (e-type) of total CO_2 saturation for Monte Carlo model (N=50 simulations). Results are calculated with equations in Section 3.2.6 for mean (total) CO_2 saturation at (a) 1, (b) 5, and (c) 10 years, and (d–f) corresponding standard deviation for each mean.*

ity strongly influences CO_2 saturation within the conductive portion of the fracture network (Figure 3.8e).

The mean fluid pressure distribution after 5 years of simulation is generally similar to the 1-year results (Figure 3.9b); however, the corresponding variability is substantially lower across most of the domain (Figure 3.9e). This suggests that flow paths for CO_2 imbibition and aqueous phase drainage stabilize within the fracture network. Nevertheless, a sharp discontinuity in mean fluid pressure emerges at the horizontal position ~2 m from the origin and 752.6 m simulated depth (Figure 3.9b). This discontinuity is collocated with a small region of elevated uncertainty, which is a constriction in the conductive fracture, where the flow paths bends to the right and permeability within a single grid cell is the dominant control on flow through the network. The region above this constriction is marked by a near-vertical channel of moderate fluid pressure uncertainty. Although this channel comprises no CO_2 at the 5-year time step, the fluid pressure variability suggests that drainage is underway, thus foreshadowing the development of a primary flow path within the fracture network. Although similar behavior is seen in the fluid pressure distribution at horizontal positions less than 2 m from the origin, the effects are much more diffuse as the conductive fractures in this region terminate into the basalt matrix.

3.3.3 Ten Years

After 10 years, the end-member simulations 39 and 46 comprise three-phase CO_2 conditions with supercritical fluid and subcritical gas as the predominant phases (Figures 3.7c and 3.7f). The notable difference between the end-member simulations is illustrated by (1) the depth of phase change and (2) the flow path taken by gas phase CO_2 at shallow depths in the domain. In simulation 39, phase change occurs at ~752.2 m simulated depth; however, the depth of phase change in simulation 46 occurs over a 0.2 m interval between 751.0 and 751.2 m simulated depth, depending on the conductive fracture. This difference in phase partitioning is caused by fluid pressure variability, which in these simulations is solely a function of fracture permeability.

The ensemble e-type results for total CO_2 saturation at 10 years are presented in Figures 3.8c and 8f. These results show that CO_2 flow within the fracture network converges on a single path, while significant CO_2 saturation levels accumulate within less conductive fractures. This behavior is consistent with numerous studies that show flow path convergence in fracture-controlled, multiphase systems (Carneiro, 2009; Fairley et al., 2004; Glass et al., 2003; LaViolette et al., 2003; Wood et al., 2004; Zhou et al., 2006). In Pollyea and Fairley (2012a), the authors suggest that relative permeability effects may favor flow path convergence in strongly heterogeneous, multiphase fluid systems. In particular, these authors suggest a feedback mechanism in which resistance to flow along a given flow path decreases as CO_2 saturation increases, thus increasing CO_2 relative permeability and allowing further saturation gains along the flow path. In the context of CO_2 sequestration in basalt reservoirs, the nature of CO_2 flow paths to converge suggests that physical trapping may be significantly enhanced as carbonate minerals precipitate in the primary flow path.

In addition to flow path convergence, mean CO_2 saturation levels remain higher at locations within the fracture network where a single flow path branches and where conductive fractures terminate into the basalt matrix. This behavior is consistent with the early time results, and suggests that relative permeability effects encourage CO_2 accumulation at fracture intersections because CO_2 saturation levels are lower in the diverging fractures, thus inhibiting mobility through the intersection. Although this relative permeability effect at fracture intersections has not been shown experimentally, Glass et al. (2003) found that water tends to accumulate at fracture intersections during imbibition of an unsaturated fracture network. However, these authors proposed that water must overcome capillary barrier effects at a fracture intersection before advancing.

The corresponding standard deviation of total CO_2 saturation is also consistent with early time results in that maximum variability occurs in relatively straight flow paths (Figure 3.8f). This result arises because unsaturated flow in fracture networks is dependent on the properties of the entire path (Doughty, 2000). For each simulation in the Monte Carlo model, CO_2 follows the same fracture; however, the CO_2 saturation at any point is dependent on the permeability distribution along the entire fracture, including the permeability ahead of the advancing CO_2. This effect was shown by Kwicklis and Healy (1993), which used numerical methods to show that fluid flux varies spatially within a fracture network with variable aperture, even under saturated steady flow. For multiphase fluid systems, path-dependent flow is likely to be even more pronounced as relative permeability and capillary pressure effects introduce strongly nonlinear feedbacks within the fracture network.

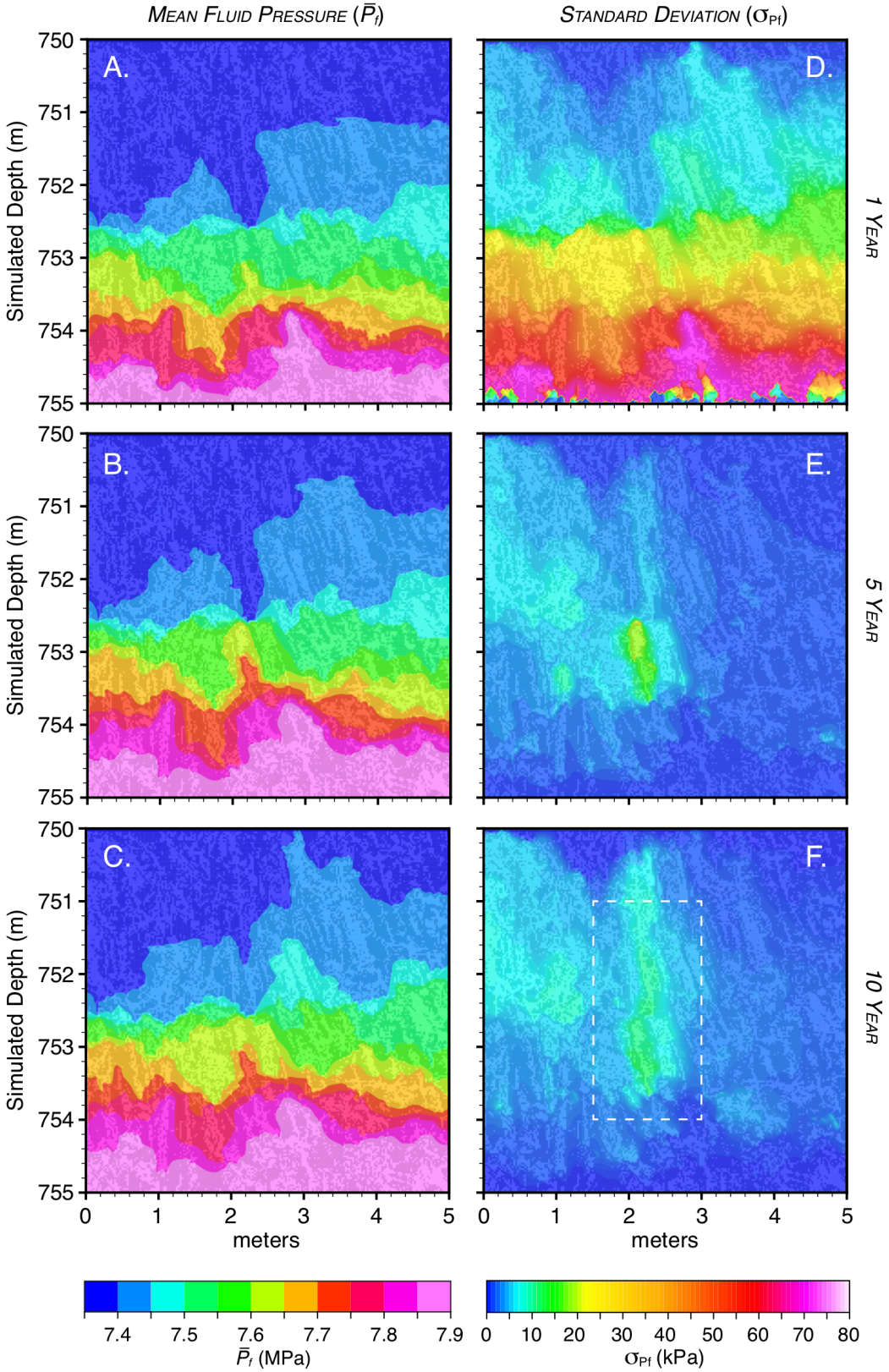

Figure 3.9: *Ensemble results (e-type) of fluid pressure for the Monte Carlo model (N550 simulations). Results are calculated with equations (9) and (10). Mean fluid pressure at (a) 1, (b) 5, and (c) 10 years, respectively, and (d–f) the corresponding standard deviation for each mean. Dashed box in panel F is presented in Figure 3.11.*

In order to evaluate the effects of fracture permeability uncertainty on phase partitioning, individual e-type results for supercritical and gas phase CO_2 are presented in Figure 3.10. At simulated depths less than ~750.8 m, the mean and standard deviation of supercritical phase CO_2 saturation are nil, which indicates that all CO_2 above 750.8 m is in the gas phase (Figures 3.10a and 3.10c). Similarly, for simulated depths greater than ~752.4 m, the mean and standard deviation of gas phase CO_2 saturation are zero indicating that all free CO_2 below this depth is in the supercritical phase (Figures 3.10b and 3.10d). Consequently, the model scenario comprises a 1.6 m overlap in which phase partitioning is governed solely by the spatial distribution of fracture permeability. In this model scenario, temperature variations are orders of magnitude lower than pressure variations, and, as a result, the window of permeability-controlled phase partitioning is governed primarily by fluid pressure.

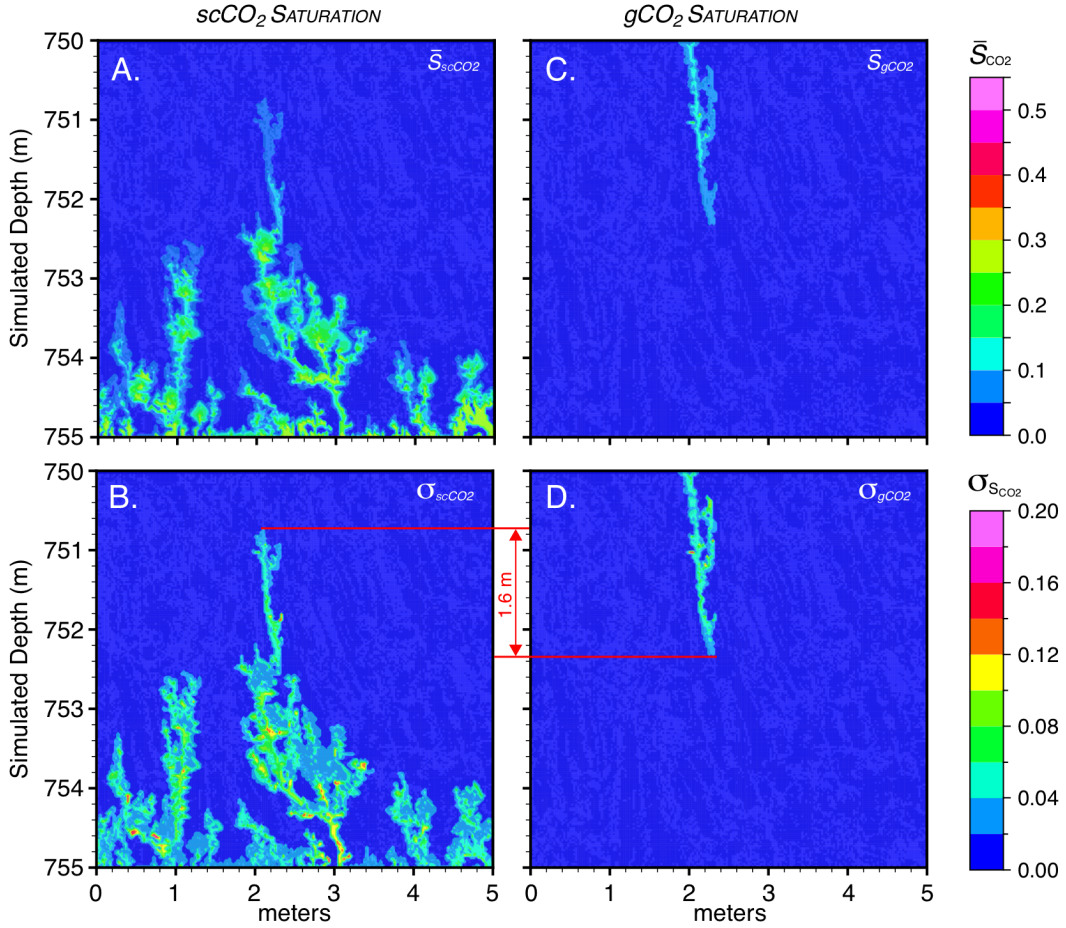

Figure 3.10: *Ensemble results (e-type) of (a, b) supercritical phase CO_2 and (c, d) subcritical gas phase CO_2 for the Monte Carlo model (N=50 simulations) after 10 years of simulation. The depth-interval for which fracture permeability governs phase partitioning is shown as red lines in Figures 3.10c and 3.10d.*

E-type results for fluid pressure after 10 years of simulation are shown in Figures 3.9c and 3.9f. The mean fluid pressure distribution is consistent with the 1- and 5-year results, except that the fluid pressure discontinuity is less pronounced at the horizontal position ~2 m from the origin and 752.6 m depth. Similarly, the standard deviation of fluid pressure at this location is substantially lower due to pressure redistribution along the continuous flow path that develops through the fracture network. This flow path is demarcated by a near-vertical zone of pressure variability that is attributable to fracture permeability variability (Figure 3.9f). The effects of uncertainty in permeability within the conductive fracture are presented with greater detail in Figure 3.11. Within the conductive fracture, the effects of permeability uncertainty are most pronounced between 753.0 and 753.5 m depth, where CO_2 is supercritical and fracture connectivity is restricted to a single grid cell. Within the overlapping phase-change interval (750.8–752.4 m), fluid pressure variability is comparatively lower (~10 kPa). The

combined e-type estimates for fluid pressure, gas-phase CO_2, and supercritical phase CO_2 suggest that as buoyant supercritical CO_2 approaches the critical point, phase partitioning is highly sensitive to small changes in fluid pressure. These effects are complicated by volumetric expansion locally increasing fluid pressure, as well as the development of the three-phase zone that locally alters CO_2 mobility due to highly nonlinear, three-phase relative permeability and capillary pressure effects (Pruess, 2005). Since fluid pressure variability in the Monte Carlo model is solely a function of permeability distribution, these results suggest that CO_2 phase partitioning is strongly controlled by the fracture permeability distribution, which for this model occurs within a 1.6 m depth interval (thickness).

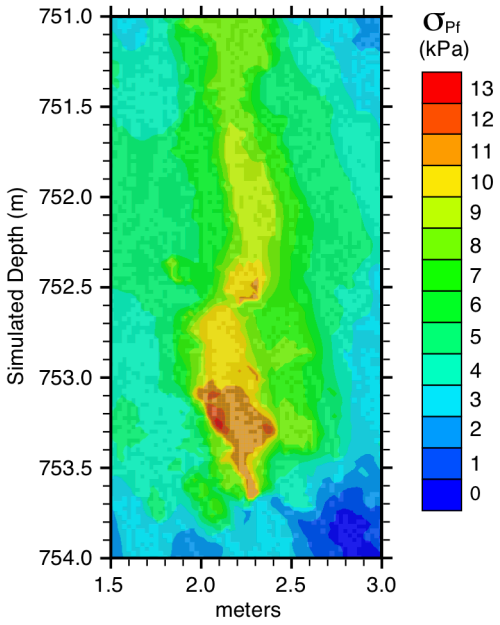

Figure 3.11: *Detail subsection of Figure 3.9f with rescaled contour interval illustrating standard deviation of fluid pressure for the Monte Carlo model (N=50) after 10 years of simulation.*

3.4 Summary

Successful field experiments in Washington State, USA, and Iceland yield compelling evidence that basalt reservoirs may be attractive targets for carbon capture and sequestration (Matter et al., 2016; McGrail et al., 2017). Nevertheless, industrial-scale implementation of this technology is hampered by still incomplete knowledge of multiphase flow characteristics in highly heterogeneous basalt fracture networks. This study is designed to gain insights into the behavior of CO_2 within the fracture network of an outcrop-scale flood basalt entablature when (1) the spatial distribution of fracture permeability is a priori unknown and (2) buoyant CO_2 undergoes phase change from supercritical fluid to subcritical liquid or gas. The primary results of this study are summarized below.

1. In early time (~1 year), CO_2 flow paths and fluid pressure are controlled primarily by fracture network geometry, while variability in CO_2 saturation is governed by interactions between fracture permeability and network geometry.
2. After 5 years of simulation, the ensemble (e-type) CO_2 saturation results show that CO_2 accumulates at fracture intersections, which suggests that mineralization may focus at these locations.
3. Ensemble calculations for subcritical and supercritical CO_2 after 10 years of simulation show that variations in fracture permeability result in a ~1.6 m depth interval within which phase change occurs. This suggests that flood basalt entablature zones may exhibit favorable physical trapping characteristics for isolating CO_2 over time scales required for widespread mineralization.
4. For the model scenario, CO_2 flow tends to converge on a single flow path. This is consistent with previous investigations documenting similar behavior as water infiltrates an unsaturated fracture network (Fairley et al., 2004; Glass et al., 2003; LaViolette et al., 2003). In the context of CCS in flood basalt, the combination of CO_2 accumulation at fracture intersections and flow path convergence suggests that physical trapping within the low-permeability entablature zone may be significantly enhanced as carbonate minerals precipitate at fracture intersections and decrease overall fracture network connectivity.

In conclusion, these results suggest a theoretical possibility that the basalt-CO_2-water system may be self- sealing; however, significantly more research is needed to assess the likelihood of such an outcome in real world settings. Specifically, additional research is needed to more fully understand the nature of reactive permeability alteration, stress-dependent reservoir properties, and multiphase fluid properties in basalt fracture networks, and to incorporate these processes into reactive transport simulation codes.

4. REGIONAL-SCALE PERMEABILITY ARCHITECTURE OF THE COLUMBIA RIVER BASALT GROUP

4.1 Objective

The spatial distribution of permeability is a first-order uncertainty in the context of modeling CO_2 injections in flood basalt reservoirs. As a result, this project implements ensemble simulation methods to model CO_2 injections into equally probable synthetic reservoirs, and doing so requires a spatial correlation model of permeability within the Columbia River Basalt Group (CRBG). We develop a new permeability database for the Columbia River Basalt Group (CRBG), USA, (Fig. 4.1) and calculate the semivariogram and permeability-depth profile. In doing so, we discovered that (i) permeability correlation is direction-dependent, (ii) the direction of long-range permeability correlation aligns with structural features underlying the CRBG, and (iii) CRBG permeability appears to *increase* at depths below ~1,000 m. We then interpret our findings to assess applicability of permeability-depth (*k*-*z*) scaling in large igneous provinces. Our analysis indicates that bulk permeability within the CRBG does not follow the expected depth-dependent trend between 950 and 1,450 m, and we hypothesize that this deviation from classical *k*-*z* scaling laws results from rapid emplacement, subsequent lithospheric subsidence, and the development of bending moment stresses.

4.2 Methods

4.2.1 Data Sources

We compiled a database of spatially referenced permeability values from previously published well data within the Columbia River Basalt Group (Reidel et al., 2002; Spane, 2013; Burns et al., 2015). The database consists of 598 individual wells with hydrologic data comprising, hydraulic conductivity (*K*), transmissivity (*T*), or permeability (*k*), as well as geographic location, center interval depth, and estimated temperature, viscosity (μ), and water density (ρ). In addition, numerous wells include multiple test intervals, and, as a result, the complete database comprises 874 records. It should be noted that the center interval depth represents the depth utilized by *Burns et al.* (2015) and represents the middle of the testing interval reported from Reidel et al. (2002) and Spane (2013). For this study, *K* is converted to permeability using the relation $k = (K\mu)/(\rho g)$, and *T* is converted to permeability as $k = (T\mu)/(\rho g b)$, where μ, ρ, g, and *b* are water viscosity, water density, gravitational acceleration, and open well interval, respectively. In Burns et al. (2015), the authors adopt a convention in which *b* is either the open well interval or 30 m (whichever is greater). This convention is based on the idea that a typical CRBG basalt flow thickness is ~30 m. The present study adopts this convention in order to maintain consistency with the substantial CRBG permeability database already reported by Burns et al. (2015). Burns et al. (2015) utilizes hydrologic data from both Kahle et al. (2011) and Spane (2013), to keep consistency and remove any redundant entries two measures were taken. First, only the data compiled by Burns et al. (2015) from Kahle et al. (2011) are used. The data from Spane (2013) is used as a test to ensure consistencies, by testing the conversion of hydrologic data to bulk permeability in this study to the converted bulk permeabilities in Burns et al. (2015). To test the consistency between the Burns et al. (2015) and this study, the percent error was calculated using %

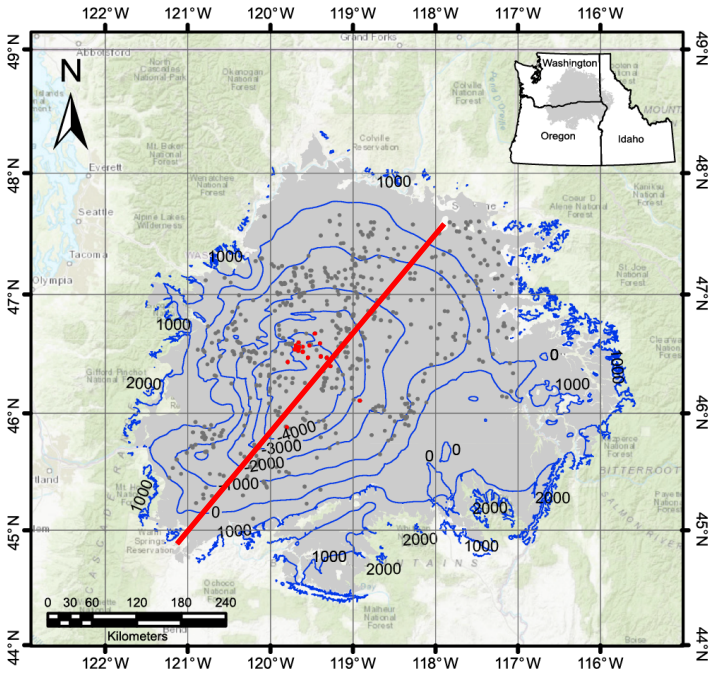

Figure 4.1: *Study area map of the Columbia River Plateau, USA, with Columbia River Basalt Group (CRBG) shown in gray shading. Dark gray circles denote well locations with hydrologic data used in this study, and red circles denote wells greater than 950 m. Blue contour lines show the bedrock elevation in meters above mean sea level (m amsl) (Burns et al., 2011). Thick red line is N40°E, and direction of maximum horizontal spatial correlation for CRBG permeability. Base map from Esri (https://www.esri.com).*

*error = ((experimental – theoretical)/theoretical) *100,* where the experimental value is log bulk permeability from this study and theoretical value is log bulk permeability from Burns et al. (2015). This comparison between 42 bulk permeability values results in an average difference of 0.7% between this study and Burns et al. (2015), which gives confidence to the consistency of the tabulated data. Second, to check for redundancy within the database a shell script was used to filter the entire database on unique combinations of Easting, Northing, and center interval depth, this results in 874 unique spatial locations (*x*, *y*, and *z*) of permeability values. In order to account for thermal effects on water properties, the temperature for each open well interval where temperature is not reported, it is estimated by using the regional heat flux of ~65 mW/m^2 (Pollack et al., 1993). In addition, all geospatial locations are converted to Universal Transverse Mercator coordinates using the Geospatial Data Abstraction Library.

4.2.2 Semivariogram Analysis

The spatial variability of CRBG scalar permeability as a function of distance is calculated using the experimental semivariogram, which is a two-point measure of spatial autocorrelation. The experimental semivariogram is defined mathematically as,

$$\gamma(h) = \frac{1}{2N(h)} \sum_{i=1}^{N(h)} (z_i - z_{i+h})^2,$$

where, $N(h)$ is the total number of data pairs separated by a spatial lag distance (h), and z_i and z_{i+h} are the head and tail values of each data pair, respectively (Deutsch and Journel, 1998). Owing to the large range of permeabilities within the database, a logarithmic (base 10) transform is applied to the permeability data, which results in a lognormal permeability distribution. In order to search for horizontal anisotropy in the spatial distribution of bulk permeability values, a 2-D semivariogram map is developed using Geostatistical Software Library™ (GSLIB; Deutsch and Journel, 1998). A semivariogram map is way to quantify γ(h) in all horizontal directions and lag distances (Fig. 4.2). This allows for the directions of minimum and maximum spatial continuity to be determined in the horizontal plane. The directions of minimum and maximum spatial continuity are then used to calculate directional semivariograms, which requires narrowing the search window for data pairs. In order to narrow the search window, the experimental semivariogram values are calculated between pairs of points along an azimuth defined by the directions of maximum and minimum continuity, 40° and 130° respectively. To narrow the search window in these directions additional parameters must be defined. The azimuth tolerance defines the maximum and minimum search azimuth. For example, the direction of maximum continuity is 40° and the azimuth tolerance chosen for this study is 45°, this means the full search window for data pairs is from 355° to 85°. Additionally, an azimuth bandwidth must be defined, which restricts the amount of deviation from the azimuth is allowed while searching for data pairs. For this study an azimuth bandwidth of 25 km is chosen. The azimuth tolerance and bandwidth control the swath of data for which the calculations are done, by increasing or decreasing these values effects the number of data points involved in each calculation for a given lag distance. Defining an azimuth, azimuth tolerance, and azimuth bandwidth changes the search pattern from a circular (isotropic) pattern to an angular band. Using an angular band to calculate the two horizontal semivariograms orthogonal to one another is a way to quantify both the spatial correlation of permeability values in those directions and also the spatial anisotropy of permeability values within the CRBG. For horizontal semivariogram calculations, multiple permeability values within a single well present a unique challenge because collocated data are known to increase the uncertainty at short lag distances. To address this challenge, the arithmetic mean of permeability is taken within wells that have multiple testing intervals. This method has shown to be a

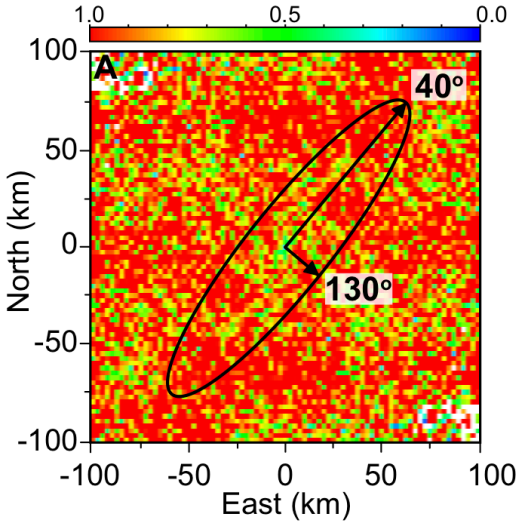

Figure 4.2: *Two-dimensional semivariogram map of CRBG permeability over a 2.5 km grid. Axes refer to North and East directions in kilometers, which are representative of lag distance γ(h), as shown in Equation 1. Black arrows denote directions of maximum and minimum horizontal spatial correlation within the ellipse scaled to reflect the anisotropic 2-D correlation structure.*

suitable method for aggregating collocated data (Desbarats and Bachu, 1994). Once the experimental semivariograms are calculated, each semivariogram can be fit with a linear combination of a priori permissible functions, e.g., spherical, exponential, Gaussian, hole effect, or power law (Deutsch and Journel, 1998). The models that are fit to the semivariogram can be fully characterized by: (1) the nugget effect, which represents spatial variability at a lower resolution than the defined lag distance; (2) the sill, represents the variance of the dataset and once the semivariogram oscillates around the sill, the data is considered to be spatially random; and (3) the range, which is the distance at which spatial correlation can be inferred. In order to compare the semivariogram calculations for different directions, each experimental semivariogram is normalized over its respective variance so that the sill (variance) in each direction is one. By fitting each experimental semivariogram with a linear combination of permissible functions, a 3-D model of spatial autocorrelation for CRBG permeability is constructed as shown by Figure 4.3.

4.2.3 Permeability variability with depth (*k*-*z* scaling)

The permeability-depth (*k*-*z*) profile is calculated on the basis of a 200 m moving average using the methods proposed by Burns et al. (2015), and 1σ dispersion about the mean is calculated to quantify uncertainty in the *k*-*z* profile (Fig. 4.4).

4.3 Results

The permeability-depth calculations (Fig. 4.4) show that average bulk (scalar) CRBG permeability (1) exhibits no apparent depth dependence between 0 and 500 m; (2) systematically decays by four orders of magnitude between ~500 and 950 m depth; and (3) increases by 1.5 orders of magnitude between 950 and 1,450 m depth. The *k*-z results between 0 and 950 m are generally consistent with Burns et al. (2015); however, their study suggests that the CRBG *k*-z profile likely exhibits power law decay at depths beyond 950 m. In contrast, our results indicate that permeability increases by 1.5 orders of magnitude between 950 and 1,450 m depth. To support the results presented in Figure 4.4, we observe that 1σ dispersion about the moving average systematically decreases with increasing depth beyond 950 m despite fewer data within the 950–1,450 m depth interval. Moreover, there are 21 permeability data above the 1σ threshold, while only 9 data points are below. The increasing *k*-z trend beyond 950 m is further supported by a single CRBG permeability measurement of 5.7×10^{-15} m^2 at 1,828 m depth, which is not included in the moving average calculations because the depth is more than 200 m beyond the deepest datum shown in Figure 4.4. These results suggest that the trend of increasing permeability within the 950–1,450 m depth interval may be robust on the basis of currently available data.

Semivariogram analysis reveals that: (1) CRBG permeability is spatially correlated with a 5:1 anisotropy ratio in the horizontal direction, (2) the directions of maximum and minimum spatial correlation are oriented N40°E and N130°E, respectively (Fig. 4.2), and (3) the vertical semivariogram is characterized by a power law model comprising a sill of 0.55 and exponent (ω) of 0.35 (Fig. 4.3). In comparing the direction of maximum horizontal spatial correlation with the depth to bedrock below the CRBG (Burns et. al., 2011), we find that the direction of maximum horizontal spatial correlation (N40°E) for CRBG permeability aligns remarkably well with the longitudinal axis of the bedrock underlying the Columbia River Plateau, which is oriented ~N42°E (Fig. 4.1).

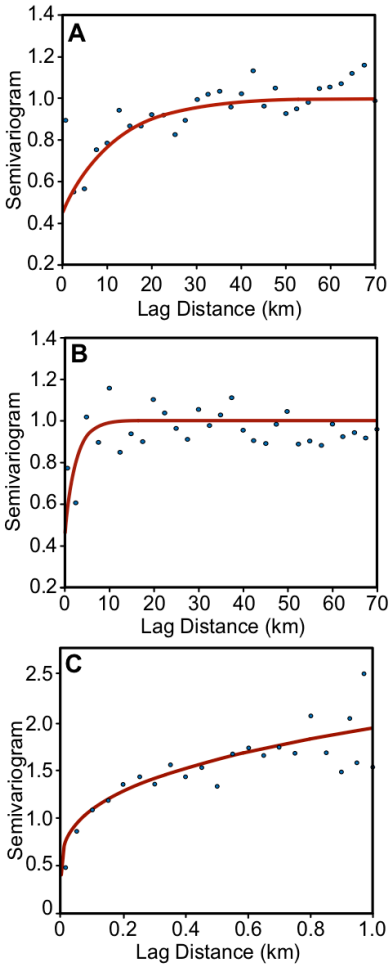

Figure 4.3: *Spatial correlation model for Columbia River Basalt Group (CRBG, western USA) permeability, with horizontal experimental semivariograms for maximum (N40°E) (A) and minimum (N130°E) (B) spatial correlation directions. Each semivariogram is normalized over the variance. Circles denote experimental semivariogram (text Equation 1), and red line denotes model semivariogram with parameters shown in Table 4.1.*

4.4 Discussion

Our results indicate that CRBG bulk permeability exhibits (1) an unexpected increasing trend within the 950–1,450 m depth interval (Fig. 4.4) and (2) the direction of maximum spatial correlation is in alignment with the longitudinal axis of the underlying bedrock depression (Fig. 4.1). We interpret these results in the context of CRBG emplacement. The CRBG is a continental large igneous province in the northwest United States (Fig. 4.1). The CRBG comprises a layered assemblage of ~300 Miocene-age flood basalts with an areal extent of 200,000 km^2, aggregate thickness of 1–5 km, and total estimated volume of 224,000 km^3 (Reidel et al., 2002). Long and Wood (1986) show that during emplacement CRBG flows initially followed an east-to-west paleoslope, and then ponded within a north-south trending paleobasin that subsequently experienced local clockwise rotation (Hooper and Conrey, 1989). This is evident in bedrock contours underlying the CRBG, which show that: (1) the CRBG occupies a bedrock depression trending ~N42°E (Fig. 4.1), and (2) the thickness of individual CRBG members generally increases near the center of the bedrock depression (Burns et al., 2011).

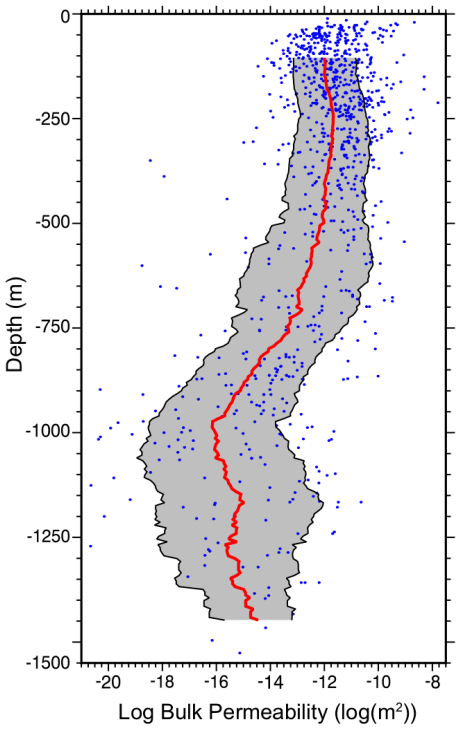

Figure 4.4: *The permeability-depth (k-z) profile is calculated on the basis of a 200 m moving average using the methods proposed by Burns et al. (2015). Gray shading denotes and 1σ dispersion about the mean.*

At the time of initial CRBG eruptions (~17 Mya), the Columbia River Plateau was undergoing uplift, and the Grande Ronde and Imnaha eruptions (17 - 15.5 Mya) produced ~94% of the total CRBG volume over a period of 1.5 million years (Reidel et al., 1989). This volume and emplacement rate rapidly loaded the underlying crust as high-density mafic rocks accumulated over comparatively lower density felsic rocks, which caused a down warp in the continental crust underlying the Columbia River Plateau (Hales et al., 2005). Since this time, the Columbia River Plateau has been undergoing subsidence at a decreasing rate from 0.7 - 1 cm yr^{-1} (15.6 Mya) to the current rate of ~0.003 cm yr^{-1} (Reidel et al., 1989).

The lithospheric response to loading is well documented in the case of continental ice sheet advance/retreat (e.g., Walcott, 1970a) and volcanism (Clague and Dalrymple, 1987; Jackson and Wright, 1970; Moore, 1970). In the context of glacial advance and volcano construction, rapid lithostatic loading in both oceanic and continental crust induces rapid evolution in the principal stresses (e.g., Walcott, 1970a; Bianco et al., 2005; Hieronymus and Bercovici, 1999). During continental glaciation, the lithostatic response to rapid loading has been linked to bending moment stresses at the base of an ice sheet that induce tensile fractures and increase the permeability of basal ice (Boulton and Caban, 1995). Although there are fewer studies of the lithostatic response to continental large igneous provinces (LIPs), Walcott (1970b) showed that flexural rigidity of continental lithosphere decreases by two-orders of magnitude for long-term loading conditions (>~10^4 yr), and that this flexural response is controlled by both elastic and viscous processes. In the presence of loading-induced subsidence, work by Johnston et al. (1998) suggests that a bending moment will increase lateral compressive stresses at shallow depths, while decreasing compressive stresses at greater depths.

Within the CRBG, Reidel et al. (1989) indicates that the Columbia River Plateau has been undergoing subsidence at a decreasing rate (0.1–0.003 cm yr^{-1}) since the Grande Ronde eruptions. The occurrence of regional subsidence after CRBG emplacement suggests that the entire CRBG assemblage has been undergoing flexure, which would result in a bending moment about the longitudinal axis of the underlying bedrock depression (~N42°E). The presence of a bending moment about this longitudinal axis further suggests that bending moment stresses would manifest in the direction orthogonal to the longitudinal axis of the subsiding basin, the result of which would impose compression above the neutral axis and tension below the neutral axis. Within the CRBG, bending moment stresses acting orthogonal to the longitudinal axis of the underlying bedrock depression would preferentially affect fracture apertures (and thus permeability) oriented parallel to longitudinal axis of the underlying depression (Fig. 4.5), which we interpret as the process that results in spatially correlated permeability parallel to the longitudinal axis.

In the context of the CRBG *k*-*z* profile, most permeability data are from portions of the CRBG with depths ranging from ~1,000–4,000 m, which suggests a neutral axis between 500 and 2,000 m depth. Although this variability in CRBG thickness will dilute the signal of reversal in the *k*-*z* trend, the distinct permeability decay between 500 and 950 m combined with the modestly increasing permeability beyond 950 m depth suggests that the bending moment stress model reasonably explains the observed *k*-*z* trend even when taking into account the variable thickness of the CRBG.

In the context of other LIPs, Coffin and Eldhom (1994) compiled and analyzed all in situ LIPs younger than 250 Ma and show that LIP emplacement is generally characterized by lithospheric uplift, rapid emplacement, and post-emplacement subsidence, which implies that bending moment stresses may also be characteristic features of continental LIPs. Based on the present analysis of CRBG permeability architecture, the broader implication is that the *k*-*z* characteristics of continental LIPs may not follow classical decay trends. Because fracture permeability governs the rate of mass and heat flow through the mafic rocks (e.g., Garven, 1995), the bending moment hypothesis for the permeability architecture of continental LIPs may have important implications for groundwater resource management, geothermal heat flow, and the development of geo-engineered reservoirs. For example, Saar (2011) suggests that minimum permeability for thermal advection is 5×10^{-17} to 10^{-15} m^2, and, as a result, the thermal signature of continental LIPs may exhibit unusual characteristics alternating between advection and conduction at depths below the neutral surface of the bending moment. Moreover, continental LIPs continue to be considered for a wide range of geological engineering applications, including long-term nuclear waste storage, natural gas storage, and geologic CO_2 sequestration (Gephard et al., 1983; McGrail et al., 2017; Reidel et al., 2002), the feasibility of which depend to a large extent on the hydraulic architecture of the host reservoir.

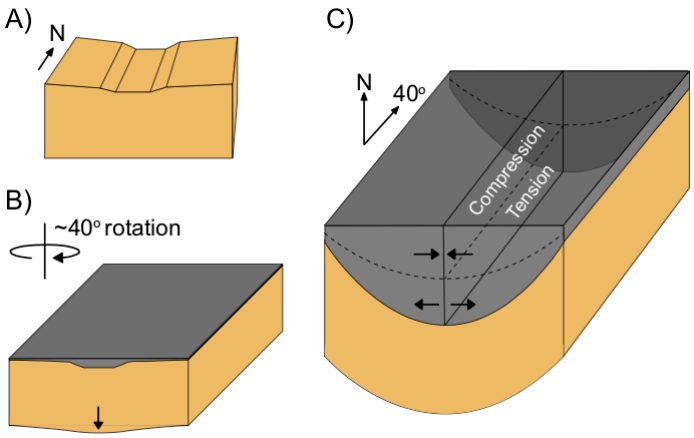

Figure 4.5: *Schematic illustrating the effects of a bending moment on Columbia River Basalt Group (CRBG, western USA) permeability. A: Prior to Imnaha eruptions (17–15.5 Ma), the paleobasin was oriented north (Long and Wood, 1986). B: Columbia River Plateau experienced 40°E rotation contemporaneously with initial CRBG emplacement at ca. 17 Ma. C: ~94% of total CRBG volume was emplaced between 17 and 15.5 Ma, which resulted in rapid loading and post-emplacement subsidence, and induced a bending moment about the longitudinal axis of the basin oriented N40°E. Arrows denote compression and tension above and below the neutral axis (dashed line), respectively, and orthogonal to the longitudinal axis.*

4.5 Summary

Permeability-depth (*k*-z) scaling is frequently invoked to explain and/or model the effects of fluid and heat flow on numerous societally relevant geological processes. In this study, we find that continental large igneous provinces may deviate from the classical permeability decay trend. Results show that CRBG permeability (1) exhibits little depth dependence between 0 and 500 m; (2) systematically decays between ~500 and 950 m depth; and (3) increases by 1.5 orders of magnitude between 950 and 1,450 m depth. Further analysis indicates that CRBG permeability is spatially correlated with a 5:1 horizontal anisotropy ratio, and the direction of maximum horizontal spatial correlation is parallel to the longitudinal axis of the bedrock depression underlying the CRBG. To explain these observations, we hypothesize that rapid CRBG emplacement and subsequent lithospheric subsidence has induced bending moment stresses within the CRBG that affect the depth-dependence and spatial correlation of fracture-controlled permeability. Because upflit, rapid loading, and post-emplacement subsidence generally characterize continental LIP emplacement, we infer that the effects of bending moment stresses may be a characteristic feature of the LIP permeability structure.

Table 4.1: *Semivariogram parameters*

Horizontal Semivariogram			
Model Type	Nugget	Sill	Range (km)
Exponential*	0.45	0.55	35
Exponential†	0.45	0.55	7.5
Vertical Semivariogram			
Model Type	Nugget	Slope	ω§
Power	0.4	1.55	0.35

*N40°E: Direction of max. spatial correlation
†N130°E: Direction of min. spatial correlation
§Exponent for power law semivariogram

5. QUANTIFYING CO_2 INJECTIVITY AT 95% OF BOREHOLE BREAKDOWN PRESSURE AT WALLULA SITE

5.1 Objective

In this study, we combine our knowledge of CO_2-brine relative permeability in fractured basalt (Section 2), outcrop-scale CO_2 flow in basalt fracture networks (Section 3), and regional-scale permeability structure of the Columbia River Basalt Group (Section 4) with borehole data from Wallula Basalt Sequestration Pilot Project (McGrail et al., 2009) to develop probabilistic estimates of CO_2 storage capacity from a single injector at pressure below the regional fracture gradient. In doing so, this study combines geostatistical reservoir simulation with multiphase, multicomponent numerical modeling to investigate the influence that the spatial distribution of permeability has on the geomechanical reservoir response of the Grande Ronde associated with an injection of supercritical CO_2. The model scenario is designed to represent a large-scale constant mass injection of supercritical CO_2 into the composite injection zone (775 m - 875 m) at the Wallula Pilot Borehole. While the hydrologic characterization within the Wallula Pilot Borehole has been extensive, the permeability distribution at intermediate- to long-range spatial scales is poorly constrained. To quantify the effects of this uncertainty, this study develops a Monte Carlo simulation strategy in which CO_2 injection is simulated in 50 equally probable reservoirs with spatially distributed permeability in each domain. The permeability distribution is randomly generated, but constrained by (i) Wallula borehole geology, (ii) the regional-scale permeability correlation model developed in Section 4, and (iii) the cumulative distribution of CRBG permeability. This approach yields a model with expected behavior (mean), as well as a quantitative measure of uncertainty.

5.2 Methods

5.2.1 Model Domain

The model domain for this study comprises an areal extent of 5,000 m × 5,000 m × 1,250 m, which represents ground surface to 1,250 m depth with the Wallula Pilot Borehole centrally located (Fig. 5.1). This domain is discretized into 530,000 grid blocks with dimensions of 50 m × 50 m × 25 m. For this model, the CRBG is conceptualized on the basis of basalt flow morphology, which is a layered heterogeneous system consisting of highly fractured flow tops (high permeability) and flow interiors (low permeability). However, this layered heterogeneity does not consider the wide range of permeability within individual basalt flow units, which are known to be internally heterogeneous due to the ubiquitous fracture networks within CRBG basalt. In order to account for the wide range of fracture-controlled permeability within the composite injection zone (775 - 875 m depth), sequential indicator simulation (sisim) is employed to generate stochastic permeability distributions for the injection zone (Deutsch and Journel, 1998). In this approach, the sisim routine selects grid cells in random order and solves the ordinary kriging equations on the basis of (1) the cumulative distribution function for CRBG permeability, (2) known data points, which are the borehole permeability tests from the Wallula borehole, (3) previously simulated grid cells, and (4) the chosen spatial correlation model, which for this study is an anisotropic semivariogram model developed by Jayne and Pollyea (2018).

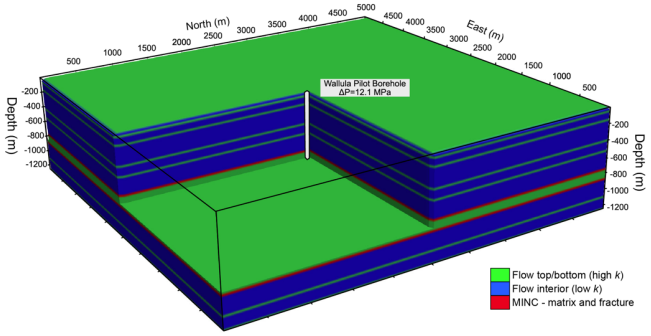

Figure 5.1: *Model domain for CO_2 injection modeling study. The composite injection zone is bounded by the two red layers, the latter of which are specified as multiple interacting continua (MINC) to represent fracture-matrix flow within the bounding entablature units.*

Jayne and Pollyea (2018) show that permeability within the Columbia River Plateau exhibits a direction of maximum and minimum spatial correlation oriented at N40°E and N130°E, respectively. In order to calculate these spatial correlation models Jayne and Pollyea (2018) compiled a regional database of CRBG permeability values from wells within the CRBG (Fig. 4.1, 5.2A) to calculate semivariograms. To do this, permeability values were filtered on two standard deviations of the mean to ensure only the highly productive flow tops and bottoms were included in the calculations (Figure 5.2). The present study adopts this convention to constrain the ranges of permeability within the high permeability zones that are representative of the composite injection zone. This results in a range of log permeabilities from -8.5 m^2 to -14.5 m^2 with a median log permeability value of -11.5 m^2. However, the present study is focused on permeability at depths greater than 750 m, where the log permeability in the

Wallula Pilot Borehole is ~-14.5 m^2. In order to account for this, the permeability distribution is translated so that the variability of permeability is maintained but the mean permeability is representative of the composite injection in the Wallula Pilot Borehole (Fig. 5.2B). This results in a log permeability range from -11 m^2 to -17 m^2. Using this approach, a total of 50 equally probable injection zones are simulated and inserted into the model domain between 775 and 875 m.

In order to model the effects of fracture-matrix flow within the entablature zones bounding the composite injection layer, the multiple-interacting-continua (MINC) method is utilized to produce a dual-permeability model that is representative of columnar jointing typical of basalt flow entablatures. The MINC method is a generalized dual-porosity concept, which allows for partitioning of the flow domain into different computational volumes within each element (Pruess, 1992). In this approach, grid blocks are considered to be "nested within one another allowing a single grid block to be defined by multiple finite elements (multiple rock properties can be used, such as, for fractured and unfractured rock matrix). A total of 50-equally probable synthetic reservoirs are simulated in which permeability within the injection zone is stochastically generated by sequential simulation and the entablature zones bounding the injection layer are modeled as a dual-continuum to represent columnar jointing. The relative permeability and capillary pressure models along with the bulk fluid and rock properties are listed in Table 5.1.

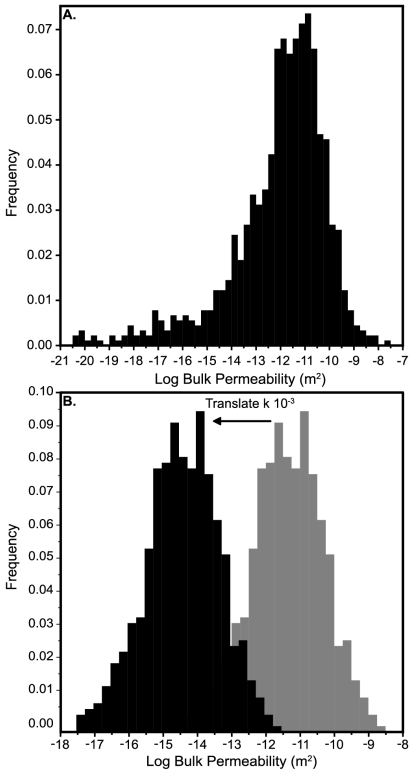

Figure 5.2: *A. Histogram of log permeability from well data compiled by Jayne and Pollyea (2018). B. Histogram of the filtered permeability data to represent the high permeability flow tops. The mean of log permeability is 11.5 m^2 (grey), in order to make this range of permeabilities more representative at the depth of the injection zone the permeability distribution is translated downward so that the mean log permeability is -14.5 m^2, which is congruent with field test from the Wallula borehole.*

5.2.2 Numerical CO_2 Flow Simulation

In order to investigate how the spatial distribution of permeability affects CCS reservoir performance in a flood basalt reservoir, CO_2 injection is simulated within each equally probable synthetic reservoir at constant pressure for 20 years. Constant pressure injections are simulated for this study within the composite injection zone at the Wallula Pilot Borehole to not only investigate the distribution of supercritical CO_2, but also compare the total mass of CO_2 injected over all 50 simulations. A constant overpressure of 12.1 MPa is used to simulate the CO_2 injection. This injection pressure represents 95% of the borehole breakout pressure as calculated by Pollyea (2016), borehole breakout pressure is used so that the maximum amount of CO_2 can be injected in each simulation without borehole failure. The code selection for this study is TOUGH3 (Jung et al., 2017) compiled with the ECO2M module (Pruess, 2011). TOUGH3 solves energy and mass conservation equations for nonisothermal, multiphase flows in a porous geologic media. The ECO2M module simulates mixtures of H_2O-NaCl-CO_2, within the following ranges for temperature, pressure, and salinity conditions: 10°C < T < 110°C, pressure < 60 MPa, and salinity from zero up to full halite saturation. ECO2M can also simulate all possible phase conditions for CO_2-brine mixtures, including transitions between super- and sub-critical CO_2 as well as phase transitions between liquid and vapor CO_2 (Pruess, 2011).

Initial conditions are specified with a hydrostatic pressure gradient ranging from 0.101 MPa (1 atm) at ground surface to 12.3 MPa at the bottom of the Wallula Pilot Borehole. Initial temperature is calculated by using the regional heat flux ~65 mW/m^2 (Pollack et al., 1993) as a thermal boundary at the base of the model and a constant temperature of 10°C at ground surface, resulting in a linear temperature gradient from 10°C at the surface to 50°C, and thermal effects are accounted for in the simulations. These initial conditions are consistent with the field measurements taken at the Wallula Pilot Borehole (McGrail et al., 2009). Within the composite injection zone, initial temperature and pressure conditions range from 35 – 38°C and 7.7 – 8.4 MPa, which are within the supercritical field for CO_2. Dirichlet boundary conditions are specified at the upper boundary of the model domain to hold pressure and

temperature constant at ground surface and at the lateral boundaries of the model domain to maintain temperature and pressure gradients in the far-field.

As with all modeling studies, a brief mention of the limitations of this model is warranted. This modeling study does not account for basalt dissolution or secondary mineral precipitation, and, as a result, this modeling study represents a conservative estimate of CO_2 storage capacity and leakage potential. Consequently, permeability alteration due to secondary mineral precipitation is neglected; however, we note that empirical permeability-porosity relationships have not yet been quantified in basalt reservoirs. Additionally, relative permeability hysteresis is not accounted for in the simulations, because only the injection phase of a CCS project is simulated so there is no imbibition for the wetting phase. Similarly, chemical diffusion is not accounted for because CO_2 is being continuously injected throughout the entire simulation resulting in a high Peclet number, which means the transport of mass and heat is dominated by advection.

5.2.3 Data Analysis

A total of 38 individual simulations were completed during the project period. While we initially planned for an ensemble of 50 runs, convergence issues 12 of the simulations and these problems were irreconcilable prior to project closeout. Nevertheless, the ensemble of 38 simulations are analyzed using e-type estimates on a grid cell by grid cell basis to quantify the average overall behavior of CO_2 and pressure at the reservoir scale, as well as the corresponding spatial uncertainty (Duetsch and Journel, 1998). In this approach, the mean (N=38) CO_2 saturation $\bar{S}_{(x,y,z)}$within each grid cell is computed as:

$$\bar{S}_{(x,y,z)} = \frac{1}{38}\sum_{i=1}^{38} S_{i(x,y,z)}$$

where, $S_{i(x,y,z)}$ is the modeled CO_2 saturation for simulation i at location (x, y, z). Similarly, the variance $(s^2_{(x,y,z)})$ associated with Equation 1 for each grid cell is computed as:

$$s^2_{(x,y,z)} = \frac{1}{38}\sum_{i=1}^{38}(S_{i(x,y,z)} - \bar{S}_{i(x,y,z)})^2$$

In the present study, the mean and variance are calculated for free-phase CO_2 saturation over all 38 simulations. This approach is also implemented to calculate mean and variance for pore fluid pressure over all 38 simulations, which are then used calculate shear failure, tensile failure, and fracture dilation.

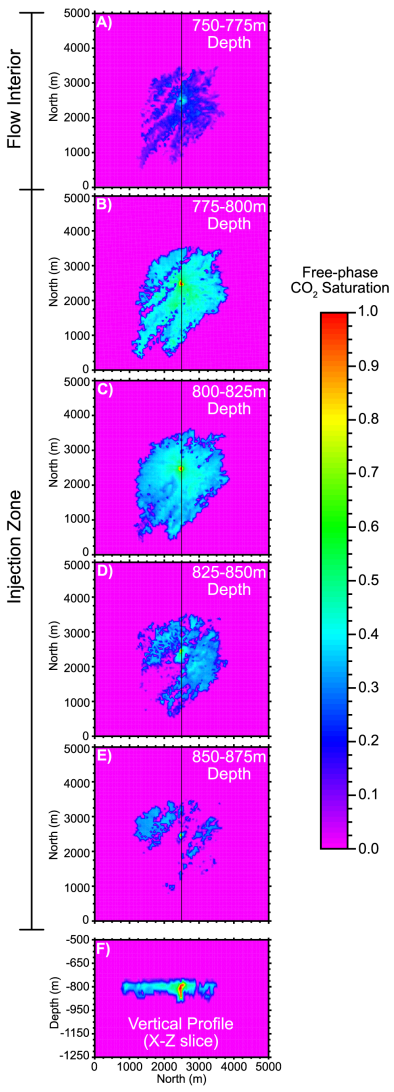

Figure 5.3: *Single realization (#20) of a 20-year constant pressure CO_2 injection. A. represents the layer above the injection zone and illustrates that free-phase CO_2 is present within the fractures. B-D. each represent an individual injection layer within the Wallula Pilot Borehole. E. A vertical north-south profile through the center (indicated by the black lines in A-E) of the model domain.*

5.3 Results

Each numerical model accounts for 20 years of simulation time, in which supercritical CO_2 is injected within the Wallula Pilot Borehole at a constant pressure of 12.1 MPa above initial conditions. For each analysis the simulations are referred to by an integer index (1-50). In order to maintain consistency and facilitate comparison each analysis includes simulation 20 because the total mass of CO_2 injected for this simulation is close to the ensemble mean. The result of simulation 20 is represented by Figure 5.3, which shows free-phase CO_2 saturation after 20 years. The e-type estimates (grid cell mean and variance) for the ensemble of 50 simulations are presented in Figure 5.4. In order to compare the injectivity within each simulation the total amount of CO_2 injected in million metric tons (MMT) is calculated, as well as, the corresponding histogram as illustrated by Figure 5.5. To compare the volumes injected throughout this modeling study 3D plots of CO_2 plumes from four different realizations which

represent the minimum (33), maximum (43), and average (11 and 20) volume of CO_2 injected after 20 years are shown in Figure 5.6. The fracture continua that bound the injection zone represent fractures within the low-permeability flow interior, e-type estimates are calculated for CO_2 saturation in Figure 5.7. In order to evaluate the thermal effects of free-phase CO_2 flow within the target reservoir, Figure 5.8 illustrates the change in temperature from pre- to post-CO_2 injection within the model domain. Additionally, a plot comparing the temperature and CO_2 saturation over time from two grid cells in the entablature zone 50 m away from the injection well in a single realization (20) are presented by Figure 5.9.

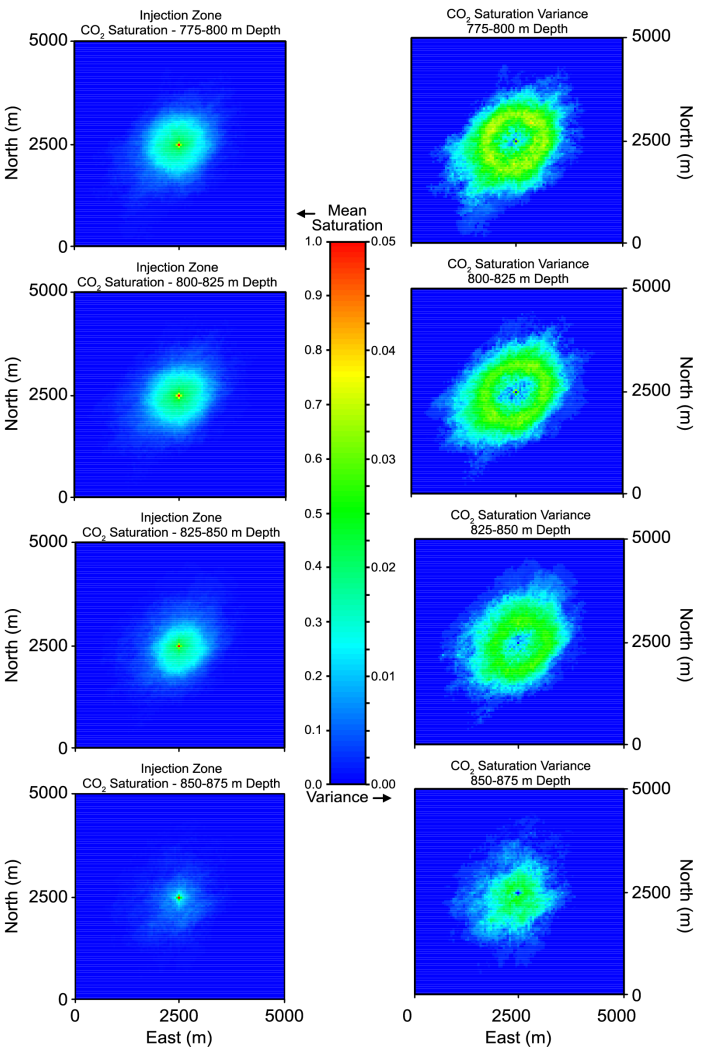

Figure 5.4: *E-type estimates for (N=50) 20-year CO_2 injections. Average free-phase CO2 saturation over all 50 simulations for the injection zones are shown on the left and the variance over all 50 simulations is shown on the right.*

5.4 Discussion

Spatial heterogeneities are present at all geologic scales, from core samples (Li and Benson, 2015) to reservoir scale (Doughty and Pruess, 2004). Understanding how spatial heterogeneity affects fluid flow is critical for engineered CCS reservoirs in terms of monitoring, management, and verification (MMV). Reservoirs that are targeted for CCS require extensive site characterization to ensure that the reservoir meets the requirements for capacity, injectivity, and confinement for a given CCS project. Numerical models are commonly used to predict what effects a large-scale CO_2 injection will have on the target reservoir and the behavior of the CO_2 plume. However, many numerical modeling studies employ a homogeneous rep- resentation of the geologic media (Van der Meer, 1995; Pruess and Garcia, 2002; Pruess et al., 2003). For example, at the reservoir-scale it is common to implement a layered heterogeneity approach with internally homogeneous rock properties. Doughty (2010) simulates an injection of 1.1 million metric tons of CO_2 into a dipping sedimentary basin to investigate the spatial and temporal evolution of the CO_2 plume. While this approach may be reasonable for some geologic environments, it is also well established that uncertainty with the model parameters, such as, permeability will strongly affect the direction and extent of the CO_2 plume (Doughty, 2010). Moreover, Doughty and Pruess (2004) investigate the physical processes associated with the sequestration of supercritical CO_2 and show that the highly heterogeneous nature of geologic media results in the formation of preferential flow paths which have a significant impact on the overall behavior of the injected CO_2. While knowing the distribution of reservoir properties at the reservoir-scale are generally unknowable, previous studies have shown that some reservoir properties can be described by a probability distribution. For example, Law et al. (1944) investigated three horizons from a sandstone reservoir and indicates that permeability follows a log-normal probability distribution. Lindberg (1989) studied synthetic fracture permeability distributions within CRBG core samples and reported that fracture aperture follows a log-normal distribution, which can be related to permeability (e.g. parallel-plate cubic law). Utilizing probability distributions is one way to account for the heterogeneity and uncertainty associated with some reservoir properties, such as, permeability. More recently, studies have investigated the effects of permeability heterogeneity by

creating randomly generated permeability distributions that follow a log-normal distribution (Li and Benson, 2015; Gierzynski and Pollyea, 2017). In order to account for permeability heterogeneity this study utilizes the distribution of permeability representative of the CRBG from previously published data (Fig. 5.2).

The effect of spatially correlated permeability within the CRBG is apparent in Figure 5.3, which illustrates CO_2 saturation within each layer of the injection zone for a single realization. When comparing the accumulation and distribution of CO_2 within each layer in Figure 5.3, it is clear that top injection layer (Fig. 5.3B) has the largest volume of CO_2 and this is due to buoyancy forces and the high permeability pathways that have formed due to the spatial heterogeneity. The combination of buoyancy-driven upward CO_2 flow and permeability heterogeneity results in CO_2 saturation patterns from the injection zone super- imposed on the overlying entablature zone, which is the reservoir confining layer (Fig. 5.3A). As a result, permeability heterogeneity in the injection zone controls not only the accumulation and distribution of CO_2 within the reservoir, but also possible leakage pathways into the confining layers. High permeability path- ways are apparent within the injection zone (Fig. 5.3D,E) where there are small amounts of CO_2 that are completely disconnected from the main portion of the plume. This is due to the spatial distribution of permeability and the pressure gradient caused by the injection. As CO_2 is injected and migrates out into the formation, the CO_2 reaches areas of low permeability, which can inhibit flow. This causes injection pressure to accumulate, which causes the CO_2 to take the path that is most energetically favorable. In some instances, this effect forces vertical CO_2 flow as shown in Figure 5.3E. These results are congruent with those of Doughty and Pruess (2004) and show that there are high permeability pathways both horizontally and vertically. It is also important to note the control that the anisotropic permeability correlation structures exhibit on the accumulation and distribution of CO_2 in a single simulation. In simulation 20 (Fig. 5.3) the injected free-phase CO_2 has migrated ~2400 m away from the injection well parallel to the direction of maximum correlation (N40°E) (Fig. 5.3B), where as, CO_2 has only migrated ~1100 m parallel to the direction of minimum spatial correlation (N130°E) (Fig. 5.3C).

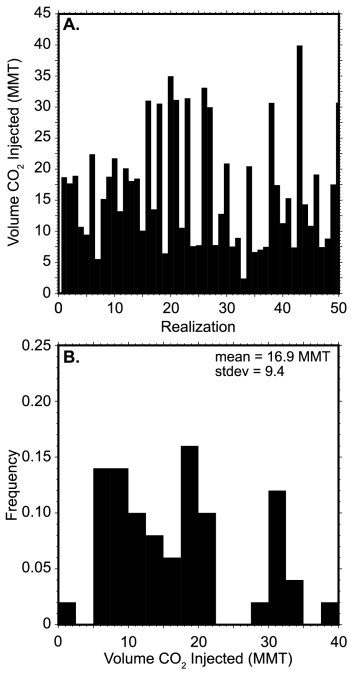

Figure 5.5: *A. Total volume (million metric tons) injected after 20 years of simulation for each of the 50 realizations. B. Histogram of the total volume injected of all 50 simulations along with the mean and standard deviation of the injected volume.*

The complete ensemble simulation results (e-type estimates) for free-phase supercritical CO_2 saturation after 20 years of injection are shown in Figure 5.4. The mean CO_2 saturation in each injection layer appears to form a circular-shaped plume, which is similar to the individual model results from McGrail et al. (2009) and Bacon et al. (2014). Interestingly, these latter studies implement radially symmetric model domains with layered heterogeneity and internally homogeneous injection zones to simulate an injection of 1000 MT of CO_2 at the Wallula Pilot Borehole. Although, results from McGrail et al. (2012) are more comparable to this study due to the volume and length of the CO_2 injection simulated. McGrail et al. (2012) uses a radially-symmetric grid to simulate an annual injection of 0.8 MMT supercritical CO_2 into the Grande Ronde formation and sub-basalt sediment layers and show that after 10 years of injection the CO_2 migrates ~500 m from the injection well and ~1,000 m after 30 years. In comparison to the results from McGrail et al. (2012), Figure 5.4 illustrates after 20 years of a CO_2 injection that the plume migrates ~900 m from the injection well. While the ensemble mean behavior of CO_2 from this study is similar to the results from studies with internally homogeneous injection reservoirs, the variability in this study reveals drastically different results.

The variance of CO_2 saturation over all 50 simulations is shown in Figure 5.4, which illustrates an 'ellipse' of variability extending up to ~1,800 m away from the injection well. The longitudinal axis of the ellipse trends N40◦E, which is the direction of maximum spatial correlation. This result suggests that the uncertainty of CO_2 migration within CRBG basalt is strongly governed by the permeability correlation structures. This variability associated with the CO_2 plume is similar to the results of Pollyea and Fairley (2012), which implements a Monte Carlo simulation strategy to quantify the effects of spatial heterogeneity in low-volume basalt formations typical of the east Snake River Plains, Idaho. In this study, the ensemble variance exhibits a similar 'ring of uncertainty' with a very large range of variability within the basalt reservoir. While these results are similar, these studies differ with respect to geologic media

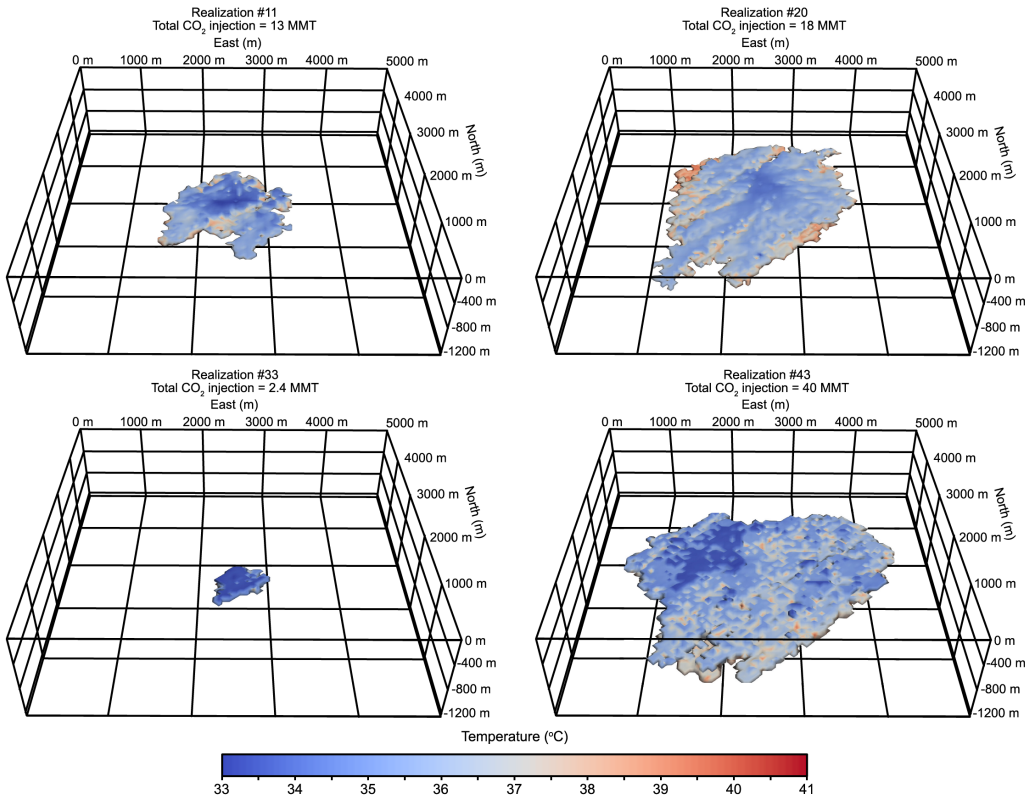

Figure 5.6: *Four different realizations after a 20-year CO_2 injection. Isosurface represents the edge of the CO_2 plume, each plume is contoured by temperature. The range of potential outcomes for total CO_2 disposal after 20 years of constant pressure injection is 2.4 – 40 million metric tons.*

being studied (low-volume basalts vs. flood basalts) and the correlation ranges use to create the permeability distributions. Pollyea and Fairley (2012) uses a geostatistical analysis of an outcrop scale low-volume basalt with a maximum correlation range of 38 m to simulate a reservoir-scale CO_2 injection, while this study uses a regional-scale geostatistical analysis with a correlation structure of 35 km presented by Jayne and Pollyea (2018). Overall, the ensemble analysis indicates that the mean CO_2 plume geometry exhibits a circular shape around the injector, while the variance corresponding with this result is strongly affected by the direction of maximum spatial permeability correlation.

The variability over all 50 simulations is not only obvious in the shape of the individual plumes (Fig. 5.3) and the ensemble variance (Fig. 5.4), but also in the total volume injected in each simulation. The total volume of CO_2 injected into each of the 50 equally probable synthetic reservoirs ranges from a nominal 2.4 MMT (0.12 MMT yr^{-1}) to 40 MMT (2 MMT yr^{-1}), as shown in Figure 5.5. For reference, a small-scale 37 MW bio-mass fueled electric generator would emit ~0.8 MMT yr^{-1} (McGrail et al., 2012) and for a large-scale 1000 MW gas-fired power plant would produce ~ 1.36 MMT yr^{-1} of CO_2. For equally-probable reservoirs, this is a significant amount of variability (Fig. 5.5B). If the scenario presented by McGrail et al. (2012) were implemented at the Wallula Borehole, the results from this study show that a constant pressure injection at 95% of the borehole breakout pressure would result in 60% of the equally probable reservoirs successfully accepting enough CO_2 to meet the criteria for a 37 MW electric generator. Conversely, that would mean that 40% of the synthetic reservoirs would fail with the given scenario and if a larger volume of injected CO_2 were required the chances of success would quickly decrease. For example, only 20% of the reservoirs would have the injectivity for a modest increase in the injection rate to 1.15 MMT yr^{-1}.

In order to visualize the variability in CO_2 injection volume for constant pressure injections, Figure 5.6 illustrates the isosurface at 1% gas saturation for four individual realizations, which represent the simulation closest to the mean CO_2 volume (Fig. 5.6, realization 20), one standard deviation from the mean (Fig. 5.6 realization 11), and the minimum and maximum CO_2 volumes (Fig. 5.6, realizations 33 and 43, respectively). This variability in CO_2 plume shape and volume injected over the ensemble of

simulations has important implications for MMV practices. There is a wide variety of methods available to monitor a CO_2 injection, such as, geophysical methods (e.g. seismic, electrical, gravity), pressure monitoring, well logging, fluid sampling, and soil gas monitoring. Each of these methods have their benefits but they also have drawbacks, e.g. detection occurs after potential impacts have occurred, significant effort for null result (Benson et al., 2006). Mathieson et al. (2010) discusses the monitoring and verification methods carried out at a CO_2 sequestration site in Algeria and emphasizes that CO_2 plume development is far from homogeneous and that each storage site is unique, which requires a specific monitoring program tailored to the risks at each site. The results presented here show that the average CO_2 plume behavior may exhibit characteristics of an isotropic permeability distribution, but the variability over all 50 simulations is significant, and warrants a site-specific monitoring program. In the case of the Wallula Site, leakage from the composite injection zone into the bounding entablature layers is a concern due to the highly-fractured nature of the CBRG. E-type estimates for the layers bounding the composite injection zone are presented in Figure 5.7. Owing to buoyancy forces, free-phase CO_2 migrates upward into the fractures within the flow interior and Figure 5.3A, B illustrate how spatial heterogeneity in the injection layer impacts the CO_2 plume shape within the flow interior. While the CO_2 saturation in Figure 5.7 is minimal compared to the injection zones, these results show that 0.1 - 1.05% of the total volume injected has migrated outside of the composite injection zone. The USDOE (2013) requires that a successful CCS project keeps >99% of the injected CO_2 isolated within the reservoir for one-thousand years. However, in no simulation did the injected CO_2 migrate farther than the layers immediately bounding the composite injection zone, which is an area for possible mineralization of the CO_2. These results are also congruent with the high-resolution fracture modeling of Gierzynski and Pollyea (2017), which shows that CO_2 flow tends to converge on a single flow path within a fracture network and suggests that this flow path convergence leads to a physical trapping mechanism followed by possible mineralization.

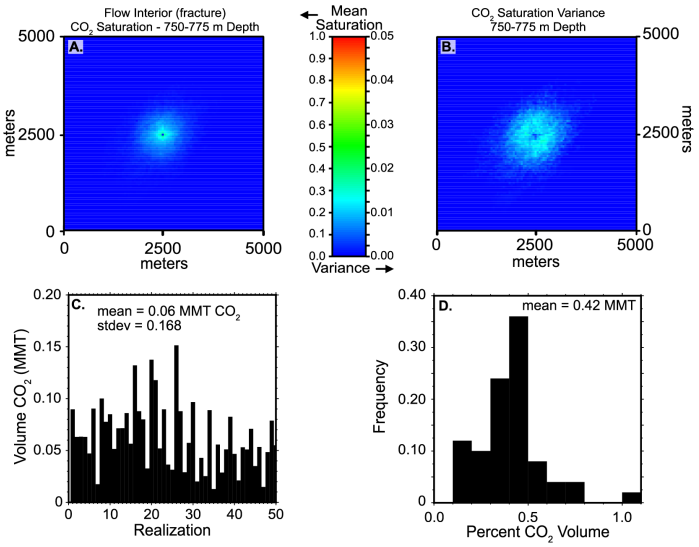

Figure 5.7: *E-type estimates for average CO_2 saturation (A) and variance (B) for the flow interior layer bounding the injection zone. C. Total volume of CO_2 in million metric tons (MMT) within the flow interior. D. Histogram showing the percentage of the total volume injected that has migrated to into the flow interior.*

Additionally, results from this study indicate that the thermal effects of a CO_2 injection may also be used for MMV practices. Specifically, the change in reservoir temperature from pre- to post-injection shows that temperature within the reservoir changes +/- 4°C as a result of the CO_2 injection (Fig. 5.8). The areas that show the largest increase in temperature are near the edges of the CO_2 plume, while areas that show the largest decrease in temperature are near the injection well. At the edges of the CO_2 plume, CO_2 dissolves into the reservoir water and this is an exothermic reaction that releases heat, which is referred to as the heat of dissolution (Pruess, 2005). In contrast, the cooling shown in this study is caused by Joule-Thomson expansion which describes the temperature change associated with the expansion of a gas (Roebuck et al., 1942). During CO_2 injections, the CO_2 is injected at a high pressure and begins to expand and cool as it migrates away from the injection well (Oldenburg, 2007). The competing effects of the heat of dissolution and Joule-Thomson expansion are shown in Figures 5.6 and 5.8. The isosurfaces in Figure 5.6 are contoured by temperature to illustrate the competing temperature effects of a large-scale CO2 injection. As the CO_2 migrates away from the wellbore due to the pressure gradient imposed by the injection, the CO_2 begins to expand and cool, but at the edges of the plume the CO_2 is dissolving into the reservoir water and giving off enough heat to overcome Joule-Thomson cooling resulting in a net increase in temperature. Conversely, near the wellbore after some time the water becomes saturated with CO_2 and no more CO_2 will dissolve. At this point, Joule-Thomson cooling dominates resulting in a net decrease in temperature near the well (Figure 5.8A-C,E). This result suggests that the competing effects of dissolution heating and Joule-Thomson cooling may be an effective strategy to monitor breakthrough. Namely, the heat of dissolution effect may be used to predict

CO_2 breakthrough at monitoring wells within the reservoir. As the CO_2 dissolves into the reservoir water and releases heat, both the CO_2 and reservoir water experience an increase in temperature. This results in a thermal anomaly that migrates throughout the reservoir slightly ahead of the free phase CO_2 plume. If this is true, then we would expect an increase in temperature would reach a monitoring well before the CO_2 plume. This effect is illustrated in Figure 5.9, which shows how temperature and CO_2 saturation change over the course of the CO_2 injection at two monitoring locations 50 m away from the wellbore. In Figure 5.9 the first change in temperature occurs after 6 days of simulation. Over the next 15 days the black line (red line shows a similar trend) steadily increases in temperature from 34.5°C to 35.5°C, then continues to increase in temperature up to 36.8°C by day 26. At day 26, the maximum temperature at this monitoring location is reached, which occurs contemporaneously with the first appearance of CO_2. For the given simulation, two grid blocks located within the layer bounding the composite injection zone exhibit a steady increase in temperature until the arrival of CO_2 which suggests that temperature may be a proxy for CO_2 breakthrough. These results suggest that thermal monitoring may be an effective predictor of CO_2 breakthrough, however more research is needed in this area of study.

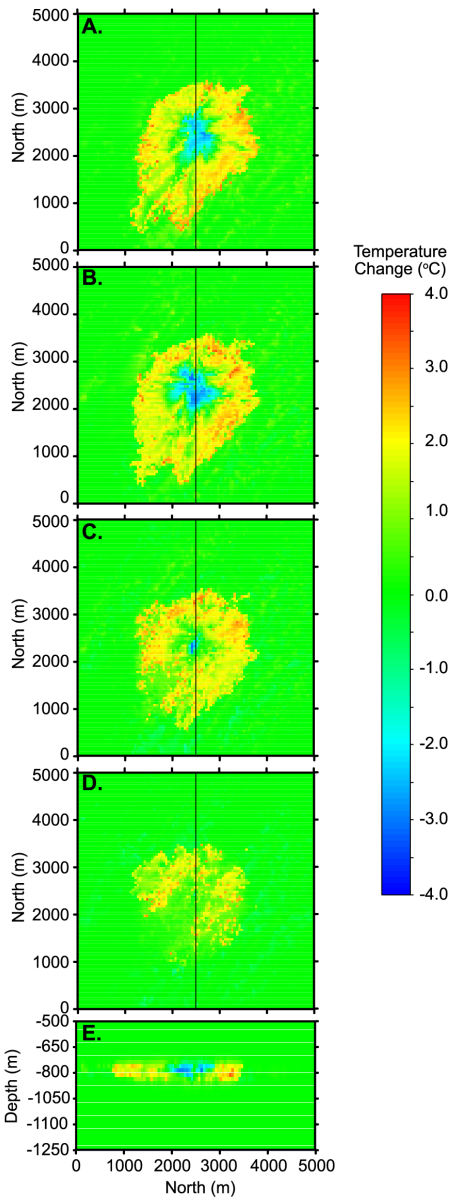

Figure 5.8: *Temperature change in realization #20 after 20 years of constant pressure CO_2 injection. Panels A-D. represent the 4 injection layers within the model domain. Panel E shows the vertical north-south section through the center (indicated by the black lines in A-D) of the model domain.*

5.4 Summary

Flood basalts have been gaining recognition as potential reservoirs for carbon capture and sequestration. The success of recent field experiments in Washington State, USA, and Iceland have validated that injected CO_2 will interact with the basalt to form carbonate minerals at the field-scale and very short timescales. Upscaling these field-scale experiments is required if CCS is to be used as a way to mitigate climate change. However, there are a number of uncertainties associated with upscaling to an industrial-scale CO_2 injection. For example, incomplete knowledge of multiphase flow in highly heterogeneous basalt reservoirs and detailed reservoir characterizations are required for proper numerical modeling and to effectively design a monitoring, measuring, and verification plan. This study investigates the uncertainty of a large-scale CO_2 injection into a highly heterogeneous basalt reservoir by focusing on the effects of spatially distributed permeability on CO_2 plume migration. The primary results from this study are summarized as:

1. The aggregate behavior of the 50 simulations results in a concentric CO_2 plume shape around the injection well, which suggests that ensemble behavior is not governed by the spatial correlation structures.
2. Ensemble variance shows an ellipse of uncertainty around the CO_2 plume that extends up to 1,800m away from the injection, this ellipse trends parallel to the direction of maximum spatial permeability correlation, suggesting that the uncertainty associated with a large-scale CO_2 injection is strongly controlled by the permeability correlation structures. This means that spatial variability must be accounted for to fully understand how variability propagates into operational and MMV decisions.

3. Injected CO_2 migrates from the injection zone into the entablature layer bounding the injection zone, but the CO_2 does not migrate any further suggesting that this region has the potential for CO_2-water-basalt interactions to effectively isolate large-scale CO_2 injection volumes.
4. The volume of CO_2 injected at 95% of the borehole breakout pressure for 20 years ranges from 2.4 MMT (0.12 MMT yr^{-1}) to 40.0 MMT (2.0 MMT yr^{-1}). While the minimum volume injected is eight times less than what would be required for the proposed scenario of offsetting the carbon emissions from a 37 MW generator. The maximum volume injected could support at 1,000 MW gas-fired power plant with a single injection.
5. Non-isothermal effects, namely the heat of dissolution associated with a large-scale CO_2 injection may be an effective MMV strategy for monitoring CO_2 breakthrough.

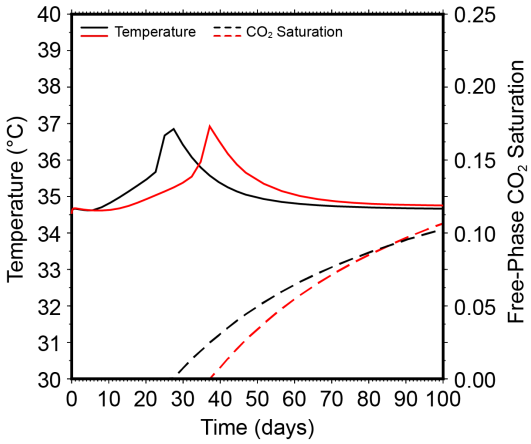

Figure 5.9: *Temperature and CO_2 saturation versus time for two monitoring locations within the entablature layer (750 - 775 m depth) 50 m away from the injection.*

In conclusion, these results suggest that the implementation of a regional-data set and spatial correlation structures into a numerical model can provide insights into the behavior of CO_2 flow in highly heterogeneous reservoirs. Additionally, these results illustrate the uncertainty associated with highly-heterogeneous flood basalt reservoirs and a CCS project would require extensive reservoir characterization and a unique monitoring, measuring, and verification plan. Significantly more research is required to develop a better under- standing of the reactive transport, geomechanical, and thermal processes associated with an industrial-scale CO2 injection into a flood basalt reservoir.

Table 5.1: Model parameters

Bulk Rock Properties				
	Matrix	*Fracture*	*Flow Top*	*Basal Boundary*
Density (kg m^{-3})	2900	2300	2300	2900
Porosity	0.05	0.1	0.3	0.05
Permeability (m^2)	10^{-20}	10^{-16}	varies	10^{-20}
Thermal Conductivity (W m $°C^{-1}$)	2.11	2.11	2.11	2.11
Heat Capacity	840	840	840	840

Multi-Phase Properties			
Relative Permeability		*Capillary Pressure*	
λ	0.55	λ	0.457
S_{lr}	0.3	S_{lr}	0.0
S_{ls}	1.0	P_o (kPa)	20,000
S_{gr}	0.25	S_{ls}	1.0

6. PRODUCTS

6.1 Peer-Reviewed Journal Articles (†Student Author)

†Dahshan, M., Polys, N.F., †Jayne, R.S., and Pollyea, R.M. Making sense of scientific ensembles with semantic interaction, *Computer Graphics Forum*, pending revisions.

†Jayne, R.S., †Wu, H. and Pollyea, R.M. Geologic CO_2 sequestration and permeability uncertainty in a highly heterogeneous reservoir, *International Journal of Greenhous Gas Control*, pending revisions.

†Wu, H., †Jayne, R.S. and Pollyea, R.M. 2018. A parametric analysis of capillary pressure effects during geologic carbon sequestration in a sandstone reservoir. *Greenhouse Gases: Science and Technology*, Vol. 8, No. 6, p. 1039-1052, December.

†Jayne, R.S., †Wu, H., and Pollyea, R.M. 2018. Geologic CO_2 sequestration in a basalt reservoir: Constraining permeability uncertainty within the Columbia River. *In Proceedings of the TOUGH Symposium 2018*, Ed. Oldenburg, C. Berkeley, California, October 8 - 10.
Note: Graduate student Richard S. Jayne won best student paper award for this contribution.

†Jayne, R.S. and Pollyea, R.M. 2018. Permeability correlation structure of the Columbia River Plateau and implications for fluid system architecture in continental large igneous provinces. *Geology*, Vol. 46, No. 8, p. 715–718. doi:10.1130/G45001.1.

†Gierzynski, A.O. and Pollyea, R.M. 2017. Three-phase CO_2 flow in a basalt fracture network. *Water Resources Research*, Vol. 53, No. 11, p. 8980–8998, November.

Pollyea, R.M. and Rimstidt, J.D. 2017. Rate equations for modeling carbon dioxide sequestration in basalt. *Applied Geochemistry*, Vol. 81, p. 53–62, June.

Pollyea, R.M. 2016. Influence of relative permeability on injection pressure and plume configuration during CO_2 injections in a mafic reservoir. *International Journal of Greenhouse Gas Control*, Vol. 46, p. 7–17, March.

6.2 Conference Abstracts (†Student Author)

†Jayne, R.S., Pollyea, R.M., and Zhang, Y. 2018. Non-isothermal effects of a CO_2 injection into a geologic reservoir, Abstract MR53A-2760, American Geophysical Union Fall Meeting, 10–14 December, Washington D.C.

†Wu, H., †Jayne, R.S., and Pollyea, R.M. 2018. Quantifying permeability alteration effects to CO_2 storage potential in a basalt fracture network, Abstract S51F-1615, American Geophysical Union Fall Meeting, 10–14 December, Washington D.C.

Gran, M., Zahasky, C., Garing, C., Pollyea, R.M., and Benson, S.M. 2017. Core- flooding experiments combined with X-rays and micro-PET imaging as a tool to calculate fluid saturations in a fracture, American Geophysical Union Fall Meeting, Abstract H21C-1466, 11–15 December, New Orleans, Louisiana.

†Jayne, R.S. and Pollyea, R.M. 2017. A spatial correlation model of permeability on the Columbia River Plateau, Abstract H34C-07, American Geophysical Union Fall Meeting, 11–15 December, New Orleans, Louisiana.

Gran, M., Zahasky, C., Garing, C., Pollyea, R.M., and Benson, S.M. 2017. Experimental study of relative permeability and saturation variations in a fractured basalt core. 9th International Conference on Porous Media & Annual Meeting (InterPore), 8–11 May, Rotterdam, Netherlands.

Pollyea, R.M. and Rimstidt, J.D. 2016. A kinetic rate model for crystalline basalt dissolution at temperature and pressure conditions relevant for geologic CO_2 sequestration, Abstract H51C-1486. American Geophysical Union Fall Meeting, 12–16 December, San Francisco, California.

†Gierzynski and Pollyea, R.M. 2016. Quantifying the effects of spatial uncertainty in fracture permeability on CO_2 leakage through Columbia River Basalt Flow interiors, Abstract GC41C-1102. American Geophysical Union Fall Meeting, 12–16 December, San Francisco, California.

†Jayne, R.S., and Pollyea, R.M. 2016. Constraining the effects of permeability uncertainty for geologic CO_2 sequestration in a basalt reservoir. Abstract GC41C-1110, American Geophysical Union Fall Meeting, 12–16 December, San Francisco, California

[†]Gierzynski and Pollyea, R.M. 2016. Quantifying the effects of spatial uncertainty in fracture permeability on CO_2 leakage through cap rocks during geologic CO_2 storage in continental flood basalts. Geological Society of America Annual Meeting, 25–28 September, Denver, Colorado.

Pollyea, R.M. 2015. System response as a function of relative permeability in geologic CO_2 sequestration, Abstract H52F-05. American Geophysical Union Fall Meeting, 14–18 December, San Francisco, California.

7. REFERENCES

Adeoye, J. T., Menefee, A. H., Xiong, W., Wells, R. K., Skemer, P., Giammar, D. E., & Ellis, B. R., 2017. Effect of transport limitations and fluid properties on reaction products in fractures of unaltered and serpentinized basalt exposed to high pCO_2 fluids. *International Journal of Greenhouse Gas Control*, 63, 310–320.

Aradóttir, E., Sonnenthal, E., Björnsson, G., Jónsson, H., 2012. Multidimensional reactive transport modeling of CO_2 mineral sequestration in basalts at the Hellisheidi geothermal field, Iceland. *International Journal of Greenhouse Gas Control* 9, 24–40.

Bachu, S., 2008. CO_2 storage in geological media: Role, means, status and barriers to deployment. *Progress in Energy and Combustion Science*, 34, 254–273.

Bachu, S., 2000. Sequestration of CO2 in geological media: criteria and approach for site selection in response to climate change. *Energy conversion and Management* 41 (9), 953–970.

Bachu, S., 2003. Screening and ranking of sedimentary basins for sequestration of CO2 in geological media in response to climate change. *Environmental Geology* 44 (3), 277–289.

Bacon, D. H., Ramanathan, R., Schaef, H. T., & McGrail, B. P., 2014. Simulating geologic co-sequestration of carbon dioxide and hydrogen sulfide in a basalt formation. *International Journal of Greenhouse Gas Control*, 21, 165–176. https://doi.org/10.1016/j.ijggc.2013.12.012

Barreyre, T., Olive, J.A., Crone, T.J., and Sohn, R.A., 2018, Depth-Dependent Permeability and Heat Output at Basalt-Hosted Hydrothermal Systems Across Mid-Ocean Ridge Spreading Rates: *Geochemistry Geophysics Geosystems*, v. 19, p. 1259–1281.

Benson, S. M., & Cole, D. R. 2008. CO2 sequestration in deep sedimentary formations. *Elements*, 4, 325–331.

Benson, S. M., et al., 2006. Monitoring carbon dioxide sequestration in deep geological formations for inventory verification and carbon credits. In: SPE Annual Technical Conference and Exhibition. Society of Petroleum Engineers.

Bertels, S. P., DiCarlo, D. A., & Blunt, M. J. 2001. Measurement of aperture distribution, capillary pressure, relative permeability, and in situ saturation in a rock fracture using computed tomography scanning. *Water Resources Research*, 37, 649–662.

Bianco, T.A., Ita, G., Becker, J.M., and Garcia, M.O., 2005, Secondary Hawaiian volcanism formed by flexural arch decompression: *Geochemistry Geophysics Geosystems*, v. 6, Q08009.

Bosshart, N. W., Azzolina, N. A., Ayash, S. C., Peck, W. D., Gorecki, C. D., Ge, J., Jiang, T., Dotzenrod, N. W., 2018. Quantifying the effects of depositional environment on deep saline formation CO_2 storage efficiency and rate. *International Journal of Greenhouse Gas Control* 69, 8–19.

Boulton, G.S., and Caban, P., 1995, Groundwater flow beneath ice sheets: part II – Its impact on glacier tectonic structures and moraine formation: *Quaternary Science Reviews*, v. 14, p. 563–587, https://doi.org/10.1016/0277-3791(95)00058-W.

Brennan, S. T., Burruss, R. C., 2003. Specific sequestration volumes: A useful tool for CO2 storage capacity assessment. US Department of the Interior, US Geological Survey.

Burns, E.R., Morgan, D.S., Peavler, R.S., and Kahle, S.C., 2011, Three-dimensional model of the geologic framework for the Columbia Plateau Regional Aquifer System, Idaho, Oregon, and Washington: U.S. Geological Survey Scientific Investigations Report 2010–5246, 44 p.

Burns, E.R., Williams, C.F., Ingebritsen, S.E., Voss, C.I., Spane, F.A., and DeAngelo, J., 2015, Understanding heat and groundwater flow through continental flood basalt provinces: Insights gained from alternative models of permeability/depth relationships for the Columbia Plateau, USA: *Geofluids*, v. 15, p. 120–138.

Camp, V. E. 1995. Mid-Miocene propagation of the Yellowstone mantle plume head beneath the Columbia River basalt source region. *Geology*, 23(5), 435–438.

Carneiro, J. F. 2009. Numerical simulations on the influence of matrix diffusion to carbon sequestration in double porosity fissured aquifers. *International Journal of Greenhouse Gas Control*, 3(4), 431–443.

Chadwick, A., Arts, R., Bernstone, C., May, F., Thibeau, S., Zweigel, P., 2008. Best Practice for the Storage of CO2 in Saline Aquifers-Observations and Guidelines from the SACS and CO2STORE projects. Vol. 14. British Geological Survey.

Clague, D.A., and Dalrymple, G.B., 1987, The Hawaiian-Emperor Volcanic Chain: U.S. Geological Survey Professional Paper, v. 1350, p. 5–54.

Clifford, S.M., and Parker, T.J., 2001, The evolution of the Martian hydrosphere: Implications for the fate of a primordial ocean and the current state of the northern plains: Icarus, v. 154, p. 40–79, https://doi.org/10.1006/icar.2001.6671.

Coffin, C.F., and Eldholm, O., 1994, Large igneous provinces: crustal structure, dimensions, and external consequences: Reviews of Geophysics, v. 32, p. 1–36, https://doi.org/10.1029/93RG02508.

Deutsch, C.V., and Journel, A.G., 1998, GSLIB: Geostatistical Software Library and User's Guide: New York, Oxford University Press, p. 369.

Doughty, C., 2010. Investigation of CO2 plume behavior for a large-scale pilot test of geologic carbon storage in a saline formation. *Transport in Porous Media* 82 (1), 49–76.

Doughty, C., Pruess, K., 2004. Modeling supercritical carbon dioxide injection in heterogeneous porous media. *Vadose Zone Journal* 3 (3), 837–847.

Doughty, C. 2000. Numerical model of water flow in a fractured basalt vadose zone: Box Canyon site, Idaho. *Water Resources Research*, 36, 3521–3534.

Fairley, J. 2016. Models and modeling: An introduction for earth and environmental scientists. Hoboken, NJ: John Wiley & Sons.

Fairley, J., Podgorney, R., & Wood, T. 2004. Unsaturated flow through a small fracture–matrix network. *Vadose Zone Journal*, 3(1), 101–108.

Freifeld, B. M., Daley, T. M., Hovorka, S. D., Henninges, J., Underschultz, J., Sharma, S., 2009. Recent advances in well-based monitoring of CO_2 sequestration. *Energy Procedia* 1 (1), 2277–2284.

Garven, G., 1995, Continental-scale groundwater flow and geologic processes: *Annual Review of Earth and Planetary Sciences*, v. 23, p. 89–117.

Ge, S. 1997. A governing equation for fluid flow in rough fractures. *Water Resources Research* 33, 53-61.

Gephart, R., Price, S., Jackson, R., and Myers, C., 1983, Geohydrologic Factors and Current Concepts Relevant to Characterization of a Potential Nuclear Waste Repository Site in Columbia River Basalt, Hanford Site, Washington: Materials Research Society Proceedings, v. 26, p. 85.

Gierzynski, A. O., Pollyea, R. M., 2017. Three-Phase CO_2 Flow in a Basalt Fracture Network. *Water Resources Research* 53 (11), 8980–8998.

Gislason, S. R., Wolff-Boenisch, D., Stefansson, A., Oelkers, E. H., Gunnlaugsson, E., Sigurdardottir, H., .Fridriksson, T. 2010. Mineral sequestration of carbon dioxide in basalt: A pre-injection overview of the CarbFix project. *International Journal of Greenhouse Gas Control*, 4(3), 537–545.

Glass, R. J., Nicholl, M. J., Rajaram, H., & Wood, T. R. 2003. Unsaturated flow through fracture networks: Evolution of liquid phase structure, dynamics, and the critical importance of fracture intersections. *Water Resources Research*, 39(12), 1352.

Gleeson, T., Smith, L., Moosdorf, N., Hartmann, J., Dürr, H.H., Manning, A.H., van Beek, L.P., and Jellinek, A.M., 2011, Mapping permeability over the surface of the Earth: *Geophysical Research Letters*, v. 38, L02401.

Goldberg, D. S., Kent, D. V., & Olsen, P. E. 2010. Potential on-shore and offshore reservoirs for CO2 sequestration in Central Atlantic magmatic province basalts. *Proceedings of the National Academy of Sciences* of the United States of America, 107, 1327–1332.

Goldberg, D. S., Takahashi, T., & Slagle, A. L. 2008. Carbon dioxide sequestration in deep-sea basalt. *Proceedings of the National Academy of Sciences* of the United States of America, 105, 9920–9925.

Gran, M., Zahasky, C., Garing, C., Pollyea, R., & Benson, S. 2017. Experimental study of relative permeability and saturation variations in a fractured basalt core. Paper presented at International Conference on Porous Media and Annual Meeting (InterPore), Rotterdam, The Netherlands.

Gysi, A. P., & Stefeansson, A. 2011. CO_2-water-basalt interaction. numerical simulation of low temperature CO_2 sequestration into basalts. *Geochimica et Cosmochimica Acta*, 75(17), 4728–4751.

Hales, T.C., Abt, D.L., Humphreys, E., and Roering, J.J., 2005, A lithospheric instability origin for Columbia River flood basalts and Wallowa Mountains uplift in northeast Oregon: *Nature*, v. 438, p. 842.

Hawkins, D. G., 2004. No exit: Thinking about leakage from geologic carbon storage sites. *Energy* 29 (9), 1571–1578.

Hegerl, G. C., Zwiers, F. W., Braconnot, P., Gillett, N. P., Luo, Y., Marengo Orsini, J., Nicholls, N., Penner, J. E., Stott, P. A., 2007. Understanding and attributing climate change. Tech. rep

Hieronymus, C.F., and Bercovici, D., 1999, Discrete alternating hotspot islands formed by interaction of magma transport and lithospheric flexure: *Nature*, v. 397, p. 604–607.

Hooper, P., Binger, G., & Lees, K. 2002. Ages of the Steens and Columbia River flood basalts and their relationship to extension-related calc-alkalic volcanism in eastern Oregon. *Geological Society of America Bulletin*, 114(1), 43–50.

Hooper, P.R., and Conrey, R., 1989, A model for the tectonic setting of the Columbia River basalt eruptions: *Geological Society of America. Special Paper*, v. 239, p. 293–306.

Huo, D., & Benson, S. M. 2015. An experimental investigation of stress-dependent permeability and permeability hysteresis behavior in rock fractures. Dynamics of Fluids and Transport in Complex Fractured-Porous Systems, 99-114.

Huo, D., Pini, R., & Benson, S. M. 2016. A calibration-free approach for measuring fracture aperture distributions using X-ray computed tomography. *Geosphere*, 12(2), 558-571.

Huo, D., & Benson, S.M. 2016. Experimental Investigation of Stress-Dependency of Relative Permeability in Rock Fractures, *Transport in Porous Media*, 113:567-590.

Ingebritsen, S.E., and Manning, C.E., 1999, Geological implications of a permeability-depth curve for the continental crust: *Geology*, v. 27, p. 1107–1110.

Jackson, E.D., and Wright, T.L., 1970, Xenoliths in the Honolulu Volcanic Series: Journal of Petrology, v. 11, p. 405–433.

Jayaraman, K. 2007. India's carbon dioxide trap. *Nature*, 445, 350.

Jayne, R.S. and Pollyea, R.M., 2018. Permeability correlation structure of the Columbia River Plateau and implications for fluid system architecture in continental large igneous provinces. *Geology*, *46*(8), pp.715-718.

Jayne, R. S., & Pollyea, R. M. 2016. Constraining the effects of permeability uncertainty for geologic CO2 sequestration in a basalt reservoir. Abstract CG41C-1110 presented at 2016 Annual Meeting of the American Geophysical Union, San Francisco, CA.

Jiang, X.W., Wan, L., Wang, X.S., Ge, S., and Liu, J., 2009, Effect of exponential decay in hydraulic conductivity with depth on regional groundwater flow: Geophysical Research Letters, v. 36, p. L24402, https://doi.org/10.1029/2009GL041251.

Johnston, P., Wu, P., and Lambeck, K., 1998, Dependence of horizontal stress magnitude on load dimension in glacial rebound models: Geophysical Journal International, v. 132, p. 41–60, https://doi.org/10.1046/j.1365-246x.1998.00387.x.

Jung, Y., Pau, G. S. H., Finsterle, S., & Pollyea, R. M. 2017. TOUGH3: A new efficient version of the TOUGH suite of multiphase flow and transport simulators. *Computers & Geosciences*, 108, 2–7.

Kahle, S., Morgan, D., Welch, W., Ely, D., Hinkle, S., Vaccaro, J., Orzol, L., 2011. Hydrogeologic framework and hydrologic budget components of the Columbia Plateau Regional Aquifer System, Washington, Oregon, and Idaho. Tech. rep., US Geological Survey.

Kerrick, D.M., and Caldeira, K., 1998, Metamorphic CO_2 degassing from orogenic belts: Chemical Geology, v. 145, p. 213–232.

Kwicklis, E. M., & Healy, R. W. 1993. Numerical investigation of steady liquid water flow in a variably saturated fracture network. *Water Resources Research*, 29, 4091–4102.

Lackner, K. S., 2003. A guide to CO_2 sequestration. *Science* 300 (5626), 1677–1678.

Lamur, A., Kendrick, J., Eggertsson, G., Wall, R., Ashworth, J., & Lavallee, Y. 2017. The permeability of fractured rocks in pressurised volcanic and geothermal systems. *Scientific Reports*, 7, 6173.

LaViolette, R. A., Glass, R., Wood, T. R., McJunkin, T., Noah, R. K., Podgorney, R. K.,…Stoner, D. L. 2003. Convergent flow observed in a laboratory-scale unsaturated fracture system. *Geophysical Research Letters*, 30(2), 1083.

Law, J., et al., 1944. A statistical approach to the interstitial heterogeneity of sand reservoirs. Transactions of the AIME 155 (01), 202–222.

Li, B., Benson, S. M., 2015. Influence of small-scale heterogeneity on upward CO2 plume migration in storage aquifers. *Advances in Water Resources* 83, 389–404.

Li, Y., LeBoeuf, E. J., Basu, P. K., Mahadevan, S., 2005. Stochastic modeling of the permeability of randomly generated porous media. *Advances in Water Resources* 28 (8), 835–844.

Lindberg, J. W. 1989. A numerical study of cooling joint width and secondary mineral infilling in four Grande ronde basalt flows of the central Columbia plateau, Washington. *Geological Society of America Special Papers*, 239, 169–186.

Litynski, J. T., Klara, S. M., McIlvried, H. G., Srivastava, R. D., 2006. The United States Department of Energy's regional carbon sequestration partnerships program: a collaborative approach to carbon management. *Environment International* 32 (1), 128–144.

Long, P.E., and Wood, B.J., 1986, Structures, textures, and cooling histories of Columbia River basalt flows: *Geological Society of America Bulletin*, v. 97, p. 1144–1155.

Luhmann, A. J., Tutolo, B. M., Bagley, B. C., Mildner, D. F., Seyfried, W. E., & Saar, M. O. 2017a. Permeability, porosity, and mineral surface area changes in basalt cores induced by reactive transport of CO2-rich brine. *Water Resources Research*, 53, 1908–1927.

Luhmann, A. J., Tutolo, B. M., Tan, C., Moskowitz, B. M., Saar, M. O., & Seyfried, W. E. 2017b. Whole rock basalt alteration from CO2-rich brine during flow-through experiments at 150 C and 150 bar. *Chemical Geology*, 453, 92–110.

Mangan, M. T., Wright, T. L., Swanson, D. A., & Byerly, G. R. 1986. Regional correlation of Grande ronde basalt flows, Columbia river basalt group, Washington, Oregon, and Idaho. *Geological Society of America Bulletin*, 97(11), 1300–1318.

Manning, C., and Ingebritsen, S., 1999, Permeability of the continental crust: Implications of geothermal data and metamorphic systems: *Reviews of Geophysics*, v. 37, p. 127–150.

Mathieson, A., Midgley, J., Dodds, K., Wright, I., Ringrose, P., Saoul, N., 2010. CO_2 sequestration monitoring and verification technologies applied at Krechba, Algeria. *The Leading Edge* 29 (2), 216–222.

Matter, J. M., & Kelemen, P. B. 2009. Permanent storage of carbon dioxide in geological reservoirs by mineral carbonation. Nature Geoscience, 2, 837–841.

Matter, J.M., Stute, M., Snæbjornsdottir, S.O., Oelkers, E.H., Gislason, S.R., Aradottir, E.S., ...Broecker,W.S. 2016. Rapid carbon mineralization for permanent disposal of anthropogenic carbon dioxide emissions. *Science*, 352(6291), 1312–1314.

Matter, J. M., Takahashi, T., Goldberg, D., 2007. Experimental evaluation of in situ CO2-water-rock reactions during CO2 injection in basaltic rocks: Implications for geological CO2 sequestration. *Geochemistry, Geophysics, Geosystems* 8 (2).

McGrail, B.P., Schaef, H.T., Spane, F.A., Cliff, J.B., Qafoku, O., Horner, J.A., Thompson, C.J., Owen, A.T., and Sullivan, C.E., 2017, Field validation of supercritical CO_2 reactivity with basalts: *Environmental Science & Technology Letters*, v. 4, p. 6–10.

McGrail, B., Sullivan, E., Spane, F., Bacon, D., Hund, G., Thorne, P., . . . Colwell, F. 2009. Topical report—Preliminary hydrogeologic characterization results from the Wallula basalt pilot study (Tech. Rep. PNWD-4129). Richland, WA: Pacific Northwest National Laboratory.

McGrail, B. P., Schaef, H. T., Ho, A. M., Chien, Y.-J., & Dooley, J. J. 2006. Potential for carbon dioxide sequestration in flood basalts. *Journal of Geophysical Research*, 111, B12201.

McGrail, B. P., Schaef, H. T., Spane, F. A., Cliff, J. B., Qafoku, O., Horner, J. A., . . . Sullivan, C. E. 2017. Field validation of supercritical CO2 reactivity with basalts. *Environmental Science & Technology Letters*, 4, 6–10.

McGrail, B. P., Spane, F. A., Amonette, J. E., Thompson, C., & Brown, C. F. 2014. Injection and monitoring at the Wallula basalt pilot project. *Energy Procedia*, 63, 2939–2948.

Metz, B., Davidson, O., De Coninck, H., Loos, M., Meyer, L., 2005. IPCC special report on carbon dioxide capture and storage. Tech. rep., Intergovernmental Panel on Climate Change, Geneva (Switzerland). Working Group III.

Moore, J.G., 1970, Relationship between subsidence and volcanic load, Hawaii: *Bulletin of Volcanology*, v. 24, p. 563–576.

Nara, Y., Meredith, P. G., Yoneda, T., & Kaneko, K. 2011. Influence of macro-fractures and micro-fractures on permeability and elastic wave velocities in basalt at elevated pressure. *Tectonophysics*, 503(1), 52–59.

Navarre-Sitchler, A. K., Maxwell, R. M., Siirila, E. R., Hammond, G. E., Lichtner, P. C., 2013. Elucidating geochemical response of shallow heterogeneous aquifers to CO_2 leakage using high-performance computing: Implications for monitoring of CO2 sequestration. *Advances in Water Resources* 53, 45–55.

NETL, 2011. Best Practices for: Risk Analysis and Simulation of Geologic Storage of CO2. Neufeld, J. A., Vella, D., Huppert, H. E., 2009. The effect of a fissure on storage in a porous medium. *Journal of Fluid Mechanics* 639, 239–259.

Neuman, S.P., 1990, Universal scaling of hydraulic conductivities and dispersivities in geologic media: *Water Resources Research*, v. 26, p. 1749–1758.

Oldenburg, C., Lewicki, J., 2006. On leakage and seepage of CO2 from geologic storage sites into surface water. *Environmental Geology* 50 (5), 691–705.

Oldenburg, C. M., 2007. Joule-Thomson cooling due to CO2 injection into natural gas reservoirs. *Energy Conversion and* Management 48 (6), 1808–1815.

Orr, F. M., 2009. Onshore geologic storage of CO2. *Science* 325 (5948), 1656–1658.

Pacala, S., & Socolow, R. 2004. Stabilization wedges: Solving the climate problem for the next 50 years with current technologies. *Science*, 305, 968–972.

Parker, J., Lenhard, R., & Kuppusamy, T. 1987. A parametric model for constitutive properties governing multiphase flow in porous media. *Water Resources Research*, 23, 618–624.

Pawar, R. J., Watson, T. L., Gable, C. W., 2009. Numerical simulation of CO2 leakage through abandoned wells: Model for an abandoned site with observed gas migration in Alberta, Canada. *Energy Procedia* 1 (1), 3625–3632.

Pini, R., & Benson, S. M. 2013. Simultaneous determination of capillary pressure and relative permeability curves from core-flooding experiments with various fluid pairs. *Water Resources Research*, 49, 3516–3530.

Pollack, H. N., Hurter, S. J., Johnson, J. R., 1993. Heat flow from the Earth's interior: analysis of the global data set. *Reviews of Geophysics* 31 (3), 267–280.

Pollyea, R. 2016. Influence of relative permeability on injection pressure and plume configuration during CO2 injections in a mafic reservoir. *International Journal of Greenhouse Gas Control*, 46, 7–17.

Pollyea, R.M., Van Dusen, E.W., and Fischer, M.P., 2015, Topographically driven fluid flow within orogenic wedges: Effects of taper angle and depth-dependent permeability: *Geosphere*, v. 11, p. 1427–1437.

Pollyea, R. M., & Fairley, J. P. 2011. Estimating surface roughness of terrestrial laser scan data using orthogonal distance regression. *Geology*, 39(7), 623–626.

Pollyea, R. M., & Fairley, J. P. 2012a. Implications of spatial reservoir uncertainty for CO2 sequestration in the east Snake River Plain, Idaho (USA). *Hydrogeology Journal*, 20, 689–699. https://doi.org/10.1007/s10040-012-0847-1

Pollyea, R. M., & Fairley, J. P. 2012b. Experimental evaluation of terrestrial lidar-based surface roughness estimates. *Geosphere*, 8(1), 1–7.

Pollyea, R. M., Fairley, J. P., Podgorney, R. K., & McLing, T. L. 2014. Physical constraints on geologic CO2 sequestration in low-volume basalt formations. *Geological Society of America Bulletin*, 126(3/4), 344–351.

Pollyea, R. M., & Rimstidt, J. D. 2017. Rate equations for modeling carbon dioxide sequestration in basalt. *Applied Geochemistry*, 81, 53–62.

Popova, O. H., Small, M. J., McCoy, S. T., Thomas, A., Rose, S., Karimi, B., Carter, K., Goodman, A., 2014. Spatial stochastic modeling of sedimentary formations to assess CO2 storage potential. *Environmental Science & Technology* 48 (11), 6247–6255.

Price, P. N., Oldenburg, C. M., 2009. The consequences of failure should be considered in siting geologic carbon sequestration projects. *International Journal of Greenhouse Gas Control* 3 (5), 658–663.

Pruess, K., 1992. Brief guide to the MINC-method for modeling flow and transport in fractured media. Earth science division. Lawrence Berkeley Laboratory, University of California, Berkeley 10179.

Pruess, K., Garcia, J., 2002. Multiphase flow dynamics during CO2 disposal into saline aquifers. *Environmental Geology* 42 (2-3), 282–295.

Pruess, K., Xu, T., Apps, J., Garcia, J., 2003. Numerical Modeling of Aquifer Disposal of CO2. SPEJ 8 (1): 49–60. Tech. rep., SPE-83695-PA. DOI: 10.2118/83695-PA.

Pruess, K. 2005. Numerical simulations show potential for strong nonisothermal effects during fluid leakage from a geologic disposal reservoir for CO_2. In Dynamics of fluids and transport in fractured rock (pp. 81–89). Washington, DC: American Geophysical Union.

Pruess, K. 2011. ECO2M: A TOUGH2 fluid property module for mixtures of water, NaCl, and CO2, including super-and sub-critical conditions, and phase change between liquid and gaseous CO2 (Tech. Rep. LBNL-4590E). Berkeley, CA: Lawrence Berkeley National Laboratory.

Ramos, F. C., Wolff, J. A., & Tollstrup, D. L. 2005. Sr isotope disequilibrium in Columbia River flood basalts: Evidence for rapid shallow-level open-system processes. Geology, 33(6), 457–460. https://doi.org/10.1130/G21512.1

Reidel, S. 2015. The Columbia River Basalt Group: A flood basalt province in the Pacific Northwest, USA. Geoscience Canada, 42, 151–168.

Reidel, S. P., 1998. Emplacement of Columbia River flood basalt. *Journal of Geophysical Research* 103 (B11), 27–393.

Reidel, S. P., Camp, V. E., Tolan, T. L., & Martin, B. S. 2013. The Columbia River flood basalt province: Stratigraphy, areal extent, volume, and physical volcanology. Geological Society of America Special Paper, 497, 1–43.

Reidel, S.P., Fecht, K.R., Hagood, M.C., and Tolan, T.L., 1989, The geologic evolution of the central Columbia Plateau: Geological Society of America. Special Paper, v. 239, p. 247–264, https://doi.org/10.1130/SPE239-p247.

Reidel, S.P., Spane, F.A., and Johnson, V.G., 2002, Natural gas storage in basalt aquifers of the Columbia basin, Pacific Northwest USA: A guide to site characterization: Pacific Northwest Laboratory Report PNNL-13962, 277 p.

Rochelle, C., Czernichowski-Lauriol, I., Milodowski, A., 2004. The impact of chemical reactions on CO2 storage in geological formations: a brief review. Geological Society, London, Special Publications 233 (1), 87–106.

Rodosta, T., Litynski, J., Plasynski, S., Spangler, L., Finley, R., Steadman, E., Ball, D., Hill, G., McPherson, B., Burton, E., et al., 2011. US Department of Energy regional carbon sequestration partnership initiative: Update on validation and development phases. *Energy Procedia* 4, 3457–3464.

Roebuck, J., Murrell, T., Miller, E., 1942. The Joule-Thomson effect in carbon dioxide. *Journal of the American Chemical Society* 64 (2), 400–411.

Rubin, Y. (2003). Applied stochastic hydrogeology. New York, NY: Oxford University Press.

Saar, M., and Manga, M., 2004, Depth dependence of permeability in the Oregon Cascades inferred from hydrogeologic, thermal, seismic, and magmatic modeling constraints: Journal of Geophysical Research. Solid Earth, v. 109, p. B04204.

Saar, M.O., 2011, Geothermal heat as a tracer of large-scale groundwater flow and as a means to determine permeability fields: Hydrogeology Journal, v. 19, p. 31–52.

Schaef, H., McGrail, B., & Owen, A. 2011. Basalt reactivity variability with reservoir depth in supercritical CO2 and aqueous phases. *Energy Procedia*, 4, 4977–4984.

Schaef, H., McGrail, B., Owen, A., & Arey, B. 2013. Mineralization of basalts in the CO2-H2O-H2S system. *International Journal of Greenhouse Gas Control*, 16, 187–196.

Sigfusson, B., Gislason, S. R., Matter, J. M., Stute, M., Gunnlaugsson, E., Gunnarsson, I., . . . Oelkers, E. H. 2015. Solving the carbon-dioxide buoyancy challenge: The design and field testing of a dissolved CO2 injection system. *International Journal of Greenhouse Gas Control*, 37, 213–219.

SIO. 2017. The keeling curve, full record. San Diego, Ca: Author. Retrieved from https://scripps.ucsd.edu/programs/keelingcurve/

Srivastava, R. M., 1994a. An overview of stochastic methods for reservoir characterization. *AAPG Computational Applied Geology* (3), 3–16.

Stone, H. 1970. Probability model for estimating three-phase relative permeability. Journal of Petroleum Technology, 22(02), 214–218.

Tolan, T. L., Reidel, S. P., Beeson, M. H., Anderson, J. L., Fecht, K. R., & Swanson, D. A. 1989. Revisions to the estimates of the areal extent and volume of the Columbia River Basalt Group. *Geological Society of America Special Papers*, 239, 1–20.

Townend, J., and Zoback, M.D., 2000, How faulting keeps the crust strong: *Geology*, v. 28, p. 399–402.

USDOE, 2013. Carbon Technology Program Plan. Tech. rep.

Van der Meer, L., 1995. The CO_2 storage efficiency of aquifers. *Energy Conversion and Management* 36 (6-9), 513–518.

Van Genuchten, M. (1980). A closed-form equation for predicting the hydraulic conductivity of unsaturated soils, Soil. Science Society of America, 44, 892–898.

Vye-Brown, C., Self, S., & Barry, T. 2013. Architecture and emplacement of flood basalt flow fields: Case studies from the Columbia River Basalt Group, NW USA. *Bulletin of Volcanology*, 75(3), 697.

Walcott, R., 1970a, Isostatic response to loading of the crust in Canada: *Canadian Journal of Earth Sciences*, v. 7, p. 716–727.

Walcott, R., 1970b, Flexural rigidity, thickness, and viscosity of the lithosphere: *Journal of Geophysical Research*, v. 75, p. 3941–3954.

Walker, R. J., Holdsworth, R. E., Armitage, P. J., & Faulkner, D. R. 2013a. Fault zone permeability structure evolution in basalts. Geology, 41(1), 59–62.

Walker, R. J., Holdsworth, R., Imber, J., Faulkner, D., & Armitage, P. 2013b. Fault zone architecture and fluid flow in interlayered basaltic volcaniclastic-crystalline sequences. *Journal of Structural Geology*, 51, 92–104.

Weis, P., 2015, The dynamic interplay between saline fluid flow and rock permeability in magmatic-hydrothermal systems: *Geofluids*, v. 15, p. 350–371.

Wigley, T. M., Richels, R., Edmonds, J. A., 1996. Economic and environmental choices in the stabilization of atmospheric CO_2 concentrations. *Nature* 379 (6562), 240–243.

Witherspoon, P., Wang, J., Iwai, K., & Gale, J. 1980. Validity of cubic law for fluid flow in a deformable rock fracture. Water Resources Research, 16, 1016–1024.

Wood, T., Glass, R., McJunkin, T., Podgorney, R., Laviolette, R., Noah, K., . . . Baker, K. 2004. Unsaturated flow through a small fracture–matrix network. *Vadose Zone Journal*, 3(1), 90–100.

Wood, W. W., & Fernandez, L. 1988. Volcanic rocks. In W. Back, J. Rosenshein, & P. Seaber (Eds.), The geology of North America, Vol. O-2. Hydrogeology (chap. 39, pp. 353–365). Boulder, CO: Geological Society of America.

Zakharova, N. V., Goldberg, D. S., Sullivan, E. C., Herron, M. M., & Grau, J. A.2012. Petrophysical and geochemical properties of Columbia River flood basalt: Implications for carbon sequestration. *Geochemistry, Geophysics, Geosystems*, 13, Q11001.

Zhou, Q., Salve, R., Liu, H.-H., Wang, J. S., & Hudson, D. 2006. Analysis of a mesoscale infiltration and water seepage test in unsaturated fractured rock: Spatial variabilities and discrete fracture patterns. *Journal of Contaminant Hydrology*, 87(1), 96–122.